

**Investigating Front Variations of  
Greenland Glaciers Using  
Multi-temporal Remote Sensing Images  
and Deep Learning**

**ZHANG, Enze**

A Thesis Submitted in Partial Fulfilment  
of the Requirements for the Degree of  
Doctor of Philosophy  
in  
Earth and Atmospheric Sciences

The Chinese University of Hong Kong  
September 2020

## **Thesis Assessment Committee**

Professor CHAN Man Nin (Chair)

Professor LIU Lin (Thesis Supervisor)

Professor YANG Hongfeng (Committee Member)

Professor CATANIA Ginny (External Examiner)

# Abstract

of thesis entitled:

Investigating Front Variations of Greenland Glaciers Using Multi-temporal  
Remote Sensing Images and Deep Learning

Submitted by ZHANG, Enze

for the degree of Doctor of Philosophy

at The Chinese University of Hong Kong in September 2020

Quantification of front variations of glaciers in Greenland is essential for understanding ice-ocean interaction, glacier dynamics, and a more accurate projection of global sea-level rise. Most previous studies manually delineated ice fronts from remote sensing images. Such manual efforts, however, are becoming more labor-intensive and even impractical for quantifying temporal changes of ice fronts at a large number of glaciers in a detailed manner, because the volume and diversity of satellite images have been increasing significantly.

Automating the identification of glaciological features such as calving fronts therefore becomes necessary. In the first study, we applied U-Net, a deep learning architecture, to multi-temporal Synthetic Aperture Radar images taken by the TerraSAR-X satellite and automated the delineation of the calving front positions of Jakobshavn Isbræ from 2009 to 2015. The results are consistent with the manually delineated products generated by the Greenland Ice Sheet Climate Change

Initiative project with the mean test errors of 38 meters ( 6 pixels). We show that the calving fronts of Jakobshavn’s two main branches retreated at mean rates of  $-117 \pm 1 \text{ m yr}^{-1}$  and  $-157 \pm 1 \text{ m yr}^{-1}$ , respectively, during the years 2009 to 2015. We suggest that the retreat of the calving front into an overdeepened basin whose bed is retrograde may have accelerated the retreat after 2011, while the inland-uphill bed slope behind the bottom of the overdeepened basin has prevented the glacier from retreating further after 2012. Although we demonstrate the feasibility of deep-learning-based method, this study is limited to a specific study area (e.g., Jakobshavn Isbræ) and dataset (e.g., TerraSAR-X).

The second study further improves the generalization and robustness of the deep-learning-based method to release its constraint of applicable region and data. The method can be applied an outlet glacier or remote sensing datasets that are not included in training, and we integrate seven remote sensing datasets into a single deep learning network. The core datasets include optical (Landsat-8 and Sentinel-2) and synthetic aperture radar images (Envisat, ALOS-1, TerraSAR-X, Sentinel-1, and ALOS-2) taken over Jakobshavn Isbræ, Kangerlussuaq, and Helheim, spanning from 2002 to 2019. We evaluate four neural network architectures (e.g., U-Net, DeepLabv3+ with Resnet, DRN, and Mobilenet as the backbones) and three pre-processing procedures (e.g. histogram normalization, linear stretching, and no histogram manipulation). We find that the combination of histogram normalization and DRN-DeepLabv3+ has the lowest mean test error, 86 meters. We produce a sub-weekly calving front dataset for the three glaciers by integrating seven datasets. Owing to the high temporal resolution, our results reveal large calving events as well as synchronous and asynchronous front variations between neighboring branches or glaciers.

In summary, by applying deep-learning-based method to multi-temporal and multi-sensor remote sensing imagery, I successfully automate the delineation of

front positions of Jakobshavn Isbræ, Kangerdlugssuaq, and Helheim. Due to the transferable nature of deep learning, the methodology can be applied to many other tidewater glaciers both in Greenland and elsewhere in the world. Our method has the potential to produce a spatially, temporally comprehensive calving front dataset, which will help to improve the understanding of front dynamics and glacial mass balance.

# 摘要

## 基於深度學習以及多時相遙感影像的格陵蘭島冰川前緣變化研究

冰川前緣變化的定量研究對於理解海冰交互作用，冰川動力學，以及更精準地預測全球海平面上升有著重要作用。先前的研究大多數基於從遙感影像中人工提取邊界。然而，此種方法耗時耗力，而且由於衛星影像的數量以及多樣性的急劇增加，人工提取無法實現對於大量冰川的細緻定量分析。

自動化諸如冰川前緣的冰川學特徵提取就變的極為重要。在第一個研究中，我們將名為 U-Net 的深度學習神經網絡應用於多時項 TerraSAR-X 合成孔徑雷達影像上，並從中自動提取了 Jakobshavn Isbræ 冰川自 2009 至 2015 年間的前緣邊界。我們的結果和 Greenland Ice Sheet Climate Change Initiative 項目人工提取的產品基本一致，並且結果的測試誤差在 38 米（約 6 個像素點）。結果顯示從 2009 到 2015，Jakobshavn Isbræ 冰川的兩個分支的平均回退速度分別為 $-117 \pm 1$  米每年以及 $-157 \pm 1$  米每年。我們認為在 2011 之後年冰川會退到一個冰床向內陸凹陷的盆地，並導致了其回退的加速。在 2012 年之後冰川邊界處的冰床向內陸上升，阻止了冰川繼續會退。儘管我們的研究證實了深度學習方法的可行性，該方法只適用於特定區域（如 Jakobshavn Isbræ）以及特定數據集（如 TerraSAR-X）。

第二項研究進一步增加了深度學習方法的普適性以及穩健性並解除了其對於特定區域和數據集的限制。該方法可以應用於訓練數據所不含蓋的冰川以及數據集。我們的核心數據包括從 2002 到 2019，覆蓋 Jakobshavn Isbræ，Kanger-

lussuaq 和 Helheim 的光學 (Landsat-8 和 Sentinel-2) 以及合成孔徑雷達 (Envisat, ALOS-1, TerraSAR-X, Sentinel-1 和 ALOS-2) 影像。我們評估了四個深度學習網絡 (如 U-Net, 以 Resnet, DRN, Mobilenet 為核心的 DeepLabv3+) 以及三個預處理方法 (直方圖正態化, 線性拉伸和無處理)。我們發現 DRN-DeepLabV3+ 和直方圖正態化的組合有最好的準確度，其測試誤差為 86 米。通過整合七個數據集，冰川前緣數據的採樣頻率超過了每週兩次。得益於數據的高時間分辨率，我們的時間序列可以直接顯示大的冰裂事件，並且可以直觀顯示出臨近冰川或分支前緣的同異步變化。

總的來說，我們通過將深度學習算法應用於多時項，多感應器遙感影像，成功地自動提取了 Jakobshavn Isbræ, Kangerdlugssuaq, 和 Helheim 冰川的前緣。由於深度學習自身的可移植性，我們的方法還能應用於格陵蘭島乃至世界其他地區的冰川。我們的方法有潛力提供一個在時間、空間尺度的全面性達到前所未有的高度的冰川前緣數據集。該數據將會對理解冰川前緣動態學以及冰川質量平衡提供有力幫助。

# Acknowledgement

Throughout my Ph.D. study and completing this dissertation, I have received a lot of support and guidance. I would like to take this opportunity to express my deep and sincere gratitude to all the people who have helped me in the past four years. This thesis would not be possible without the support from all of you.

Firstly, I would like to express my sincere gratitude to my advisor Prof. LIU Lin for the continuous support of my Ph.D. study. Your patience, motivation, and immense knowledge mean a lot for me. I joined Lin's group as a visiting student in 2015 summer when I was an undergraduate. Two months working with Lin inspired my interest in studying glaciers in Greenland. Then I started pursuing my Ph.D. in Earth science. I appreciate all your contributions of time, ideas, and funding to make my Ph.D. experience productive.

I want to thank the committee members of my dissertation: Prof. Ginny Catania, Prof. CHAN Man Nin, and Prof. YANG Hongfeng for generously offering your time to review this document and serving as examiners in my oral defense. Your support, constructive as well as insightful comments, and invaluable suggestions make this dissertation better.

I would like to thank Prof. Anders Anker Bjørk and Prof. Shfaqat Abbas Khan for hosting my visit to the University of Copenhagen for six months. It was a delightful and fulfilling period working with you. I gained much insight and knowledge in our collaboration on finding newly revealed islands in Greenland,

which will benefit my future research.

I would like to thank my former and current group mates: Bao Zhang, Yufeng Hu, Zhiwei Zhou, Bo Hu, Joseph Ma Ho Yin, Jiangjun Ran, Kenneth Ho Ngai Lun, Xiaowen Wang, Lingcao Huang, Yan Hu, Jie Chen, Xiyu Chen, Xingyu Xu, and Jiahua Zhang for the support and help. Also, I would like to thanks all the EASC members for the friendships with them. My life has been much more colorful because of you.

Last, I would like to express my most profound appreciation to my parents for being supportive all the time.

# Contents

<b>Abstract</b>	i
<b>摘要</b>	iv
<b>Acknowledgement</b>	vi
<b>Contents</b>	viii
<b>List of Figures</b>	xii
<b>List of Tables</b>	xviii
<b>1 Introduction</b>	1
1.1 Background . . . . .	1
1.1.1 Glacier front variations in Greenland . . . . .	1
1.1.1.1 Observations . . . . .	1
1.1.1.2 Potential mechanisms and remaining questions .	2
1.1.1.3 Development of remote sensing dataset . . . . .	4
1.1.2 Previous mapping efforts . . . . .	7
1.1.2.1 Manual delineation . . . . .	7
1.1.2.2 Feature extracting methods . . . . .	8
1.1.2.3 Deep-learning-based methods . . . . .	8
1.2 Deep Learning . . . . .	9
	viii

1.2.1	Basic concepts of deep learning . . . . .	9
1.2.2	Convolutional neural network . . . . .	11
1.2.3	Applications of deep learning to remote sensing . . . . .	13
1.3	Objectives and hypotheses . . . . .	13
1.4	Road map of dissertation . . . . .	14
1.5	Innovative merits and potential impacts . . . . .	15
<b>2</b>	<b>The first trial of applying deep learning</b>	<b>17</b>
2.1	Introduction . . . . .	18
2.2	Jakobshavn Isbræ . . . . .	19
2.3	TerraSAR-X images and pre-processing . . . . .	21
2.4	Deep Learning and post-processing . . . . .	23
2.5	Data validation and error estimation . . . . .	28
2.6	Results . . . . .	29
2.7	Discussion . . . . .	32
2.7.1	Differences from the previous work . . . . .	32
2.7.2	Calving front variation and bed elevation . . . . .	35
2.7.3	Limitations of current method . . . . .	38
2.7.4	Prospects for future work . . . . .	38
2.8	Conclusion . . . . .	39
<b>3</b>	<b>A generalized method based on deep learning</b>	<b>40</b>
3.1	Introduction . . . . .	41
3.1.1	Study areas . . . . .	41
3.1.1.1	Jakobshavn Isbræ . . . . .	42
3.1.1.2	Kangerlussuaq and Helheim . . . . .	42
3.1.2	Remote sensing dataset . . . . .	44
3.2	Method . . . . .	47

3.2.1	An alternative CNN: DeepLabv3+ . . . . .	47
3.2.2	Improvements of deep-learning-based framework . . . . .	50
3.2.2.1	Pre-processing procedures . . . . .	51
3.2.2.2	Network training . . . . .	53
3.2.2.3	Post-processing procedures . . . . .	55
3.3	Results . . . . .	57
3.4	Discussion . . . . .	64
3.4.1	Advantages and limitations . . . . .	64
3.4.2	Synchronous and asynchronous dynamic behaviors of glaciers	65
3.4.3	Misidentification caused by artifacts and tabular icebergs .	66
3.4.4	Prospects for improvement . . . . .	68
3.5	Conclusion . . . . .	70
<b>4</b>	<b>Conclusion</b>	<b>71</b>
4.1	Summary . . . . .	71
4.2	Future Work . . . . .	72
4.2.1	A broader application to all major outlet glaciers in Greenland	73
4.2.2	Quantifying the spatio-temporal characteristics of calving front variations . . . . .	74
4.2.3	Using structural equation modeling to analyze causal relationships . . . . .	74
<b>A</b>	<b>Supplementary figures, movies and tables for Chapter 2</b>	<b>77</b>
<b>B</b>	<b>Glossary of abbreviations</b>	<b>82</b>
	<b>List of publications and outputs</b>	<b>84</b>
	<b>Bibliography</b>	<b>86</b>

# List of Figures

1.1	A map showing retreat rates of the three largest glaciers in Greenland from 2000 to 2010. The data is derived from [Murray et al., 2015]. . . . .	3
1.2	Diagram summarizing potential mechanisms that control front variations. One-headed arrows indicate a directed relationship, and two-headed arrows indicate an undirected relationship. . . . .	4
1.3	Remote sensing datasets introduced in this dissertation. Optical and SAR images are groups within outer and inner arcs, respectively. Numbers in the parentheses are nominal revisit times in days. Landsat 7 images obtained after 2003 may still be useful, despite suffering from defects due to the failure of its Scan Line Corrector (SLC). Landsat 9 is scheduled to launch in 2021. . . . .	6



2.3	The Architecture of the U-Net. The red box indicates the contracting path and the blue box indicates the expansive path. Each solid blue box corresponds to a multi-channel feature map. Gray solid boxes represent copied feature maps. The length, width, and height of each layer correspond to the pixel dimensions and the number of feature channels respectively. Arrows with different colors denote the different operations. This figure is adopted from [Ronneberger et al., 2015]	24
2.4	Diagram of the proposed framework. Details are described in Sections 2.3 and 2.4.	25
2.5	Examples of (a) superior and (b) inferior delineation from our deep-learning-based method. In both (a) and (b), the red line shows the calving front delineated by the network. (c) and (d) show the zoom-in figure of the obscure calving front positions within the blue boxes in (b).	30
2.6	Time series of calving front variations (in area changes) of Branches A and B from our deep learning method (stars) and the Greenland Ice Sheet CCI project (triangles). Dashed vertical lines divide the time series into three separate phases (see text).	31
2.7	Two examples showing the asynchronous behaviors of Branches A and B. (a) Branch A began to retreat in May 2010, while Branch B started to retreat one month later. (b) Branch A’s calving front underwent strong variation between August to November 2012, whereas Branch B’s calving front was relatively stable. The magenta line in both (a) and (b) shows the calving front position just before the annual retreat.	33

2.8	Two examples showing the asynchronous behaviors of Branches A and B. (a) Branch A began to retreat in May 2010, while Branch B started to retreat one month later. (b) Branch A’s calving front underwent strong variation between August to November 2012, whereas Branch B’s calving front was relatively stable. The magenta line in both (a) and (b) shows the calving front position just before the annual retreat. . . . .	34
2.9	Bed elevation profiles of two branches derived from BedMachine v3 [Morlighem et al., 2017]. The profile locations are shown in Figure 2.1a. The dashed box shows the zone where the bed slopes uphill inland. . . . .	37
3.1	Location of the glaciers included in this research. Red lines show the network-delineated calving fronts. . . . .	44
3.2	Illustration of a simple atrous convolution with the kernel size of 2, and the rate of atrous convolution is 2. Equation below shows the calculation of atrous convolution for the upper-left unit of the output layer. . . . .	48
3.3	Architecture of DeepLabv3+ (adapted from [Chen et al., 2018]). The network is constructed by an encoder (blue) and a decoder (red). The encoder is composed of the network backbone, the ASPP module (black), and the following $1 \times 1$ convolution. The decoder combines the low-level feature from the network backbone and the encoder output. . . . .	50
3.4	Diagram of the deep-learning-based framework (modified from figure 2.4). . . . .	51

3.5	The comparison between original (a & c) and normalized images (b & d). We normalize each image histogram to the same Gaussian distribution with identical pixel value ranges (b & d). The second column shows the histograms of corresponding images. . . . .	52
3.6	Illustration of our data splitting strategy. Red indicates the training-validation set while blue indicates the test set. . . . .	54
3.7	Examples of network-delineated calving fronts (red line) using all six datasets in the test sets. . . . .	59
3.8	An example showing the contrast enhancement and the improvement after applying histogram normalization. (a) is the original image with severe shadow problem. (b) is the zoom-in figure of the shadowed area (blue box). (c) shows the same area as (b) but after applying histogram normalization. Red lines in (b) and (c) show the corresponding network-delineated calving fronts. . . . .	60
3.9	Time series of calving front variations of the two branches of Jakobshavn Isbræ. Dashed vertical lines divide the time series into three phases (see text). . . . .	61
3.10	The time series of calving front variations of Kangerlussuaq. (b) is the zoomed-in figure within the black box in (a), showing the jumps (indicated by black bars) caused by large calving events. Dashed vertical lines divide the time series into two phases (see text). . . . .	62

3.11 Time series of calving front variations of Helheim. (b) is the zoomed-in figure within the black box in (a), showing the jumps (indicated by black bars) caused by large calving events. The solid blue dot in (b) indicates the position after a large calving event (Figure 3.12). Dashed vertical lines divide the time series into two phases (see text). . . . .	63
3.12 Images before (a) and after (b) a large calving event. Curves are network-delineated calving fronts. Blue dashed line in (b) is the same calving front in (a). Red arrow points at the tabular iceberg generated after the large calving event. Before the large calving event, a 4-km-long crevasse existed in the frontal area (blue box).	64
3.13 Example showing the stripe artifacts caused by terrain correction in SAR images. (b) shows the zoomed-in figure of artifacts within the blue box in (a). The red line is the calving front delineated by the network, showing the misidentifications of the artifacts as glacier ice. . . . .	67
3.14 Two examples showing the results with newly generated tabular icebergs. The well-trained network could (a) generate promising results, or (b) misidentify the newly generated tabular icebergs as parts of the glacier. Red lines show the calving fronts delineated by the well-trained network. . . . .	68

4.1	Meta-model showing hypothesized causal links from which a structural equation model was constructed. One-headed arrows indicate a directed relationship, and two-headed arrows indicate an undirected relationship. The numbers on the arrows are fictitious path coefficients. The absolute value of each number means the intensity of the corresponding causal links, and the sign means positive (+) or negative (-) relationship between two variables. . . . .	75
A.1	An example of the training dataset. The left is a training image, and the right one is its ground truth image where the black region is ice mélange and the white region is non-ice mélange (including both glacier and bedrock). The red line is the calving front we delineate manually. . . . .	77
A.2	An example showing how we use a reference image to delineate a smooth calving front on a winter image with obscure boundaries. (a) is the reference image and (b) is the image with obscure boundaries. (c) and (d) show the manually delineated calving fronts. The blue box in (e) shows the location of (a)-(d). . . . .	78
A.3	Two examples showing the validation of re-georeferencing. In both (a) and (b), the two lines show the manually delineated calving fronts from ours and the CCI. . . . .	79
A.4	An example of error estimation of the network-delineation. The green line is the calving front we manually delineate. The yellow line is the calving front delineated by the deep-learning network. The red zone indicates the error of our results, which is the area circled by the green and yellow lines. . . . .	80

# List of Tables

2.1	Retreat rates in area and equivalent length during different phases.	32
3.1	Advantages and disadvantages of SAR and optical images. . . . .	45
3.2	Summary of datasets used in this study. This table shows the satellite mission, band (SAR data only), nominal spatial resolution, total number of images, duration, nominal repeat cycle of each dataset. . . . .	47
3.3	The test errors (in meters) of different networks. Dark green indicates small test error. In the second column, “HN” means histogram normalization, “LS” means linear stretching, and “Non” means no histogram modification. The last three rows show the averages of test error weighted by each dataset’s number of images.	58
A.1	Test error of each image and their means. . . . .	81

# Chapter 1

## Introduction

### 1.1 Background

#### 1.1.1 Glacier front variations in Greenland

##### 1.1.1.1 Observations

Over the past two decades, the Greenland Ice Sheet has been losing its mass at a dramatic rate of  $258 \text{ Gt yr}^{-1}$ , contributing 26% of the global mean sea level rise [Bamber et al., 2018]. Both decreased surface mass balance (SMB) and increased ice discharge contribute to the mass loss [van den Broeke et al., 2017]. Ice discharge accounts for about half of the ablation from Greenland through calving processes [van den Broeke et al., 2009]. Changes in glacier front positions are good indicators for dynamic mass changes, as thinning and accelerating of glaciers are coupled with retreat [Khan et al., 2015; Joughin et al., 2008c,b; Howat et al., 2005].

Glacier front variations have been recorded for a century. [Warren, 1991] studied the front variations of 72 glaciers in West Greenland from 1940s/1950s to 1980s. [Bjørk et al., 2012] extract frontal variations of glaciers in southeast Greenland

from 1930s to 2012s by combining historical aerial images with modern satellite imagery. From 1992–2000 to 2000–2006, a marked increase in retreat rate of marine-terminating outlet glaciers in northern, eastern, and southeastern Greenland has been observed [Moon and Joughin, 2008]. Greenland outlet glaciers retreated at  $-110 \text{ m yr}^{-1}$  over 2000–2010 [Howat and Eddy, 2011; Murray et al., 2015]. Meanwhile, 37 glaciers in central-east Greenland retreated 1.6 km on average, with nearly half of them retreating 1 km or more [Walsh et al., 2012].

The three largest glaciers, namely Jakobshavn Isbræ, Kangerlussuaq, and Helheim, have retreated more intensely among all the retreating glaciers (Figure 1.1). In 2000, Jakobshavn Isbræ started to retreat progressively, which resulted in nearly complete disintegration of its 15-km-long floating ice tongue by 2003 [Joughin et al., 2004]. Then, Jakobshavn Isbræ kept retreating 16 km from 2002 to 2008 [Rosenau et al., 2013], and 4 km from 2009 to 2014 [Joughin et al., 2014]. The behaviors of Kangerlussuaq and Helheim changed markedly between 1999 and 2002, and started to retreat greatly. Between 2001 and 2005, Helheim retreated 6.8 km [Howat et al., 2005], while Kangerlussuaq retreated more than 4 km from April 2004 to April 2005 [Luckman et al., 2006].

### 1.1.1.2 Potential mechanisms and remaining questions

In general, calving front variations are governed by various local controlling factors such as buoyancy forces, submarine melting, basal geometry, ice mélange strength, and meltwater runoff [Benn et al., 2017; Cowton et al., 2018]. Figure 1.2 summarizes the possible mechanisms that control the glacier front variations. The frontal ablation in Greenland is governed by two main mechanisms: buoyancy-driven calving [Van Der Veen, 1996] and submarine melting [Luckman et al., 2015; Fried et al., 2015]. Buoyancy-driven calving is an important process on large, fast-flowing outlet glaciers [Wagner et al., 2016]. Based on high-

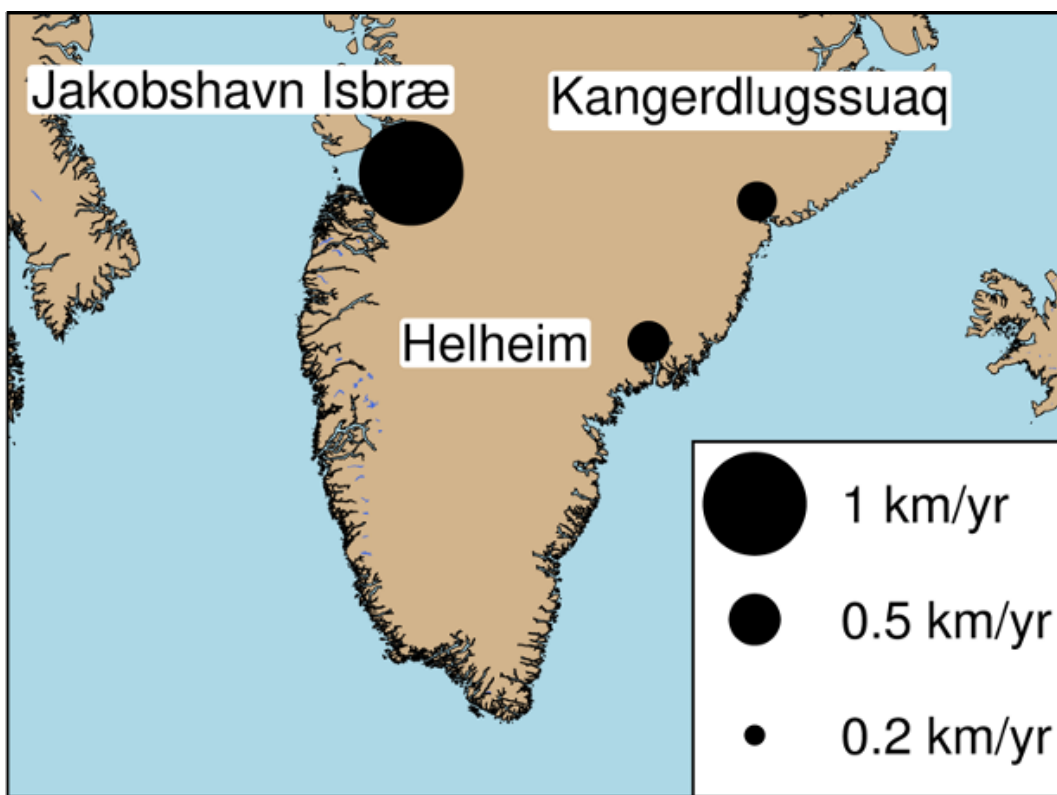


Figure 1.1: A map showing retreat rates of the three largest glaciers in Greenland from 2000 to 2010. The data is derived from [Murray et al., 2015].

temporal- and spatial-resolution digital elevation models (DEMs), [James et al., 2014] observed the buoyancy-driven lifting of the front before the iceberg detaches and glacier retreating. For slow-flowing glaciers, submarine melting could have significant control on terminus position since warm ocean water are capable of inducing submarine melt rates comparable with ice velocity [Bartholomaeus et al., 2013; Luckman et al., 2015; Fried et al., 2015]. In addition to two ablation mechanisms, retreat could also be influenced by basal geometry, ice mélange strength, and surface runoff. [Catania et al., 2018] found that in central-western Greenland, the amount of retreat of glacier is related to the length of the overdeepening behind the terminus at retreat onset from 1985 to 2016. [Amundson et al., 2010] suggested that the seasonality of Jakobshavn Isbræ's front may be driven by ice

mélange strength after it lost the ice tongue in 2003. Meltwater drains through a glacier and discharges subglacially to form buoyant plumes, which enhances submarine melting at glacier termini [Jenkins, 2011; Fried et al., 2018; Carroll et al., 2015].

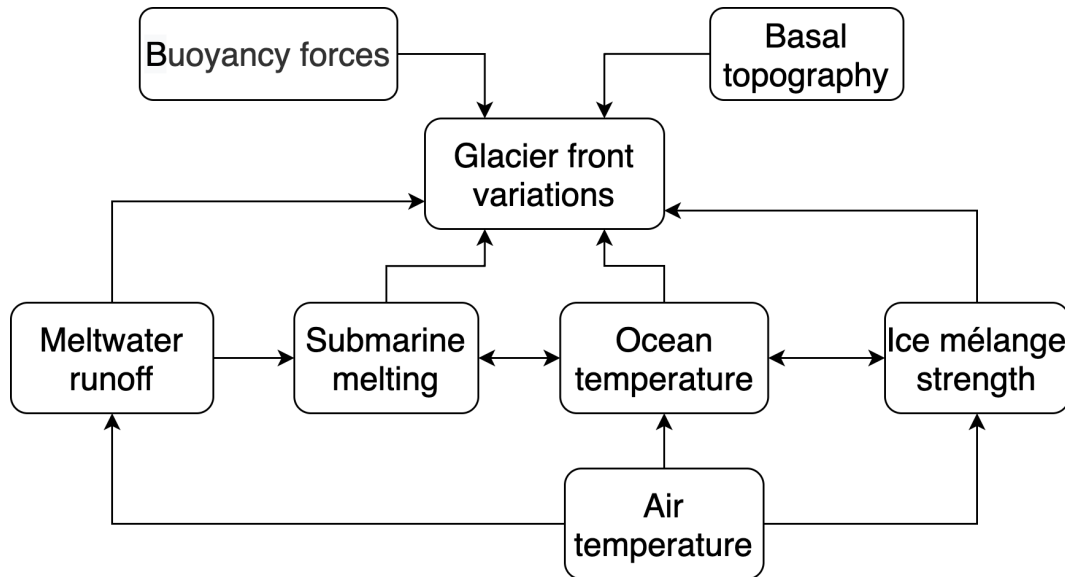


Figure 1.2: Diagram summarizing potential mechanisms that control front variations. One-headed arrows indicate a directed relationship, and two-headed arrows indicate an undirected relationship.

### 1.1.1.3 Development of remote sensing dataset

Remote sensing data provide the key observations of glacier's front variations. With the continuous accumulation in the past decades and in recent space missions, the data volume of remote sensing imagery in the polar regions has increased dramatically. Figure 1.3 summarizes some operating satellites since 2000, and the following gives the detailed information, including their operating period, spatial resolution, temporal resolution, and sensors.

In 1995, RADARSAT-1 was launched with the repeat cycle of 24 days. It car-

ried a C-band Synthetic aperture radar (SAR) with the highest resolution of 10 meters. The satellite had been collecting data for 17 years until 2013, which is much longer than its projected lifetime of five years. In 1999, Landsat-7 was launched with the repeat cycle of 16 days. It carried a panchromatic band with 15 m resolution; visible, near-infrared, and mid-infrared bands with 30 m resolution; and a thermal infrared band with 60 m resolution. However, on May 31, 2003 the Scan Line Corrector (SLC) in the ETM+ instrument failed, making the images have no-data stripes. Landsat-8 was launched in 2013 and Landsat-9 will be launched in 2021. The panchromatic band has the best spatial resolution for all the Landsat satellites. The Advanced Spaceborne Thermal Emission and Reflection Radiometer (ASTER) is a Japanese instrument onboard Terra satellite launched in 1999 and has been collecting data since February 2000. The repeat cycle of ASTER is 16 days, and it has 14 bands of the electromagnetic spectrum, ranging from visible to thermal infrared light. The spatial resolution ranging from 15 (near infrared and visible) to 90 m. Envisat was launched in March 2002, and the mission ended in May 2009. It carried a C-band SAR sensor with the best resolution of 30 m, and the repeat cycle is 35 days. ALOS-1 & -2 were launched in 2006 and 2014, respectively, and ALOS-1 ended its mission in 2011. They carry the Phased Array type L-band Synthetic Aperture Radar (PALSAR) with the best resolution of 10 m. The revisit times are 46 days for ALOS-1 and 14 days for ALOS-2. The German satellite TerraSAR-X (TSX) was launched in June 2007 and carries an X-band SAR sensor. It has a high spatial resolution (3.3 to 3.5 m) and high temporal resolution (11 days). The Sentinel-1A & -1B satellites were launched in February 2014 and April 2016, respectively, and carry C-band SAR sensors. Each of these two satellites has a 12-day repeat cycle and their combination offers a 6-day repeat. Sentinel-1 has four operational modes, namely Strip Map (SM) mode, Interferometric Wide Swath (IW) mode, Extra

Wide Swath (EW) mode, and Wave (WV) mode. Among these modes, IW is the best choice considering both spatial coverage and resolution (5 by 20 m). The Sentinel-2A & -2B satellites were launched in June 2015 and March 2017, respectively. Each of them has a 10-day repeat cycle and the combination offers a 5-day repeat. They carry multi-spectral instruments (MSI) with 13 spectral channels in the visible/near infrared (VNIR) and short wave infrared spectral range (SWIR). Among them, the visible and near infrared bands have the best spatial resolution (10 m).

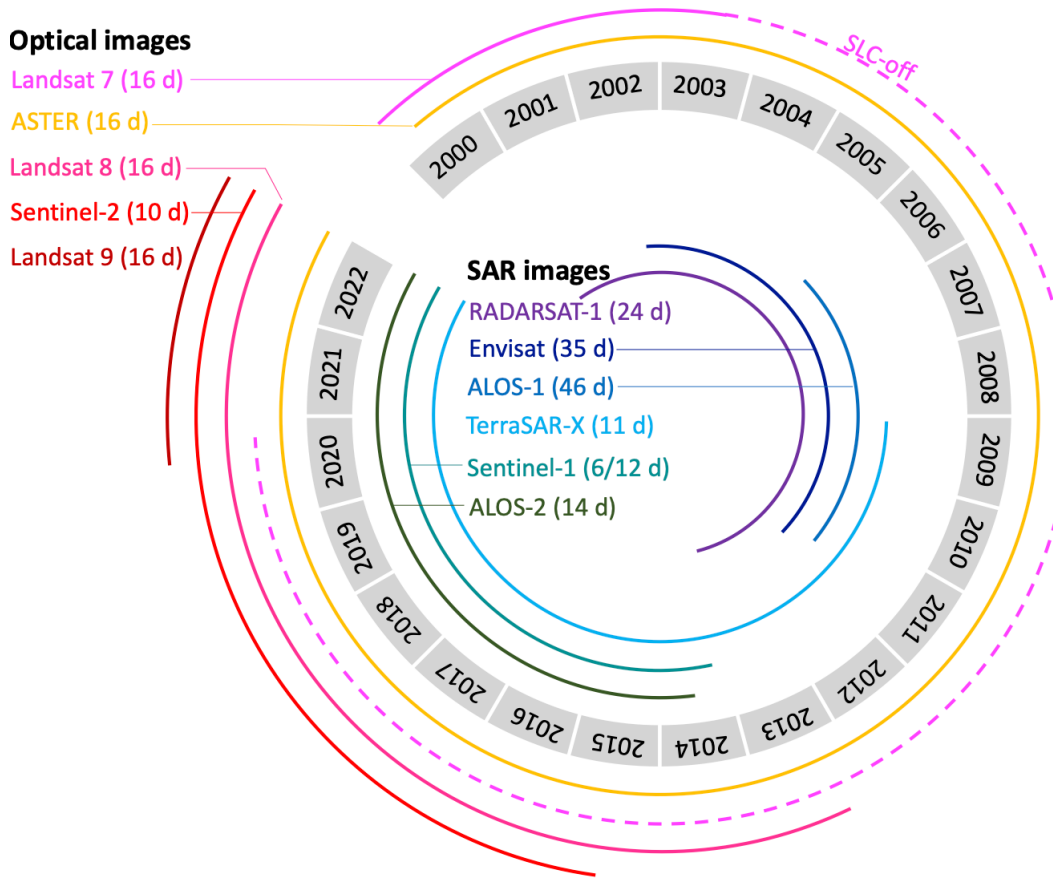


Figure 1.3: Remote sensing datasets introduced in this dissertation. Optical and SAR images are groups within outer and inner arcs, respectively. Numbers in the parentheses are nominal revisit times in days. Landsat 7 images obtained after 2003 may still be useful, despite suffering from defects due to the failure of its Scan Line Corrector (SLC). Landsat 9 is scheduled to launch in 2021.

Integrating multiple remote sensing yields a massive number of images. To have a rough estimation of data volume, we divide the days of a year (356.25) by the repeat cycle of the satellite to calculate the number of images. Assuming that a glacier is covered by all the operating satellites that we list (Figure 1.3), the total number of images would be around 200 in 2017. Considering that Greenland has more than 200 outlet glaciers, we could have hundreds of thousands of images when conducting a multi-decadal investigation. The increased data volume of remote sensing imagery indeed provides the foundation of a comprehensive investigation of front variations in both spatial and temporal scales. However, it is impractical to produce such a comprehensive front dataset by manual delineation. Therefore, we need to automate it.

### 1.1.2 Previous mapping efforts

#### 1.1.2.1 Manual delineation

Most of the previous studies of glacier front variations were based on manual delineation [Howat et al., 2010; Schild and Hamilton, 2013; Lea et al., 2014; Carr et al., 2017; Catania et al., 2018; Cowton et al., 2018]. Some studies that used multiple remote sensing datasets have been regionally specific [e.g., Walsh et al., 2012; Fried et al., 2018]. A few studies that investigated glacier front variations across the entire Greenland Ice Sheet but limited in specific datasets. [Moon and Joughin, 2008] examined ice front changes of 203 glaciers in Greenland using SAR mosaics derived from ERS-1 images. Using Landsat imagery, [Howat et al., 2011] measured changes in front positions of 210 marine-terminating glaciers in Greenland spanning nearly four decades, [Murray et al., 2015] mapped 199 Greenland glaciers between 2000 and 2010, and [Bunce et al., 2018] digitized 276 outlet glaciers in the northwest (100) and southeast (176) regions of Greenland between

2000 and 2015. Combining both ASTER and Landsat-7 images, [Walsh et al., 2012] mapped 37 marine-terminating glaciers in the central-east Greenland from 2000 to 2010. Three recent major projects have combined multiple datasets to generate ice front products: the Greenland Ice Sheet Climate Change Initiative (CCI) product includes calving fronts for 28 glaciers derived from ERS, Sentinel-1 and Landsat images; data produced by the Programme for Monitoring of the Greenland Ice Sheet (PROMICE) include front lines for 47 glaciers derived from Landsat, ASTER, and Sentinel-2 images [Andersen et al., 2019]; the Greenland Ice Mapping Project (GIMP) uses Landsat-8, RADARSAT-1, Sentinel-1 images to delineate calving fronts for 238 glaciers.

### 1.1.2.2 Feature extracting methods

Compared with manual delineation, automated mapping method is superior due to its greater productivity and lower cost. Feature-extracting methods have been developed to automatically delineate glacier front positions from both optical and SAR images. [Sohn and Jezek, 1996] designed a method to extract the ice sheet margin by applying Roberts edge extractor to ERS-1 SAR images. By integrating the Canny edge detection and locally adaptive thresholding methods, [Liu and Jezek, 2004] extracted a complete coastline of Antarctica from RADARSAT images. [Seale et al., 2011] automated the identification of glacier fronts from daily MODIS images by combining the Sobel and brightness profiling methods. [Krieger and Floricioiu, 2017] combined the Canny edge detector with a shortest path algorithm to detect the front position of Zachariæ Isstrøm from TSX and Sentinel-1 images. These feature-extracting methods require extensive prior knowledge and experience. Moreover, when applying to different glaciers or remote sensing images, case-specific modifications to these methods are required because of changes glacier textures due to variations in snow cover, wetness,

and geometric properties such as roughness, grain size, and internal structure. Therefore, in the big data era, deep learning techniques are more appropriate to automate the extraction of glaciological features from diverse datasets and complex glacier systems across Greenland.

### 1.1.2.3 Deep-learning-based methods

Deep learning, building on multiple layers of convolutional neural networks, is used in many fields such as computer vision, artificial intelligence, and Earth sciences and has outperformed most conventional machine learning methods [e.g., [LeCun et al., 2015](#)]. Section 1.2 will provide a brief introduction to deep learning. Two deep learning-based methods have been developed to automate the delineation of glacier fronts and showed the network's generalization by testing on glaciers that are not included in training [[Mohajerani et al., 2019](#); [Baumhoer et al., 2019](#)]. Both used the same deep learning network, U-Net, and were restricted to a specific dataset. Despite the similarities, these two works are different in datasets, strategies of classifications, and workflow. For example, [[Mohajerani et al., 2019](#)] semantically classified Landsat images into calving front and non-calving front regions and extracted fronts using a lowest-cost path search algorithm. [[Baumhoer et al., 2019](#)] segmented Sentinel-1 images into ocean and glacier and then extracted boundaries. [[Baumhoer et al., 2019](#)] also combined different polarizations and elevation information to obtain more accurate results. Regarding workflow, [[Mohajerani et al., 2019](#)] adjusted images of each glacier to make all the glaciers flow in the same direction to reduce the diversity brought by multiple glaciers. Therefore, their network could produce promising results by only training limited examples. By splitting images into tiles and merging after, the work of [[Baumhoer et al., 2019](#)] could handle images with different sizes and keep the original spatial resolution of SAR images.

## 1.2 Deep Learning

### 1.2.1 Basic concepts of deep learning

Deep learning is the method based on multi-layer neural networks, which contains massive internal adjustable parameters, or weights and biases (e.g.,  $w$  and  $b$  in Figure 1.4). The most common form of deep learning is supervised learning, which requires training data prepared by human (or is supervised by human). For the task of classifying images as a person, a dog, or a cat, we first collect a large amount of images of people, dogs, and cats, each labeled with its category. During the training, the network takes these pictures as input and output a vector of their category. Before the training, it is unlikely for the network to output what we desire. We use a cost function to measure the difference between the desired and output categories. By modifying the weights and biases, or learning, the network can minimize the difference.

The network modifies its internal adjustable parameters by backpropagation. Figure 1.4 illustrates how forward propagation and backpropagation are done using a simple neural network. In the forward propagation, we first compute the total input  $z$  to every unit in each layer, which is a weighted sum of the outputs of the units in the layer below. Then we use a non-linear active function  $f$  to get the output of the unit. Without the non-linear active function, multiple layers will collapse into a single layer due to the linearity. For different layers, the active functions could be different, including rectified linear unit (ReLU)  $f(z) = \max(0, z)$ , sigmoid function  $f(z) = \frac{1}{1+e^{-x}}$ , hyperbolic tangent function  $f(z) = \frac{e^x - e^{-x}}{e^x + e^{-x}}$ , and so on. In the backpropagation, in each hidden layer, we first compute the error derivative of the output ( $E/y$ ), which is a weighted sum of the error derivatives with respect to the total inputs to the units in the layer above.

For the output layer, the derivative of the output is the difference between output ( $y_l$ ) and ground truth ( $t$ ) if we choose cost function as  $E = 0.5 * (y_l - t)^2$ . Then, we calculate the derivative of the input ( $E/z$ ) and the derivative of each weight ( $E/w$ ). With the derivative of each weight, we could update weight value with a given learning rate ( $lr$ ).

In addition to internal adjustable parameters, we also have fixed parameters, namely hyperparameters (e.g., the number of layers, the unit numbers in each layer, learning rate, and so on). When building a network, the setting of hyperparameters is essential, and we need to conduct numerous experiments to find the best configuration. In the deep learning convention, the whole dataset is separated into three subsets, namely, training, validation, and test. The training set is for optimizing the network's internal adjustable parameters, while the validation set is for optimizing the network's hyperparameters. The test set is for providing an independent estimation of the network's accuracy.

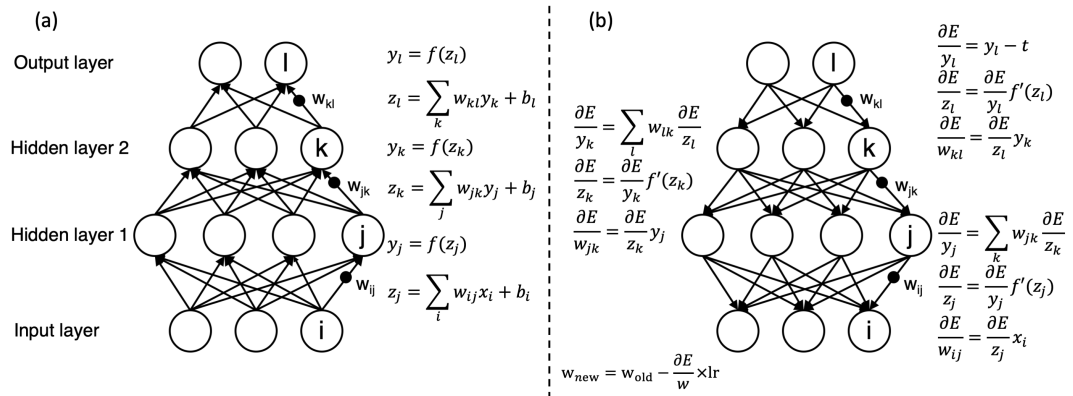


Figure 1.4: Illustration of forward propagation (a) and backpropagation (b) using a four-layer neural network. The circles show the units in each layer, and the connected black dots are weights. Arrows refer to the related units for getting the next layer. The equations aside show how we do the calculation.  $x$  refers to the input of the input layer,  $z$  means the input of other layer,  $y$  is the output of each layer,  $E$  is the cost function,  $lr$  is the learning rate, and  $t$  is the ground truth. The subscript  $i$  means input layer,  $j$  means hidden layer 1,  $k$  means hidden layer 2, and  $l$  means output layer. This figure is adapted from [LeCun et al., 2015].

### 1.2.2 Convolutional neural network

Convolutional neural network (CNN) is designed to process data in the form of multiple arrays such as images. The example network given in the previous subsection connects all the units of the previous layer to the units in the next layer. When processing images, a network with full connectivity requires an enormous amount of adjustable parameters. The consumption of computational power would be significant and even unrealistic.

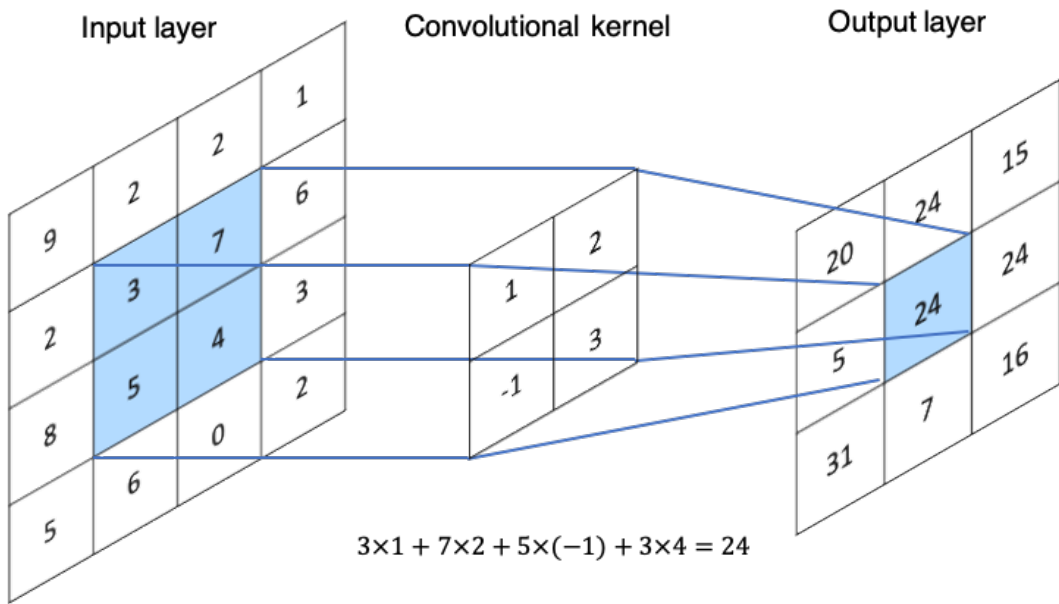


Figure 1.5: Illustration of a simple convolution with a  $2 \times 2$  kernel. The output layer unit is the weighted sum (with the weights being the values of the kernel) of corresponding input layer units. The equation at the bottom shows the convolution calculation for the central unit of the output layer.

By connecting adjacent layers through convolutional kernels, CNN can take advantage of local connections, shared weights, and the use of many layers. More specifically, a convolutional layer's output is the weighted sum of the input layer's local patches and convolutional kernel (Figure 1.5). The reason for the convolutional design is twofold. First, in images, local groups of values are often highly

correlated, forming distinctive local features that are easily detected. Second, features in an image can appear repeatedly. Therefore, similar features at different locations could share the same weight for detecting the same pattern. Moreover, the multi-layer structure of CNN allows the progressive of feature extraction; low-level features are extracted in the top layers and compose high-level features in deeper layers. Backpropagating gradients through a CNN is as simple as through a regular deep network, allowing all the weights in all the convolutional kernels to be trained.

### 1.2.3 Applications of deep learning to remote sensing

Despite the complexity of remote sensing datasets, deep learning has made important breakthroughs in tackling satellite images [Zhu et al., 2017]. Here, we only briefly introduce some representative applications of deep learning to remote-sensing-related studies. Using satellite images, deep learning has been applied in many fields including but not limited to object and change detection [Anantrasirichai et al., 2018; Huang et al., 2020], differentiation [Bentes et al., 2016], classification [Kussul et al., 2017], parameter inversion [Wang et al., 2016; Cooke and Scott, 2019], and super-resolution [Leong and Horgan, 2020]. More specifically, [Anantrasirichai et al., 2018] applied CNN to detect volcanic deformation from interferometric SAR (InSAR) images. [Huang et al., 2020] used deep learning to map retrogressive thaw in Tibetan Plateau from CubeSat images. [Bentes et al., 2016] applied a CNN to ship-iceberg differentiation, tested on TSX images. Using both Landsat-8 and Sentinel-1A images, [Kussul et al., 2017] classified land cover and crop types with deep learning technology. CNN can also be used to estimate sea ice concentration from SAR images [Wang et al., 2016; Cooke and Scott, 2019]. In addition to CNN, Generative Adversarial Network

(GAN), another deep learning branch, can also be applied to remote sensing images [Leong and Horgan, 2020]. Based on GAN, [Leong and Horgan, 2020] combined low-resolution bed elevation, surface elevation, ice velocity, and snow accumulation to provide a super-resolution bed topography of Antarctica.

### 1.3 Objectives and hypotheses

We aim to develop a generalized method towards automated delineation of the glacial front at major outlet glaciers in Greenland from satellite imagery. This is a versatile deep learning-based method to take on the diversity introduced by multi-sensor remote sensing datasets and complex glacier systems. We will also quantify and investigate the variations of calving front positions. More specifically, this research aims:

1. To develop a deep-learning-based method that can automatically delineate calving fronts of Greenland outlet glaciers from multi-sensor and multi-temporal remote sensing images;
2. To produce time series of front position changes at the three largest glaciers in Greenland using seven remote sensing datasets;
3. To investigate the controlling factors, mechanisms, synchronous, and asynchronous behaviors of frontal variations.

This dissertation tests the following hypotheses:

1. Deep learning can be successfully applied to automatically delineating calving fronts, and the well-trained network can be applied to glaciers and datasets that are not included in the training.
2. The accuracy of network-delineated fronts is close to that of manual-delineated ones.

3. Basal topography has a substantial influence on the glacier retreat, and neighboring branches or glaciers could behave synchronously due to regional environment forcings, and asynchronously due to glaciological settings such as floating conditions.

## 1.4 Road map of dissertation

In this dissertation, we first apply U-Net, a deep learning architecture, to automate the delineation of calving fronts of Jakobshavn Isbræ from TSX images (Chapter 2, Zhang et al., 2019). Small errors suggest that the accuracy of a well-trained network can be close to the human level. However, all these works are limited to a specific dataset and study area, which is not general enough to be applied to multi-sensor remote sensing imagery and different glaciers with diverse texture and context. In the second study, we increase the accuracy, generalization, and robustness of the deep-learning-based method in two ways (Chapter 3). First, we apply a more advanced deep-learning architecture, namely DeepLabv3+, for solving the diversity introduced by the multi-sensor datasets and complex glacier system. Second, we adopt histogram normalization to homogenize the diversity of multi-sensor remote sensing imagery. With the more advanced method, we integrate seven remote sensing datasets into a single deep learning network and automate the delineation of the calving fronts of Jakobshavn Isbræ, Kangerlussuaq, and Helheim using Envisat, TSX, Landsat-8, Sentinel-1 & -2, and ALOS-1 & -2 images. In Chapter 2, we discuss the influence of basal topography on the observed front variations of Jakobshavn Isbræ. We also discuss the synchronous and asynchronous dynamic behaviors between neighboring branches or glaciers in Chapter 3. In Chapter 4, we address the conclusions of this dissertation and possible directions for future work.

## 1.5 Innovative merits and potential impacts

This dissertation develops an innovative deep learning-based method to automatically delineate glacier fronts. In the first trial, we develop a framework including a series of pre-processing and post-processing procedures, which enables the application of a deep-learning network, U-Net. In the second work, we further increase the generalization and robustness of our method by applying a more advanced network, DeepLabv3+, and histogram normalization. For the first time, we integrate seven remote sensing datasets into a single deep learning network. Moreover, our method can be applied to a glacier and datasets that are not included in the training.

Our method has the potential to provide an unprecedentedly comprehensive dataset, which will help to better understand the frontal dynamics. In addition to the remote sensing images obtained during the study period (2002–2019), our method can also be applied to images collected by both future and historical space missions, saving a tremendous number of manual practices. The effectiveness and transferable nature of deep learning ensure that our innovative method can also be applied to other glaciers around the world. In addition to front positions, our method can extend to mapping other glaciological features and processes including, not limited to, icebergs, crevasses, and supraglacial lakes, benefitting broader glaciology communities.

---

End of chapter.

## **Chapter 2**

# **Automatically delineating the calving front of Jakobshavn Isbræ from multi-temporal TerraSAR-X images: a deep learning ap- proach**

This chapter presents the study that used a deep learning-based method to automatically delineate glacier calving fronts. Applying U-Net, a deep learning architecture, to multi-temporal Synthetic Aperture Radar images taken by the TerraSAR-X satellite, we automate the delineation of the calving front positions at Jakobshavn Isbræ from 2009 to 2015. The results show that the front variations of Jakobshavn Isbræ had a three-phases inter-annual signal. We suggested that the basal topography has strong influence on the front variations. Our results have a small test error of 38 meters and are consistent results with manually delineated products generated by the Greenland Ice Sheet Climate Change Initiative project. Demonstrating through this successful case study on Jakobshavn Isbræ, we prove the feasibility of applying deep learning to automatically delineating glacier calving front.

## 2.1 Introduction

Glacier retreating is one of the processes that control the recent speedups of Greenland’s tidewater glaciers [King et al., 2018]. As glacier retreats, it accelerates to compensate for the loss of downstream buttress. Glacier dynamic instabilities, as suggested decades ago by [Meier and Post, 1987], play an essential role as the glaciers retreat over depressions in the bedrock topography. For example, [Joughin et al., 2008b] indicated that dynamic instabilities caused Helheim and Kangerdlugssuaq Glaciers to speed up as they retreated into an overdeepened basin whose bed is retrograde between 2001 and 2006. Examining 276 marine-terminating outlet glaciers, [Bunce et al., 2018] concluded that bed geometry is an important control on the timing and magnitude of glacier retreat. With a comprehensive calving front dataset, we could investigate the influence of bed geometry on glacier retreat in detail.

Here we aim to design a method to automatically delineate a glacier calving front from multi-temporal TSX images based on deep convolution neural networks (DCNNs). More specifically, we delineate the glacier calving front of Jakobshavn Isbræ (Figure 2.1a) and quantify its seasonal and inter-annual variations. With this new set of observations, we investigate the possible link between calving front variations and bed elevation.

DCNNs are a class of the deep learning methods, and have made important breakthroughs in image processing. DCNNs can discover both low-level (e.g., edges, corners, and lines) and mid-level features (e.g., shapes, sizes, and locations) [Sun et al., 2014; Zhang et al., 2015]. Recently, some studies have used DCNNs on high-resolution SAR images to perform classification tasks [Geng et al., 2015; Huang et al., 2017]. These studies unanimously agree that DCNNs outperform traditional classification methods on SAR images.

We use TSX images due to their high temporal resolution (11 days), high spatial resolution (3.3 to 3.5 meters), and ability to penetrate cloud cover. These high-temporal-resolution images have been acquired in all seasons and allow us to investigate calving front variations with a high degree of continuity and consistency. With these high-spatial-resolution images, we can easily digitize the calving fronts (known as “ground truth” in the context of deep learning), and verify the accuracy of the DCNN. Using SAR images can avoid the cloud cover problem associated with optical images such as the Landsat-8 image shown in Figure 2.1b.

## 2.2 Jakobshavn Isbræ

Jakobshavn Isbræ, located in central-west Greenland, is one of the largest and fastest tidewater glaciers in the world. In Jakobshavn, the ice flows westward to the ocean and divides into two branches near the coast (Figure 2.1a). Before summer 2004, these two branches merged and flowed into the Kangia fjord. Afterwards, as the glacier retreated, the two branches became disconnected [Bondzio, 2017]. During the past few years, Jakobshavn Isbræ has undergone dramatic acceleration as the glacier has retreated and thinned [Joughin et al., 2008c, 2012]. Jakobshavn’s calving front retreated 16 km between 2002 and 2008 [Rosenau et al., 2013]. This glacier alone has contributed nearly 1 mm to the global sea level rise from 2000 to 2011 [Howat et al., 2011].

Observations have shown that the calving front variations were correlated with the glacier velocity changes in Jakobshavn Isbræ. In 1998, the glacier sped up by 18% in its frontal regions, coinciding with the initial retreat of the ice tongue [Thomas, 2004; Luckman and Murray, 2005]. The glacier doubled its speed by spring 2003, when nearly the entire floating ice tongue had disintegrated [Joughin

et al., 2004]. After the loss of this ice tongue, the glacier's velocity fluctuated seasonally from 2004 to 2007 [Joughin et al., 2008a]. The glacier slowed down when it was advancing, and sped up when it was retreating [Joughin et al., 2012]. The variations of Jakobshavn's calving front are also strongly influenced by the presence of ice mélange, namely a mixture of calved icebergs and sea ice (Figure 2.1a). The seasonal variation of the calving front in Jakobshavn Isbræ is well correlated with the growth and recession of sea ice in the Kangia fjord [Sohn et al., 1998; Joughin et al., 2008c]. Temporal variations of the ice mélange strength can also control the timing of calving events and influence the evolution of the calving front position [Amundson et al., 2010].

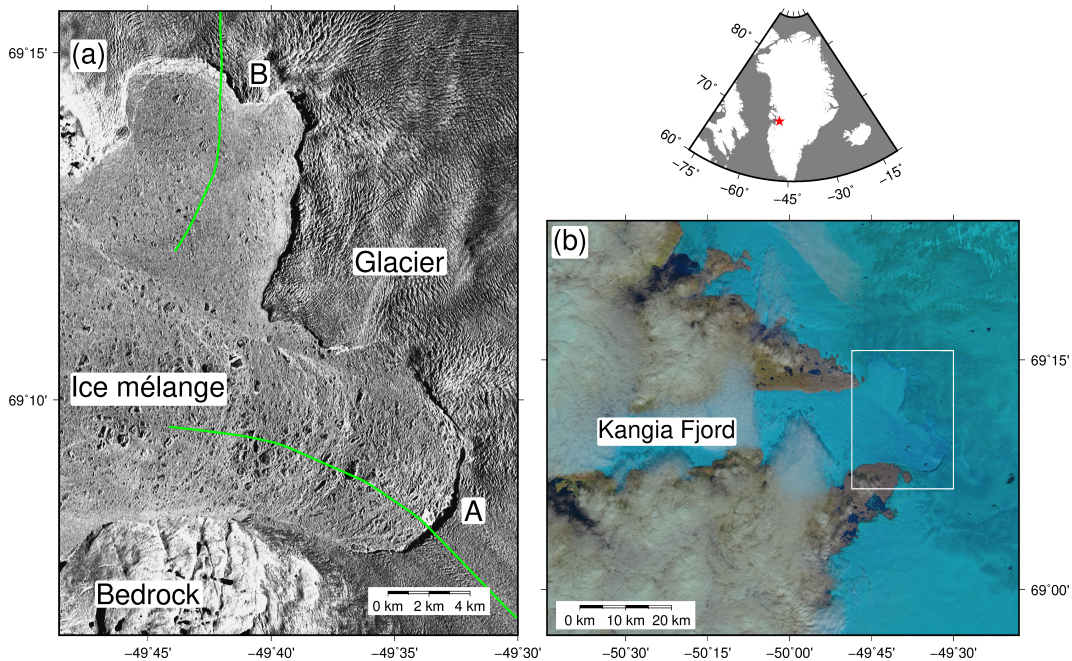


Figure 2.1: (a) TerraSAR-X image taken on 11th July 2015 showing the frontal area of Jakobshavn Isbræ. Its two branches are labeled as 'A' and 'B'. The green lines indicate the location of the bed elevation profiles shown in Figure 2.9. (b) Landsat-8 image taken on 13th July 2015. The white box shows the area illustrated in Figure 2.1a.

Our study area covers a  $14 \times 18$  km section of the frontal area of Jakobshavn, and

includes bedrock, ice mélange, and glacier regions. We restrict the extent of the study area to reduce the computational costs, while also ensuring the coverage of all the calving fronts within our investigation period (2009–2015, determined by the TSX images we have access to). We classify our study area into two classes: ice mélange and non-ice mélange regions (including both glacier and bedrock regions). We delineate the boundaries between these two regions and retrieve glacier calving fronts. The repetitive texture of crevasses in the glacier region clearly distinguishes it from ice mélange, where icebergs are distributed discretely. It is easy to identify the bedrock region because of the distinct bedrock texture, including cracks and land-based lakes.

## 2.3 TerraSAR-X images and pre-processing

The German SAR satellite TerraSAR-X was launched in June 2007 and carries an X-band SAR sensor. In this study, we use TSX images taken in both ascending and descending orbits and in stripmap imaging mode. We use the enhanced ellipsoid corrected (EEC) products, which are multi-looked, projected and resampled to the WGS84 reference ellipsoid. We use 159 images in total, taken between April 16<sup>th</sup>, 2009 and December 23rd, 2015. We apply three pre-processing procedures including despeckling, multi-looking, and re-georeferencing. Figure 2.2 shows an illustrative example of our pre-processing workflow, which we will describe below in detail.

Because the quality of SAR images is adversely affected by the speckle noise (Figure 2.2a), we apply the median blur filter to mitigate the speckle noise (Figure 2.2b) and then multi-look the filtered images to reduce their size by 25 times (Figure 2.2c). The median blur filter is widely used in image processing and is particularly effective for speckle noise. With the despeckled images, we average

five neighboring pixels (vertically and horizontally) by using Geospatial Data Abstraction Library (GDAL) package ([www.gdal.org](http://www.gdal.org)). Moreover, both despeckling and multi-looking can smooth images without the loss of essential information for delineating the calving fronts. After despeckling and multi-looking, the pixel size of our images is six meters. We choose the EEC products because they include topographic correction and are the standard geocoded products of TSX [Roth et al., 2004]. However, even for the EEC products, we observe that the geocoding information for our study area is inaccurate. First, overlaying the EEC images on Google Earth, we note obvious offsets between these two. Second, the geocoding information is inconsistent in different orbit directions of EEC products. Therefore, we need to re-georeference the EEC products. For the images we have, we observe that the images in the same orbit direction, we apply the same thin plate spline transformation using the GDAL package.

## 2.4 Deep Learning and post-processing

DCNNs are a class of neural networks that consist of numerous convolutional layers, each of which contains learnable weights and biases. A network's architecture refers to its overall structure, including the number of units and layers the network has and how they are connected. Here, we use the U-Net architecture, which has achieved outstanding performance in biomedical segmentation applications and is among the best methods in image segmentation [Ronneberger et al., 2015]. This network is fast, taking less than a second on a mainstream graphics processing unit (GPU) to segment a  $512 \times 512$  image. The U-Net architecture consists of a contracting path and an expansive path (Figure 2.3). The contracting path consists of repeated application of two  $5 \times 5$  convolution layers, each followed by a batch normalization layer and a leaky rectified linear unit (LeakyReLU) acti-

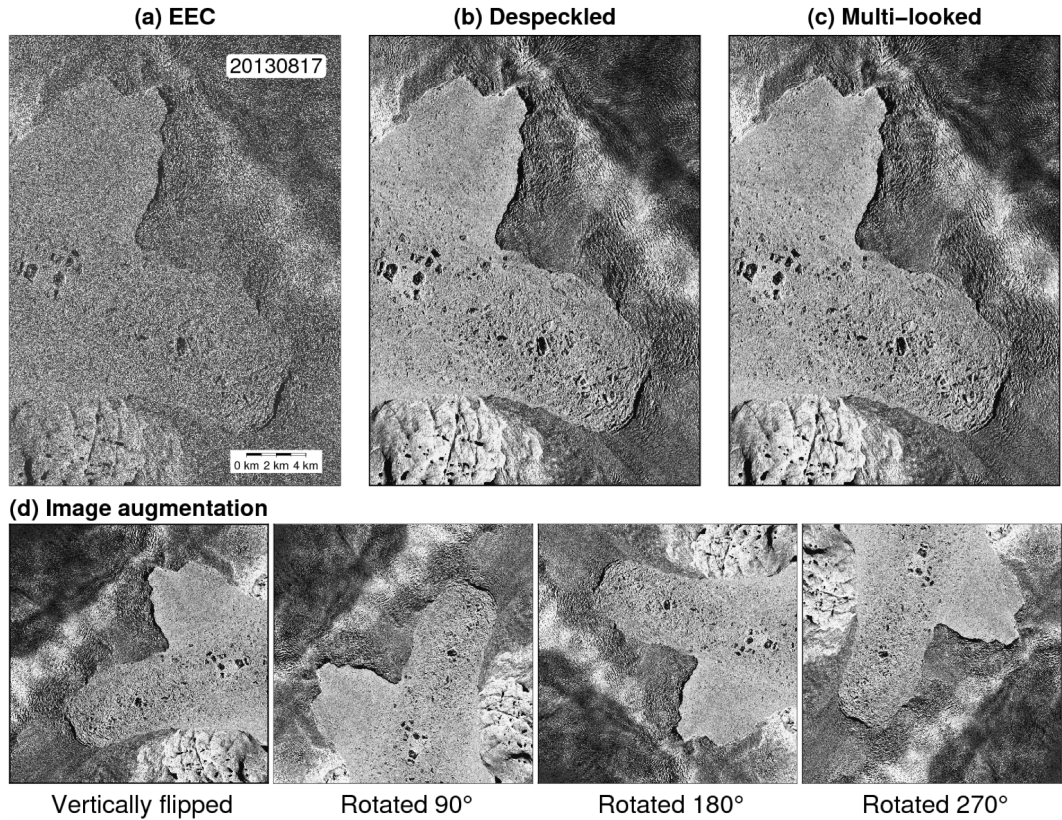


Figure 2.2: A set of examples of TerraSAR-X data pre-processing and preparation, including (a) the EEC product, (b) despeckled image after reducing the speckle noise, (c) multi-looked image after decreasing the image size, and (d) images after vertically flipping and rotating Figure 2.2c by 90°, 180°, and 270°, respectively. For ease of presentation, the images in Figure 2.2d are not to scale with (a)–(c).

vation function, and  $2 \times 2$  max pooling operation for downsampling feature maps and doubling the number of feature channels. Every step in the expansive path consists of a  $4 \times 4$  up-convolution layer that upsamples the feature map and halves the number of feature channels, a concatenation with the corresponding feature map from the contracting path and two  $5 \times 5$  convolution layers, each followed by a batch normalization layer and a LeakyReLU activation function. The final layer is a  $3 \times 3$  convolutional layer with Sigmoid activation function to get the final segmentation patch. We utilize relatively large convolution kernel size ( $5 \times 5$ ) to

obtain smoother calving fronts. We use LeakyReLU activation functions with a slope of 0.1 below zero, which allows for small, non-zero gradient when the unit is not active [Maas et al., 2013], making optimization potentially more robust. We use binary cross-entropy (BCE) between the ground truth images, and the network outputs to measure the training error because it avoids the problem of slow learning (the training loss decreases slowly) [Goodfellow et al., 2016]. We use adaptive moment estimation max (AdaMax) [Kingma and Ba, 2014] as the optimizer with a learning rate of 0.0001 and an L2 regularization factor of 0.00001.

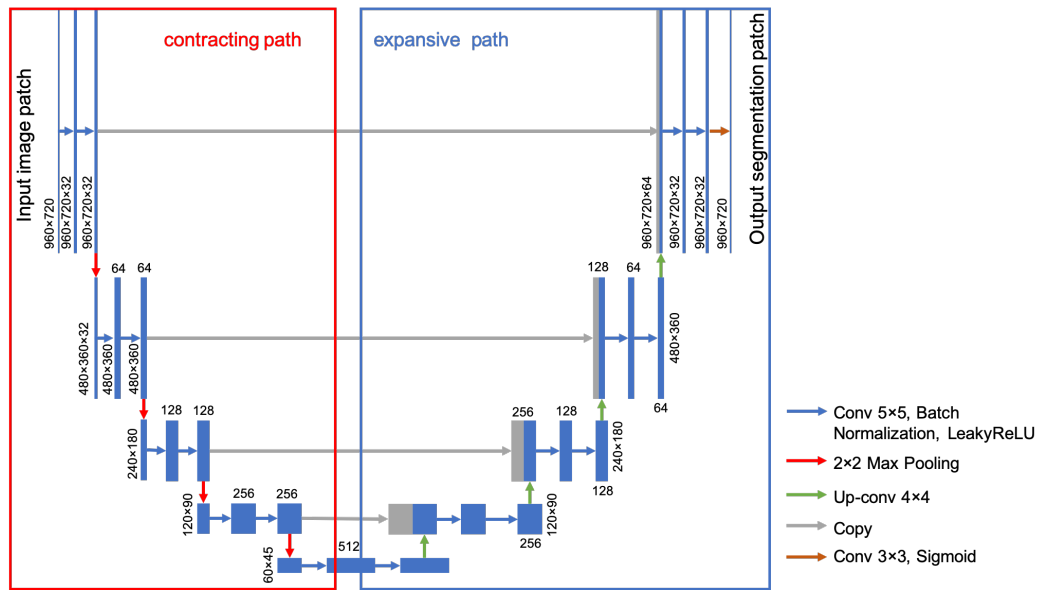


Figure 2.3: The Architecture of the U-Net. The red box indicates the contracting path and the blue box indicates the expansive path. Each solid blue box corresponds to a multi-channel feature map. Gray solid boxes represent copied feature maps. The length, width, and height of each layer correspond to the pixel dimensions and the number of feature channels respectively. Arrows with different colors denote the different operations. This figure is adopted from [Ronneberger et al., 2015]

The proposed framework for using deep learning to delineate the calving fronts is summarized in Figure 2.4. We separate all the SAR images into a training-validation dataset (75 images) and a test dataset (84 images). In the training-

validation dataset, we randomly choose 90% as training data and take the rest as validation data. The validation dataset is for minimizing overfitting and tuning the hyperparameters of the network such as learning rate and kernel size.

Before training the network, we prepare the training dataset, including training

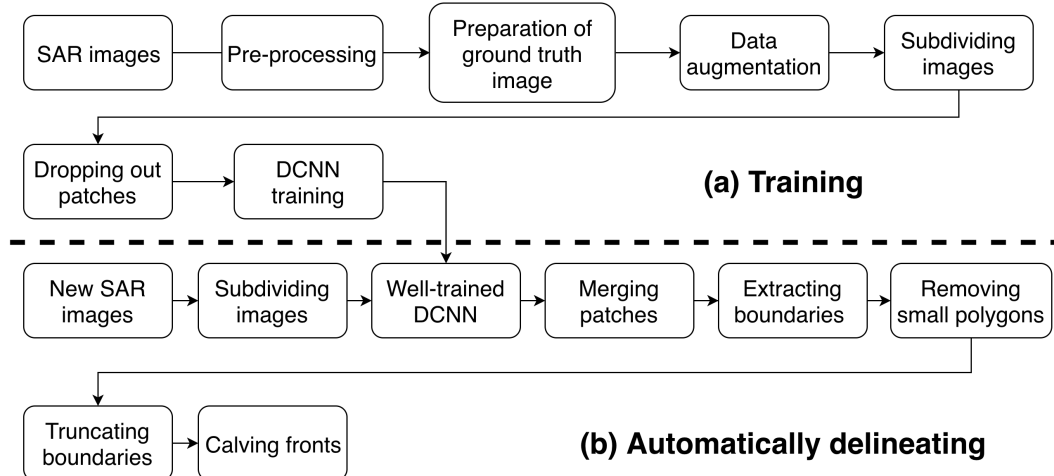


Figure 2.4: Diagram of the proposed framework. Details are described in Sections 2.3 and 2.4.

images (SAR images) and their corresponding ground truth images. The ground truth images have two classes: the ice mélange region is set as zero, and the non-ice-mélange region (including both glacier and bedrock regions) is set as one (Figure A.1). The ground truth images are derived by converting the vector of manually delineated calving fronts to rasters using GDAL. Manual delineation is simple on most TSX images. However, it is challenging to delineate the calving fronts on few TSX images acquired in winter and spring because the boundaries are obscured due to snow cover and sea ice bonding. For each of these obscure images, we use its temporally closest image with a clear calving front as a reference, and require that our manually-delineated fronts are smooth (Figure A.2). To ensure the effectiveness and accuracy of deep learning for a set of SAR images taken in all seasons spanning seven years, it is important to prepare a sufficiently

diverse training dataset. We include at least one image in each month into the training dataset to represent various conditions related to radar backscatter and image texture. First, radar backscatter can vary with the dielectric properties of the surface scatterers in the study area due to changes in snow cover, wetness, and variations in geometric properties such as roughness, grain size, and internal structure [Fahnestock et al., 1993]. Since our study area is in the ablation region, backscatter increases in winter because of dry snow cover and decreases in summer due to snow melting. Second, the seasonal and inter-annual variations of ice mélange condition can change the image texture. Sea ice formation in winter solidifies ice mélange, while ice mélange weakens in summer, resulting in freely floating icebergs [Amundson et al., 2010; Xie et al., 2016].

We also perform data augmentation to enrich our training dataset. We adopt the following two strategies. First, We vertically flip and rotate our training images by  $90^\circ$ ,  $180^\circ$ , and  $270^\circ$ , respectively, to constitute many possible locations of the calving front in the study area (Figure 2.2d). Second, We apply 2% linear stretch to the training images to enhance the edges. For all the values between the  $2^{nd}$  and  $98^{th}$  percentiles of the pixel value histogram, We linearly stretch them to the range between 0 to 255. The values lower than the  $2^{nd}$  percentile are set to zero, and the values larger than the  $98^{th}$  percentile are set to 255.

We subdivide each image ( $3565 \times 1634$  pixels) in the training dataset into small patches ( $960 \times 720$  pixels). Otherwise, the resolution would be limited by the GPU memory. We split images with overlaps, and obtain 36414 patches in total. Such a strategy allows a seamless segmentation after merging, which reduces the edge effect. A larger patch size can also better mitigate the edge effect. A common training strategy in deep learning is to train several training examples as a batch each time instead of training the whole dataset. With a given GPU memory, a smaller patch size allows more items in a batch, which increases the

efficiency and improves the accuracy of the gradient estimation at each step. To strike a balance between edge effect and batch size, we choose  $960 \times 720$  pixels as our patch size and the batch size is three.

Due to different computational time used in training and automatic delineation, the overlap areas between adjacent patches are set differently in the training and the test datasets. Taking the GPU we use as an example, training the network takes more time (80 hours) than automatic delineation (20 minutes) after the network is well trained. Therefore, we split the training images with smaller overlap (two-thirds of the patch size) to save computational power and split the test images with larger overlap (four-fifths of the patch size) to make denser samplings so that the results become more robust.

Balancing the number of training samples between classes is crucial in deep learning [Batista et al., 2005; Anantrasirichai et al., 2018]. Compared with patches with two classes, patches with only one class are not equally helpful for delineating boundaries. However, one-fifth of the 36414 patches only have one class. Therefore, we randomly drop out 80% of these patches to make the network perform better on the boundary between two classes and also to save computational power. Training the network starts with initializing all weights as zero. We stop the training when the validation error starts to increase for five consecutive epochs. After the training, we first subdivide each test TSX image into small patches and use the well-trained network to segment all the patches into ice mélange and non-ice-mélange classes. Then, we merge the segmented patches (binary images with a pixel value of one or zero) into a single segmentation image by averaging the overlaps. After merging, if the pixel value is larger than 0.5, we consider the pixel to be in a non-ice mélange region. We use GDAL to convert the segmentation image into a vector, which contains a large polygon constituted by both the calving front and the image border, and small isolated polygons caused

by erroneous segmentation. After removing the small polygons and truncating the large polygon to separate the calving front from the image border, we finally obtain the calving front for each image.

Using the post-processed delineation results, we can quantify the temporal calving front variations of both branches. Taking the earliest calving front (April 16<sup>th</sup>, 2009) as the reference, we calculate the enclosed area bounded by the reference and the calving front in a given TSX image. We adopt these metrics of area changes because they take both calving front position and shape into account.

## 2.5 Data validation and error estimation

Our results are validated by calving front products from the Greenland Ice Sheet Climate Change Initiative (CCI) project (<http://products.esa-icesheets-cci.org>). The CCI calving fronts are derived by manual delineation using ERS & Sentinel-1 SAR, and Landsat-5,7,8 optical imagery. We validate our results in the following two aspects.

First, the validation of the re-georeferencing (Section 3) is derived by directly comparing the manually delineated calving fronts obtained from this study and the CCI products. The calving fronts from these two datasets should be on the same date, and therefore, only six calving fronts are compared. We manually delineate the calving fronts from the TSX image after re-georeferencing and then calculate the averaged width of the enclosed area bounded by both the calving fronts from these two datasets. The mean difference is 104 meters (equivalent to  $\sim 17.3$  pixels) (Figure A.3). Several reasons could cause such a seemingly large difference. The geocoding information of the CCI products also has uncertainties. Moreover, manual delineation from both the CCI and ours are subjected to image quality and the different criteria we adopt for front delineation. To measure the

manual delineation error, we have another investigator to manually delineate the above-mentioned six calving fronts again. By comparing the two sets of independent delineation results, we obtained a mean difference of 33 meters (equivalent to  $\sim 5.5$  pixels).

Second, the difference of calving front variations between ours and the CCI presents an overall validation that sums up both re-georeferencing and network-delineation uncertainties. We quantify the calving front variations of the CCI products with the same method and reference used in our results. Finally, we calculate the difference between these two variations in terms of both area and equivalent length.

The errors in the test dataset represent the error of the network. Unlike the BCE-measured segmentation error in training, the test error is for calving front delineation. We measure the test error by calculating the averaged width of the enclosed area bounded by the manually delineated and the network-delineated calving fronts (Figure A.4).

## 2.6 Results

We present our results in the following order: (1) the network-delineated calving fronts from April 16th, 2009 to December 23rd, 2015, which are shown in a movie (Movie A1); (2) two examples of our automatically delineated calving fronts (i.e., results in test dataset) (Figure 2.5); (3) retreat rates (Table 2.1) and time series of calving front variations (Figure 2.6); (4) inter-annual calving front variation (Figure 2.7 and 2.8).

The individual network-delineated results are influenced by image quality. Usually, the boundary is more distinct in summer than in other seasons, yielding superior results (Figure 2.5a). In winter and spring, the boundary is obscure due

to the low contrast and similar texture of the images, for example, the Branch B and the northern part of Branch A (Figure 2.5b, 2.5c, and 2.5d). The backscatters of the snow-covered ice mélange and the glacier are similar. Moreover, sea ice formation in winter solidifies the ice mélange and even bonds it with the glacier. As a result, our detected edge deviates from the ground truth. Table A.1 lists all of the test error with a mean of 38 meters. It also shows that our network performs better in summer than other seasons.

Overall, our results agree well with the CCI products (Figure 2.6). The

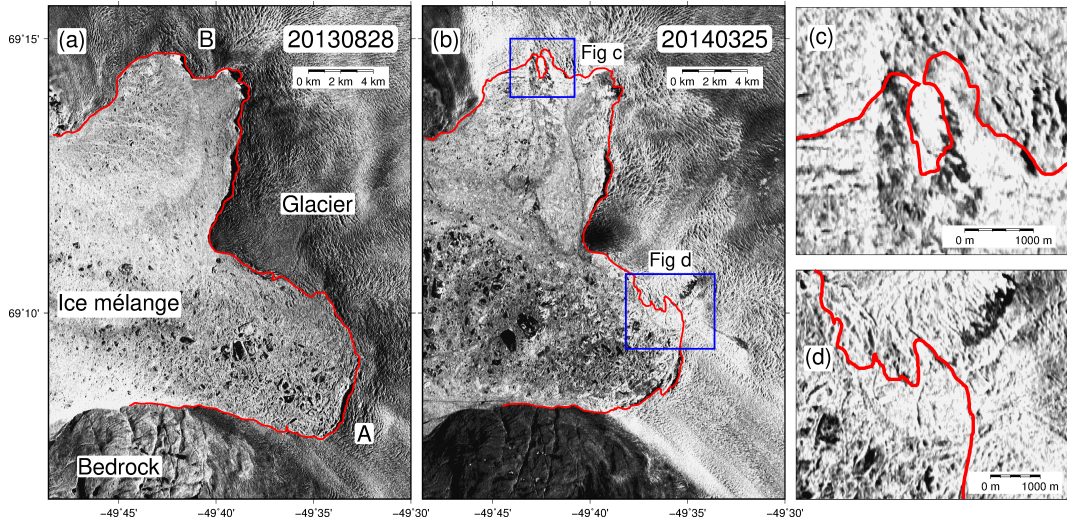


Figure 2.5: Examples of (a) superior and (b) inferior delineation from our deep-learning-based method. In both (a) and (b), the red line shows the calving front delineated by the network. (c) and (d) show the zoom-in figure of the obscure calving front positions within the blue boxes in (b).

area difference is  $2.14 \times 106 \text{ m}^2$ , and the equivalent length difference is 73 meters. Moreover, our results have a higher temporal resolution (about two measurements every month) than the CCI products (about four measurements every year). Therefore, we can observe the seasonal and inter-annual variations more clearly. Based on our results, Branches A and B retreated from 2009 to 2015 with linear trends of  $-117 \pm 1 \text{ m yr}^{-1}$  and  $-157 \pm 1 \text{ m yr}^{-1}$ , respectively. The

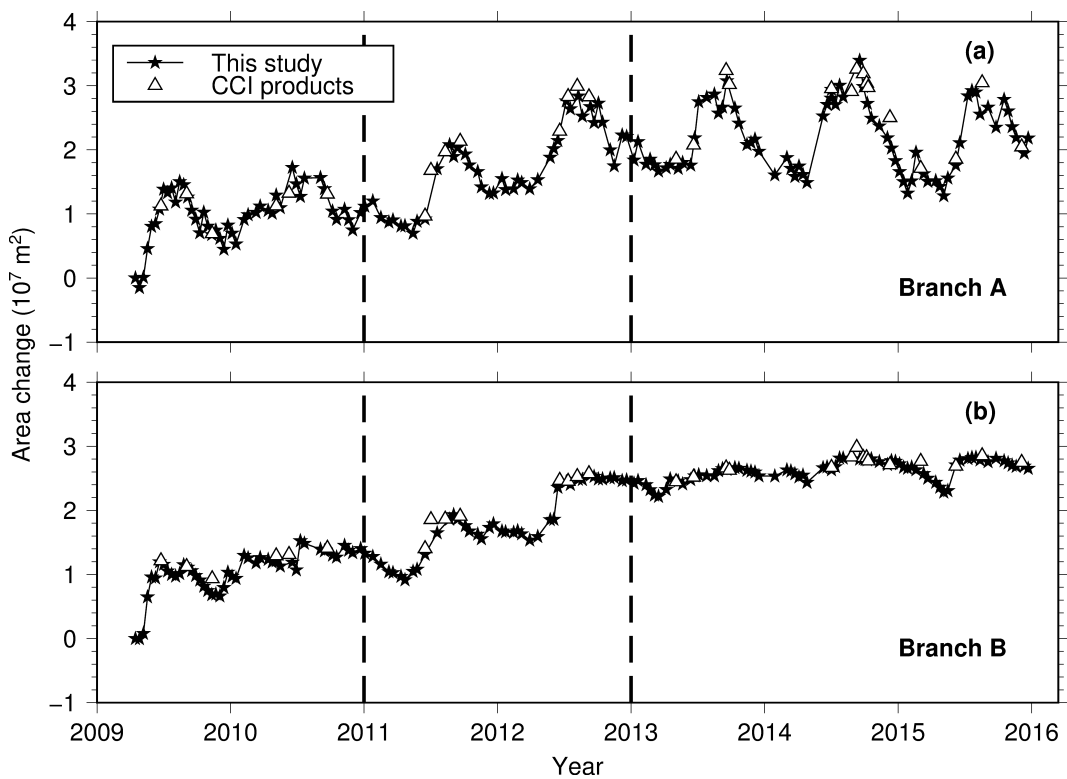


Figure 2.6: Time series of calving front variations (in area changes) of Branches A and B from our deep learning method (stars) and the Greenland Ice Sheet CCI project (triangles). Dashed vertical lines divide the time series into three separate phases (see text).

inter-annual variation can be roughly divided into three phases (Figure 2.6 and summarized in Table 2.1). (1) From April 2009 to January 2011, the retreat rates were  $-141 \text{ m } y^{-1}$  and  $-228 \text{ m } y^{-1}$  along Branches A and B, respectively. (2) From January 2011 to January 2013, the glacier retreated 170% and 61% faster than in the previous phase in Branches A and B, respectively. (3) From January 2013 to December 2015, these two branches behaved differently. In Branch A, the glacier retreated and advanced seasonally, but at much slower average rates ( $-23 \text{ m } y^{-1}$ ). In Branch B, the seasonal variations were minor, and the glacier retreated slowly ( $-46 \text{ m } y^{-1}$ ).

Further examination of the inter-annual variation indicates that the calving front

Table 2.1: Retreat rates in area and equivalent length during different phases.

	Period	Mean retreat rate	
		Branch A	Branch B
Area Change ( $10^6 \text{ m}^2 \text{ yr}^{-1}$ )	Apr 2009–Jan 2011	$-3.07 \pm 0.05$	$-4.97 \pm 0.09$
	Jan 2011–Jan 2013	$-8.30 \pm 0.04$	$-8.03 \pm 0.07$
	Jan 2013–Dec 2015	$-0.50 \pm 0.03$	$-1.01 \pm 0.03$
	Apr 2009–Dec 2015	$-2.56 \pm 0.01$	$-3.41 \pm 0.01$
Equivalent length change( $\text{m yr}^{-1}$ )	Apr 2009–Jan 2011	$-141 \pm 4$	$-228 \pm 9$
	Jan 2011–Jan 2013	$-381 \pm 3$	$-368 \pm 5$
	Jan 2013–Dec 2015	$-23 \pm 2$	$-46 \pm 2$
	Apr 2009–Dec 2015	$-117 \pm 1$	$-157 \pm 1$

exhibited different seasonal variations from year to year. First, even within a close distance of ten kilometers around the coastal area, Branches A and B behaved asynchronously. For example, in 2010, Branch A began to retreat in May, while Branch B started to retreat one month later (Figure 2.7a and 2.8). Moreover, after 2012, Branch A’s front underwent strong seasonal variation while Branch B’s front remained relatively stable (Figure 2.7b). Second, the retreat timing of the glacier varied in different years. In Branch A, the front began to retreat around May in most years, while in 2011 and 2013 the retreat started in June. In 2010, both branches experienced a sudden retreat from mid-January to early February, and then became stable. Third, the calving front variation became regular after 2012. In Branch A, the front stopped retreating in July of each year, and its position remained unchanged up to September to October. In Branch B, the front advanced in spring and retreated in early summer, while its position remained almost unchanged in other seasons (Figure 2.6 and 2.8).

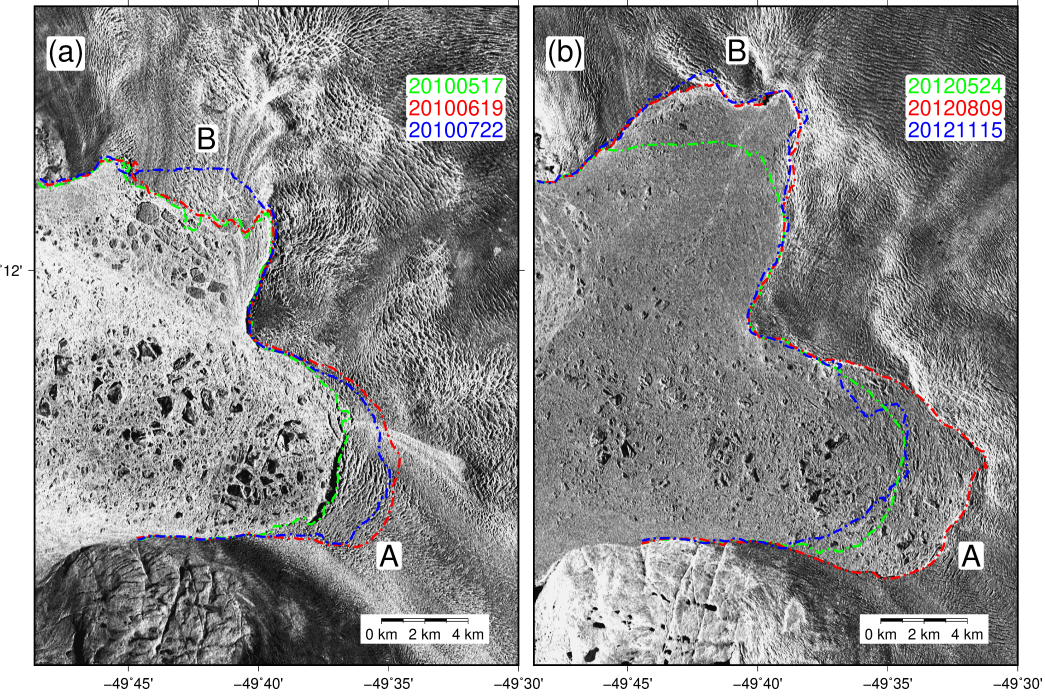


Figure 2.7: Two examples showing the asynchronous behaviors of Branches A and B. (a) Branch A began to retreat in May 2010, while Branch B started to retreat one month later. (b) Branch A’s calving front underwent strong variation between August to November 2012, whereas Branch B’s calving front was relatively stable. The magenta line in both (a) and (b) shows the calving front position just before the annual retreat.

## 2.7 Discussion

### 2.7.1 Differences from the previous work

We discuss the differences from the previous work in two aspects: (1) deep-learning-based front delineation and (2) estimation of front variations.

[Mohajerani et al., 2019] have applied U-Net architecture to Landsat images over Jakobshavn, Sverdrup, Kangerlussuaq, and Helheim glaciers in Greenland. Despite both using the U-Net architecture, our study is different from [Mohajerani et al., 2019] in datasets, result accuracy, transferability, strategies for classifica-

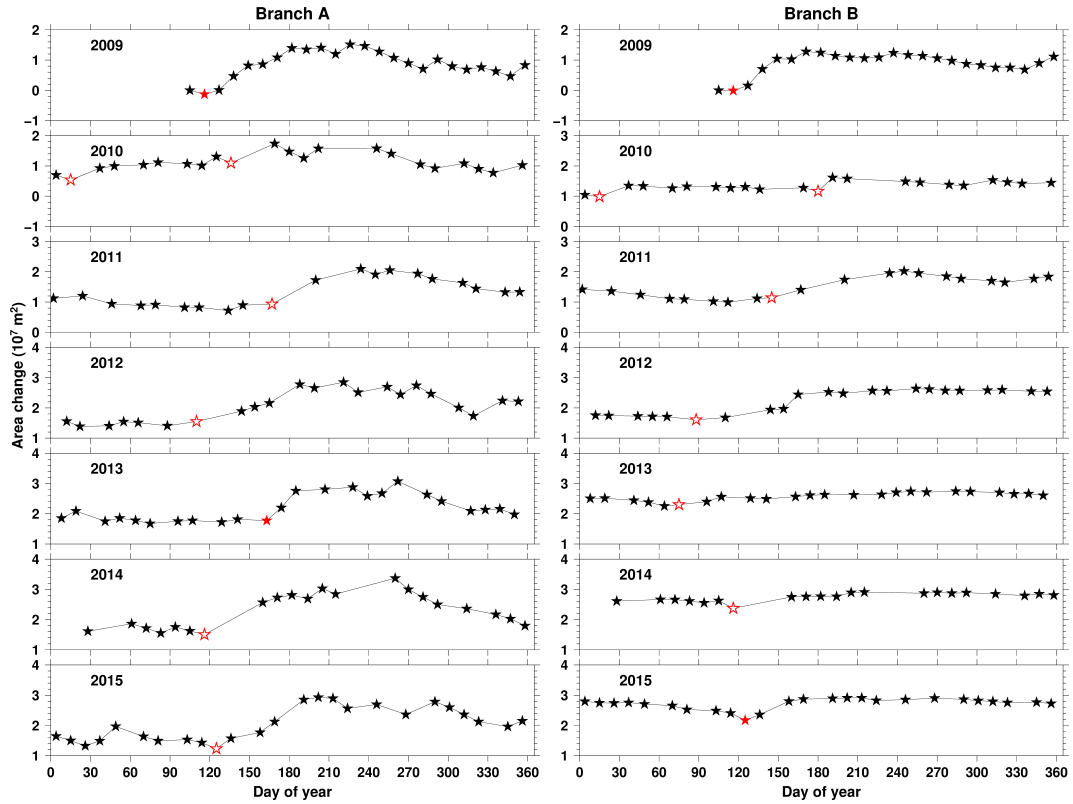


Figure 2.8: Two examples showing the asynchronous behaviors of Branches A and B. (a) Branch A began to retreat in May 2010, while Branch B started to retreat one month later. (b) Branch A’s calving front underwent strong variation between August to November 2012, whereas Branch B’s calving front was relatively stable. The magenta line in both (a) and (b) shows the calving front position just before the annual retreat.

tion, post-processing, and image resampling. The usage of high-resolution TSX images allows us to generate more accurate calving fronts. Without additional manual practices, our method is more transferable, particularly when applying to large areas with many glaciers. Below we discuss the technical differences in detail.

First, our study classifies the surface into two types (i.e., ice mélange and non-ice mélange) to extract the calving front, while [Mohajerani et al., 2019] used semantic segmentation to extract the front without classifying the surrounding

surfaces. Both strategies require post-processing procedures. In our method, erroneous segmentation can cause small isolated polygons within the ice mélange or the non-ice mélange regions. Yet, we can solve this problem by removing these small polygons in the post-processing. The semantic segmentation used by [Mohajerani et al., 2019] can be affected by icebergs, crevasses, etc. Nonetheless, the least-cost path search method could solve this problem [Mohajerani et al., 2019]. Second, additional manual practices are needed in the work of [Mohajerani et al., 2019]. For instance, images of every single glacier in their work were adjusted by a certain angle to make all the glaciers flow in the same direction in the pre-processing. Third, we subdivide the images into small patches, which allows us to utilize the advantages of images with high resolution and various sizes. [Mohajerani et al., 2019] resampled images to a fixed size (240 by 152 pixels) with low spatial resolution (49.0 to 88.1 meters), therefore the position accuracy is limited. Previous studies have quantified front variations using only the central line positions [Walsh et al., 2012; Joughin et al., 2014]. In this study, we calculate the enclosed area bounded by different front positions. Comparing with using only the central line position, these metrics of area changes are more unbiased since the front position changes are often uneven, with some parts of the front retreating while other parts remain stable. Moreover, capturing these uneven changes can help to understand the controlling mechanisms of front variations, especially for modelers to simulate the changes of the entire front. Firstly, lateral friction induced by the fjord walls could prevent the glacier from calving. Secondly, the bed elevation at the central line is often lower than near the fjord walls, which makes the glacier easier to calve in the middle. Thirdly, the ocean-ice interaction is stronger in the middle of the front than near the fjord walls, where the ocean tide is less obstructed by the fjord walls. All these three mechanisms make glacier calve more in the middle than near the fjord walls.

### 2.7.2 Calving front variation and bed elevation

In general, calving front variations are influenced by multiple factors, including floating or grounding conditions [McFadden et al., 2011; Murray et al., 2015; Bondzio, 2017; Fried et al., 2018], interaction with the ocean [Holland et al., 2008; Howat et al., 2008; Motyka et al., 2011; Vieli and Nick, 2011; Straneo et al., 2013], ice mélange and sea ice conditions [Amundson et al., 2010; Moon et al., 2015; Cassotto et al., 2015], basal lubrication [Joughin et al., 2008a; Moon et al., 2014] and bed elevation [Joughin et al., 2008b, 2014; Kehrl et al., 2017; Bunce et al., 2018]. Here we examine the possible link between the observed variations of the calving fronts with bed elevation.

Bed elevation has a substantial influence on the glacier retreat. In the first situation where the bed is flat, glacier retreat decreases resisting force, which accelerates the glacier. The acceleration of the glacier can also thin the ice. Thinning reduces the effective pressure at the bed,  $N = P_i - P_w$ , where  $P_i$  is the overburden pressure and  $P_w$  is water pressure. A decreased  $N$  reduces basal drag, causing stretching and faster flow and constituting positive feedback. In the second situation, as the glacier retreats into an overdeepened basin where the bed slopes down inland or is retrograde, the positive feedback is reinforced, and the glacier becomes more unstable, for two reasons. First, ice thickness at the calving front increases as the retreat progresses, increasing driving stress. Second, because the calving front moves into deeper water, this retreat decreases  $N$  further. In the third situation where the bed slopes inland-uphill, the glacier may stabilize, since retreating into shallower water increases  $N$  and decreases driving stress.

Previous studies also suggest that bed elevation has a substantial influence on glacier calving front variations. Examining the height above flotation of Branch A in Jakobshavn, [Joughin et al., 2014] suggested that retreating into an overdeep-

ened basin where the bed slope is retrograde may lead to an unstable calving front retreat, and a bed sloping inland-uphill may stabilize the glacier. Other studies have also suggested that retreating into deeper water may accelerate the glacier, resulting in an unstable retreating [Howat et al., 2005, 2007; Nick et al., 2009; Catania et al., 2018].

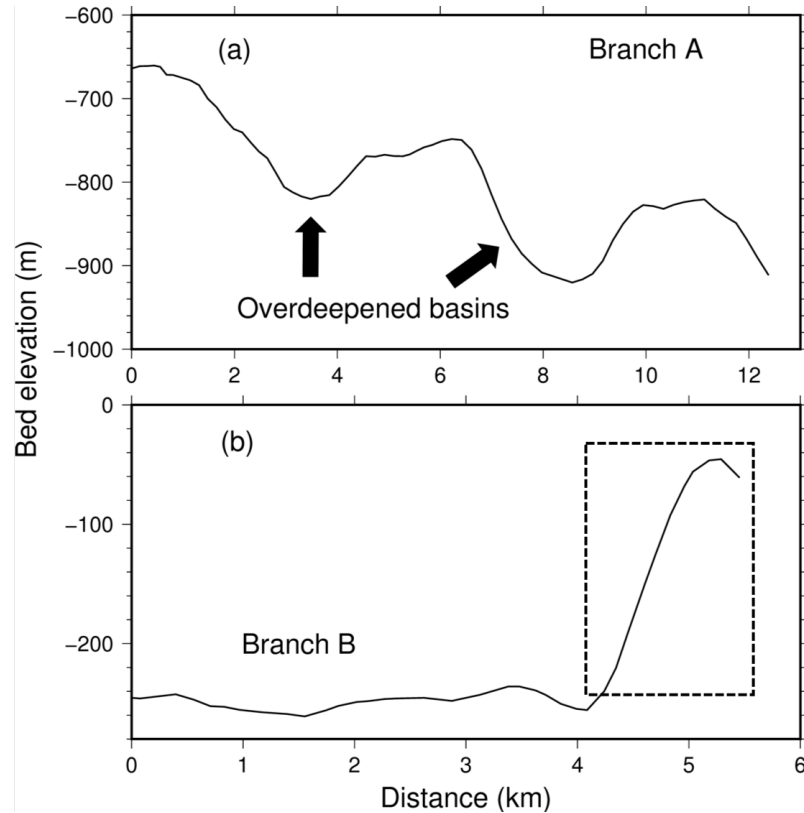


Figure 2.9: Bed elevation profiles of two branches derived from BedMachine v3 [Morlighem et al., 2017]. The profile locations are shown in Figure 2.1a. The dashed box shows the zone where the bed slopes uphill inland.

In our study area, the bed elevation derived from BedMachine v3 [Morlighem et al., 2017] shows two overdeepened basins along the main channel of Branch A (Figure 2.9a). During the period from 2009 to 2015, the calving front of Branch A retreated into the second overdeepened basin in August 2011 for the first time, which may have produced a faster rate of retreat. In July 2012, the glacier

retreated to the bottom of the overdeepened basin and stopped retreating further (Movie A2). The inland-uphill bed slope behind the bottom of the overdeepened basin may have prevented the glacier from further retreating. In Branch B, after June 2012, the glacier retreated into a zone where the bed slopes uphill inland (Figure 2.9b, Movie A3), which may have led to the more regular and stable behavior of Branch B after June 2012 (Figure 2.6b).

### 2.7.3 Limitations of current method

The current method is limited by high computational power requirement, and manual delineation largely control its accuracy. First, the U-Net architecture requires relatively high GPU memory for large images. In our configuration, around 15 gigabyte (GB) GPU memory is needed for training the network. Second, although splitting images with overlaps allow as to apply the network to images with different sizes, the overlaps increase the training time. These two limitations can be overcome by hardware development. With more powerful GPU in the future, we can increase the calculation efficiency and lessen the training time. Third, the accuracy of this method relies on manual delineation as well as the information richness of the training dataset [Goodfellow et al., 2016]. If the training examples are not representative for the actual task or if the manual delineation in these examples is of low quality or inconsistent, U-Net will either fail to train or will reproduce inconsistent results on new data. To further increase the accuracy and robustness of the network, more training examples are needed.

### 2.7.4 Prospects for future work

In the near future, we will include more training examples to minimize network error. In this study, the well-trained network is limited to a specific dataset,

namely TSX images. However, it is feasible to apply the DCNN to multi-sensor remote sensing imagery, which has been proved by previous studies [Nogueira et al., 2017; Gao et al., 2018]. Moreover, as long as the calving fronts are clear in the images, our method can also use images with light cloud cover and Landsat 7 images with scan line errors.

The effectiveness and transferable nature of deep learning [LeCun et al., 2015] promises that our methodology can be applied to many other glaciers, both in Greenland and elsewhere in the world. Besides Jakobshavn Isbræ, other Greenland tidewater glaciers such as Helheim and Kangerdlugssuaq also show strong calving front variations [Howat et al., 2005, 2007; Joughin et al., 2008b]. In theory, the DCNN can be retrained whenever new data is added to the training dataset. Moreover, including more data over other places can increase the generalization of the network, making it applicable to more situations [Goodfellow et al., 2016].

## 2.8 Conclusion

This Chapter designs a deep-learning-based method automate the calving front delineation of Jakobshavn Isbræ from TerraSAR-X SAR images obtained from 2009 to 2015. Small test error suggests that the accuracy of a well-trained network can be close to the human level. Our results reveal that the two branches of Jakobshavn Isbræ behaved asynchronously. We suggest that bed elevation may have a major influence on the observed calving front variations. Our methodology can be applied to many other tidewater glaciers both in Greenland and elsewhere in the world using multi-temporal and multi-sensor remote sensing imagery.

---

□ End of chapter.

## **Chapter 3**

# **An automated, generalized, deep-learning-based method for delineating the calving fronts of Greenland glaciers from multi-sensor remote sensing imagery**

This chapter further increases the generalization and robustness of the deep learning-based method. The method in Chapter 2 is restricted to a specific study area and dataset. In this study, we develop a more generalized method that can be applied to a major outlet glacier or remote sensing datasets that are not included in the training. We integrate seven remote sensing datasets into a single deep learning network. The core datasets include optical (Landsat-8 and Sentinel-2) and synthetic aperture radar images (Envisat, ALOS-1 TerraSAR-X, Sentinel-1, and ALOS-2) taken over Jakobshavn Isbræ, Kangerlussuaq, and Helheim, spanning from 2002 to 2019. We evaluate four neural network architectures (e.g., U-Net, DeepLabv3+ with Resnet, DRN, and MobileNet as the backbones) and three histogram modification strategies (e.g., histogram normalization, linear stretching, and no histogram modification). We find that the combination of

histogram normalization and DRN-DeepLabv3+ has the lowest test error, at 86 meters. These promising results show that our method has a high generalization ability and considerable potential for delineating calving fronts at many other glaciers in Greenland and elsewhere in the world.

## 3.1 Introduction

In this study, we aim to further increase the generalization and robustness of the deep-learning-based method. First, we apply DeepLabv3+, a more advanced deep-learning architecture than U-Net. DeepLabv3+ can tackle the diversity introduced by the different spatial resolutions of multi-sensor remote sensing imagery. Second, we adopt histogram normalization to homogenize diverse image properties. We conduct 12 experiments to find the best combination of deep learning networks and histogram modification methods. We quantify calving front variations and investigate the seasonal and inter-annual signals at each glacier. We also discuss the advantages and limitations of this method. Our key innovations are the integration of seven remote sensing datasets into a single deep learning network, and its application to remote sensing datasets that are not included in the training. Furthermore, integrating multiple datasets offers us sub-weekly calving front datasets.

### 3.1.1 Study areas

We choose the three largest outlet glaciers in Greenland as our study targets, namely Jakobshavn Isbræ, Kangerlussuaq, and Helheim (Figure 3.1). In recent years, they have exhibited dramatic retreats, which could increase our dataset’s diversity and, therefore, enhance its robustness. More specifically, we choose Jakobshavn Isbræ and Kangerlussuaq as the training glaciers, and use Helheim

to test the generalization level of our deep-learning-based method.

### 3.1.1.1 Jakobshavn Isbræ

The dramatic retreat of Jakobshavn Isbræ and the influence of ice mélange are introduced in Section 2.2. In addition to ice mélange, Jakobshavn Isbræ’s front position is also controlled by other factors, including submarine melting, bed topography, and ocean temperature. Around 1998, with warm ocean water entering and increased submarine melting, the ice tongue was destabilized, followed by an abrupt retreat [Motyka et al., 2011]. In 2003, Jakobshavn Isbræ’s front started to fluctuate seasonally [Joughin et al., 2008c, 2014], probably driven by ice mélange strength [Amundson et al., 2010]. In 2009, the glacier started to retreat rapidly as its terminus reached an overdeepened basin [Joughin et al., 2014]. In 2017, this retreating has halted in response to recent regional ocean cooling [Khazendar et al., 2019].

### 3.1.1.2 Kangerlussuaq and Helheim

The Kangerlussuaq and Helheim glaciers in southeast Greenland collectively drain 8% of the Greenland Ice Sheet area [Nick et al., 2013]. Here, we group these two glaciers together, since they have exhibited synchronous dynamic behaviors caused by regional environmental forcing and asynchronous behaviors driven by different glaciological settings such as floating conditions, ice mélange strength, and fjord geometry. A comparison between the two glaciers helps to elucidate their dynamic behaviors.

In the late 1990s, the fronts of both glaciers appeared to advance and retreat in tandem, possibly driven by regional environmental forcing [Luckman et al., 2006]. In the early 2000s, both glaciers abruptly retreated, thinned, and accelerated [Rignot et al., 2004; Stearns and Hamilton, 2007]. Between 2002 and 2005,

Helheim retreated more than 7 km [Howat et al., 2005], while Kangerlussuaq underwent a 5-km retreat in 2004 and 2005 [Luckman et al., 2006]. Retreating into deeper water promoted the abrupt retreat of both glaciers between 2002 and 2005 [Howat et al., 2007; Joughin et al., 2008b].

Helheim and Kangerlussuaq also showed asynchronous variations. In the early 2000s, they behaved differently on seasonal scales. The calving front varied seasonally at Kangerlussuaq but showed little seasonality at Helheim [Joughin et al., 2008b; Schild and Hamilton, 2013]. They were also different in their iceberg-calving behaviors. Two types of icebergs have been observed at Helheim and Kangerlussuaq: tabular and nontabular [Joughin et al., 2008b]. The glaciers with a floating tongue can generate tabular icebergs, while grounded glaciers generate small, nontabular icebergs. From 2008 to 2016, the percentage of tabular iceberg calving among all calving episodes was higher at Kangerlussuaq (53%) than at Helheim (14%), possibly due to different floating conditions [Kehrl et al., 2017]. Similarities in glaciological settings among these glaciers could help the network learn their common features, while differences could increase our dataset's diversity. First, all three glaciers have ice mélange ahead of their front. The common features of ice mélange learned from different glaciers could help the network have better accuracy on the blur boundaries caused by the bounding of the ice mélange to the glacier. Second, Jakobshavn Isbræ has two branches, while Helheim and Kangerlussuaq have one channel. Third, Helheim and Kangerlussuaq, unlike Jakobshavn Isbræ, have floating tongues, which can generate tabular icebergs. Moreover, Helheim and Kangerlussuaq could have large crevasses near the terminus. The diversity enhanced by these differences could make the network more robust and applicable to broader areas.

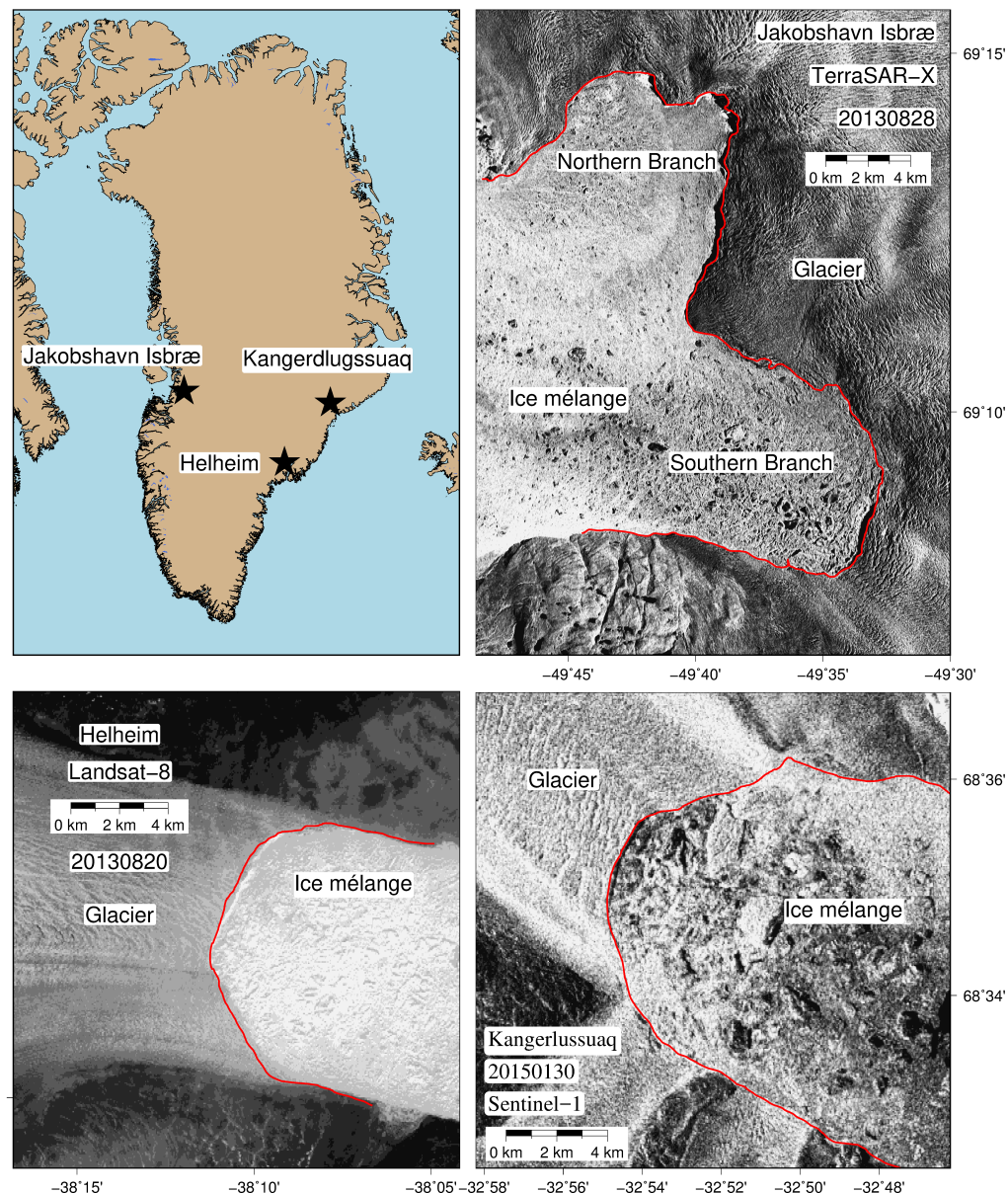


Figure 3.1: Location of the glaciers included in this research. Red lines show the network-delineated calving fronts.

### 3.1.2 Remote sensing dataset

We use seven datasets, two optical (i.e., Landsat-8, Sentinel-2) and five SAR (i.e., Envisat, ALOS-1, TSX, Sentinel-1, and ALOS-2), covering the years from 2002

to 2019. These datasets are referred to by their mission names in this paper. Optical and SAR images can complement each other (Table 3.1). Optical images are limited by cloudiness and the lack of sunlight in polar winter. Due to their insensitivity to weather, SAR images have become an important complementary dataset. However, SAR images are affected by speckle noise and geometrical distortions such as layover. The correction of layover yields accurate geolocations, but it might generate artifacts. Optical images can complement SAR images since the former are free from speckle noise and less affected by geometrical distortions. Integrating seven datasets largely increases the number of images (Table 3.2), and therefore increases the temporal resolution of the glacier front dataset. Moreover, it enlarges the duration of the front dataset. Among the datasets we select, no single dataset can cover from 2002 to 2019 (Table. 3.2).

Table 3.1: Advantages and disadvantages of SAR and optical images.

	SAR	Optical
Advantages	Insensitivity to weather	No speckle noise and distortions
Disadvantages	Speckle noise; artifacts	Limited by weather and solar illumination

We set two criteria for choosing these datasets: accessibility and spatial resolution. Access to TSX data older than 18 months and ALOS images requires data proposals, but the other four datasets are completely open-access. The lowest spatial resolution among all chosen datasets is 40 meters (Table 3.2). These high-spatial-resolution images enable us to accurately digitize glacier fronts (referred to as ground truth). Moreover, except for TSX, all the other six datasets are chosen in pairs according to their data types. We select either one of the two for training and the other for testing the generalization of our method on different data types. For instance, both Envisat and Sentinel-1 images are C-band SAR;

but the Sentinel-1 data are only used for training, whereas the Envisat data are used for testing the generalization of C-band SAR images.

We note that the numbers of images are imbalanced due to their accessibility and repeat cycle (Table 3.2). For instance, the number of ALOS images is limited due to its small quota. Sentinel-1 has the largest number of images, owing to its low repeat cycle (6 days) and long duration (6 years), and we use Sentinel-1 images at all three glaciers. Although Sentinel-2 has the highest temporal resolution, its number of images is not the largest due to the relatively short duration (4 years), and we only use Sentinel-2 images over Helheim.

For Landsat-8, we use the panchromatic band for its finest 15-meter resolution. The Sentinel-2A & -2B revisit every ten days, which collectively gives a five-day repeat cycle. For Envisat, we use Advanced Synthetic Aperture Radar (ASAR) images. ALOS-1 & -2 were launched in 2006 and 2014, respectively, and ALOS-1 ended in 2011. We choose the Phased Array type L-band Synthetic Aperture Radar (PALSAR) products in stripemap imaging mode. For TSX, we use the enhanced-ellipsoid-corrected (EEC) products in stripemap imaging mode. For Sentinel-1A & -1B, we choose the Ground Range Detected (GRD) products in Interferometric Wide (IW) image mode.

Landsat-8, Sentinel-1, Sentinel-2 images are cropped and downloaded through Google Earth Engine (<https://earthengine.google.com/>) [Gorelick et al., 2017]. We obtain Envisat images from European Space Agency (<https://esar-ds.eo.esa.int/oads/access/>), TSX images from Deutsches Zentrum für Luft- und Raumfahrt (DLR) (<https://eoweb.dlr.de/egp/>), and ALOS-1 & -2 images from Japan Aerospace Exploration Agency (<https://auig2.jaxa.jp/>).

Table 3.2: Summary of datasets used in this study. This table shows the satellite mission, band (SAR data only), nominal spatial resolution, total number of images, duration, nominal repeat cycle of each dataset.

	Satellite mission	Band	Resolution (m)	Number of images	Duration	Repeat cycle (days)
Optical	Landsat-8	Panchromatic	15	468	2013–2018	16
	Sentinel-2	Red band	10	87	2016–2019	10 (5)
	Envisat	C band	30	56	2002–2009	35
	ALOS-1	L band	10	13	2006–2010	46
SAR	TerraSAR-X	X band	3	169	2009–2015	11
	Sentinel-1	C band	40	1280	2014–2019	12 (6)
	ALOS-2	L band	10	14	2014–2019	46

## 3.2 Method

Previous deep-learning-based, automated delineation methods applied U-Net to a specific dataset and demonstrated its feasibility [Mohajerani et al., 2019; Baumhoer et al., 2019]. However, the usage of fixed-size kernels in U-Net might make results less promising when applying the network to multi-sensor remote sensing datasets with various spatial resolutions. Here, we adopt an alternative CNN, DeepLabv3+.

### 3.2.1 An alternative CNN: DeepLabv3+

DeepLabv3+ is a state-of-the-art deep learning algorithm for image segmentation [Chen et al., 2018]. It combines the usage of the encoder-decoder structure and atrous convolution, where the former can obtain sharp object boundaries while the latter senses multi-scale contextual information. These two abilities are helpful for our task since 1) sharp boundaries could improve delineation accuracy, and 2) we integrate remote sensing datasets with different spatial resolutions. Next, we will introduce the key concepts adopted in DeepLabv3+ (e.g., atrous convolution

and encoder-decoder structure) and describe the architecture of DeepLabv3+.

Atrous (or dilated) convolution is the convolution with holes inserted in the filter (the French word *trou* means ‘hole’ in English). Considering a two-dimensional output  $y$ , at each location  $[i, j]$ , the atrous convolution kernel  $w$  is applied over the input feature map  $x$ :

$$y[i, j] = \sum_m \sum_n x[i + r \times m, j + r \times n] \times w[m, n] \quad (3.1)$$

where  $r$  is the rate of atrous convolution, and standard convolution is a special case for  $r = 1$ . Atrous convolution allows us to increase filter’s field-of-view (FOV) by effectively enlarging the kernel size of a  $k \times k$  filter to  $k_e = k + (k - 1) \times (r - 1)$  without increasing the number of the kernel’s parameters. Moreover, atrous convolution with different rate values has various FOVs and is therefore able to sense multi-scale contextual information. Like U-Net, DeepLabv3+ adopts the encoder-decoder structure. It contains an encoder that captures features from low-level (e.g., corners and lines) to high-level (e.g., glacial texture), and a decoder that gradually recovers the spatial information. Based on the above-mentioned idea, DeepLabv3+ has an encoder that applies atrous convolution to sense multi-scale contextual information and a simple but effective decoder module to obtain sharp object boundaries.

The encoder of DeepLabv3+ starts with the network backbone (Figure 3.3), which applies atrous convolution to previously developed architectures. DeepLabv3+ then applies four parallel atrous convolutions with different rates to the output of the network backbone (known as Atrous Spatial Pyramid Pooling, or ASPP). To incorporate global context information into the model, DeepLabv3+ also applies average pooling to the backbone’s output. After concatenating all the resulting features from both atrous convolution and pooling, a  $1 \times 1$  convolution is applied

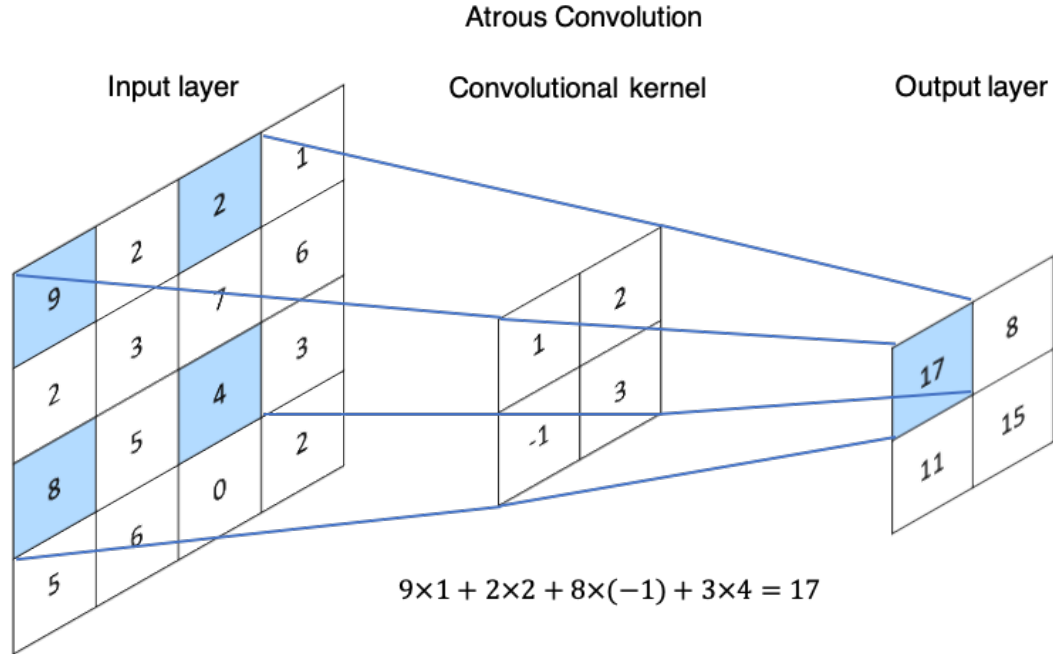


Figure 3.2: Illustration of a simple atrous convolution with the kernel size of 2, and the rate of atrous convolution is 2. Equation below shows the calculation of atrous convolution for the upper-left unit of the output layer.

to reduce the number of channels and produce encoder features.

The encoder features are first upsampled and then concatenated with the corresponding low-level features from the network backbone which have the same spatial resolution. Another  $1 \times 1$  convolution is applied to the low-level feature to have the same number of channels with the encoder features. After concatenation, a few  $3 \times 3$  convolutions are applied, followed by another upsampling that gives the network's output the same spatial resolution as the input.

Since the network backbone of DeepLabv3+ is based on previously developed architectures, it can share their particularities. In this study, we adopt three widely used networks as backbones: ResNet [He et al., 2016], DRN [Yu et al., 2017], and MobileNet [Howard et al., 2017]. ResNet can avoid a typical problem in deep learning, namely that as the network depth increases, the accuracy becomes sat-

urated and then degrades [He et al., 2016]. ResNet is, therefore, relatively easy to optimize and can gain accuracy from increasing depth. DRN is the dilated version of Resnet and requires a larger GPU memory [Yu et al., 2017]. By downsampling inputs with smaller factors in the network, DRN can recognize more detailed features and improve the accuracy of results [Yu et al., 2017]. MobileNet is designed as a small and efficient network. By shrinking the number of adjustable parameters and decreasing image resolution, MobileNet sacrifices a modest amount of accuracy in the interests of reducing the required computational power [Howard et al., 2017]. Even though the accuracy and efficiency of these architectures have been well tested and appraised for processing images from everyday scenes (e.g., identifying and outlining cats and dogs), their performances for our specific task (i.e., delineating glacial fronts from satellite imagery) remain to be evaluated.

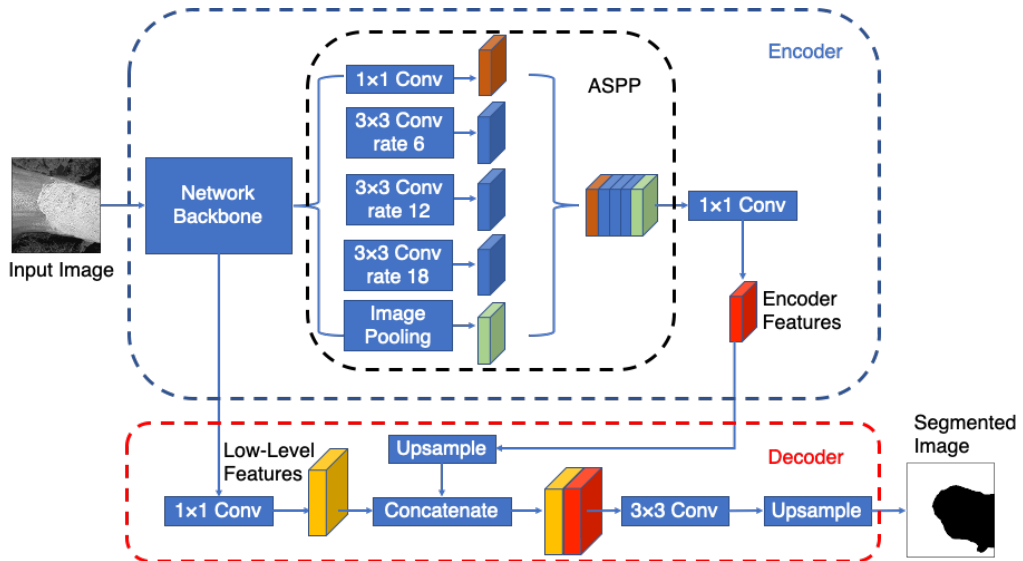


Figure 3.3: Architecture of DeepLabv3+ (adapted from [Chen et al., 2018]). The network is constructed by an encoder (blue) and a decoder (red). The encoder is composed of the network backbone, the ASPP module (black), and the following  $1 \times 1$  convolution. The decoder combines the low-level feature from the network backbone and the encoder output.

### 3.2.2 Improvements of deep-learning-based framework

A simplified framework for using deep learning to delineate the calving front is illustrated in Figure 3.4. Full details of the processing steps are described in Chapter 2. Below we will highlight the new strategies implanted in this study that aim to generalize our method and release labor to evaluate the quality of results.

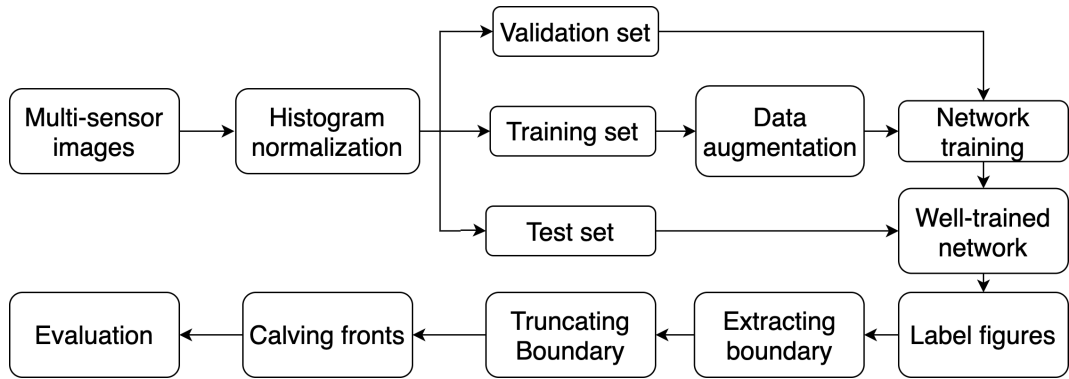


Figure 3.4: Diagram of the deep-learning-based framework (modified from figure 2.4).

#### 3.2.2.1 Pre-processing procedures

We adopt similar pre-processing procedures in Chapter 2, including 1) cropping to the area of interest, 2) image augmentation, and 3) despeckling for SAR images. A further pre-processing procedure, 4) histogram normalization, is added due to the diversity introduced by combining multiple datasets. The images in this study are taken by seven sensors, including both optical and SAR. They have different ranges of digital values, image texture, and are of various bands (Table 3.2 and Figure 3.5). It is therefore difficult for the network to retrieve shared information among the different datasets. To homogenize all the images, we normalize each image histogram to the same Gaussian distribution with the same pixel value range (see Figure 3.5, for example). This normalization enhances the image

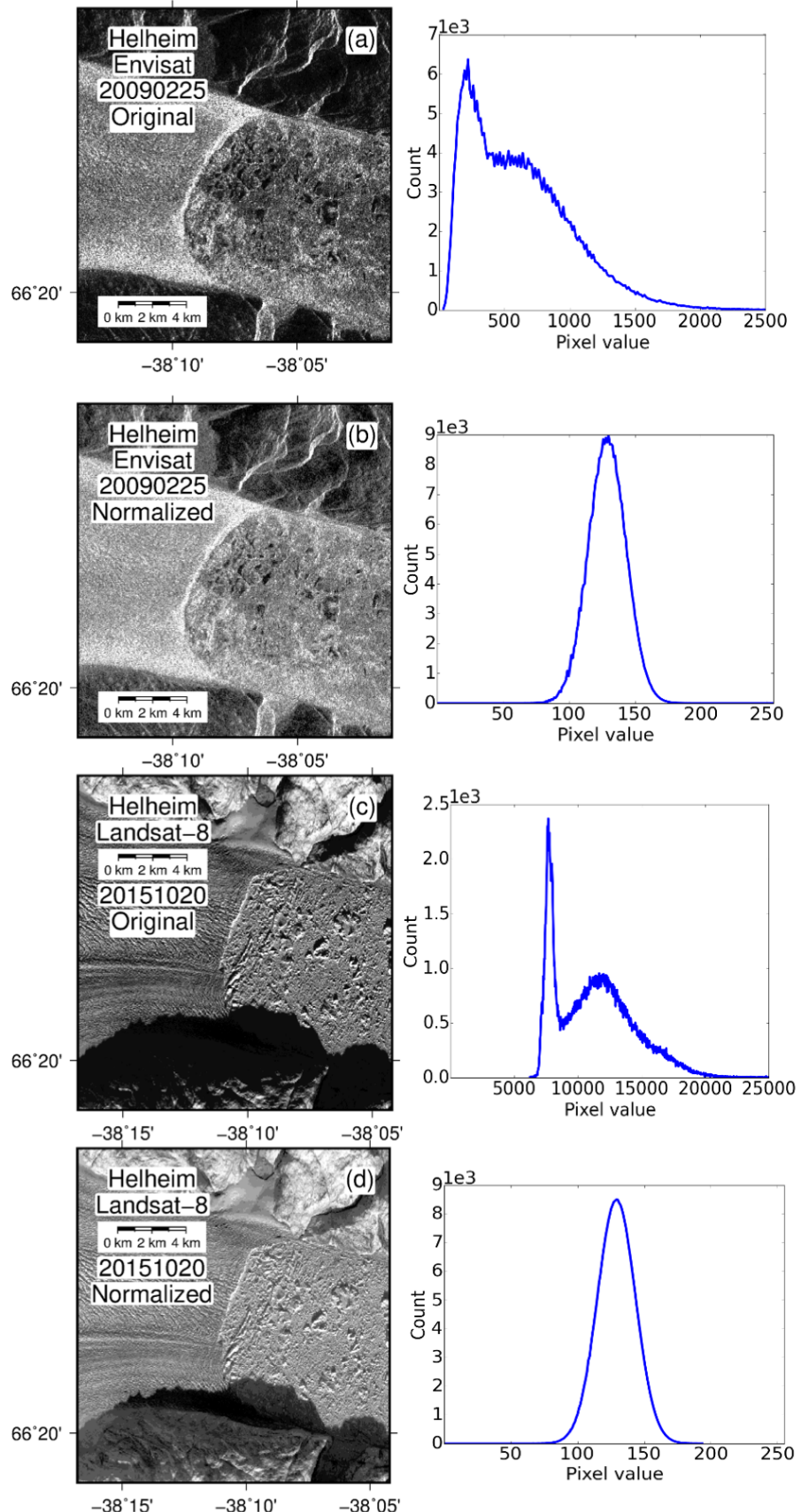


Figure 3.5: The comparison between original (a & c) and normalized images (b & d). We normalize each image histogram to the same Gaussian distribution with identical pixel value ranges (b & d). The second column shows the histograms of corresponding images.

contrast and yields better results, especially for optical images taken during polar winters and images with severe shadows (e.g., Figures 3.5c & d). To demonstrate the necessity and efficiency of histogram normalization, we also conduct two more experiments by 1) applying no histogram modification and 2) linearly stretching values between the 2<sup>nd</sup> and 98<sup>th</sup> percentiles of the histogram to the range between 0 and 255.

### 3.2.2.2 Network training

Figure 3.6 summarizes our data splitting strategy. The training-validation dataset includes 110 Landsat-8, 13 ALOS-1, 76 TSX, and 140 Sentinel-1 images over Jakobshavn and Kangerlussuaq. We randomly choose 90% of training-validation data for training and take the remaining 10% for validation. The training set optimizes the network’s parameters (such as weights and biases), while the validation set minimizes overfitting and optimizes the network’s hyperparameters (such as learning rate). The test dataset includes 74 Landsat-8, 52 Sentinel-2, 48 Envisat, 17 TSX, 90 Sentinel-1, 14 ALOS-2 images over Helheim. The test dataset can provide an independent estimation of the network’s accuracy. Testing through Sentinel-2, Envisat, and ALOS-2 images at Helheim, we demonstrate the network’s generalization on various targets with different glacial characteristics, and on optical, C- and L-band SAR images, respectively.

The training-validation dataset contains training images (remote sensing images) and their corresponding ground truth images. The ground truth images are binary segmented images that separate ice mélange and non-ice mélange regions. The ground truth images are derived by converting the vectors of manually delineated calving fronts to rasters. We also perform data augmentation as in Chapter 2, such as image rotation, flipping, and resampling, to diversify the training dataset and improve the generalization of our deep-learning-based method.

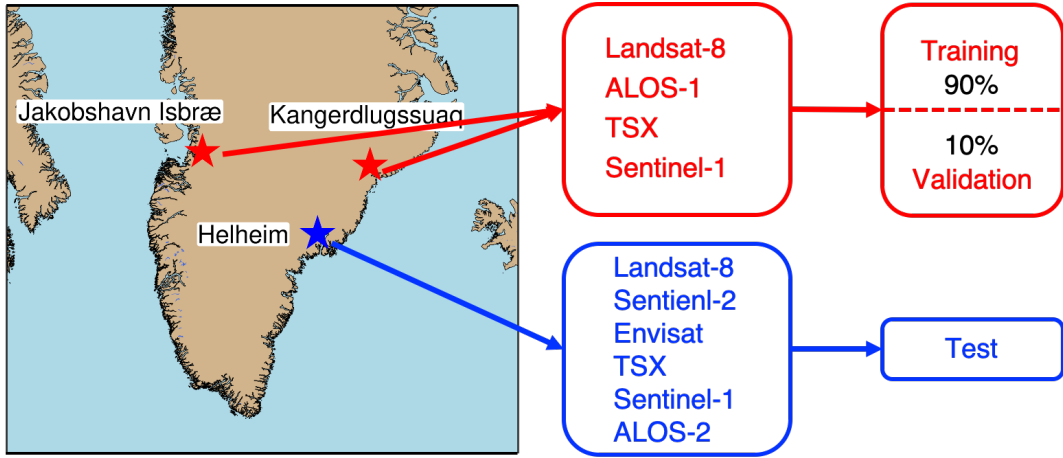


Figure 3.6: Illustration of our data splitting strategy. Red indicates the training-validation set while blue indicates the test set.

During the training, we calculate the validation error by calculating the intersection over union (IOU) after each training epoch. IOU is defined as

$$IOU(A, B) = \frac{area(A \cap B)}{area(A \cup B)} \quad (3.2)$$

where  $A$  is a network output, and  $B$  is its corresponding ground truth image. A higher IOU value represents a more accurate result. To minimize overfitting, we halt the training when the IOU value starts to decrease for five consecutive epochs. With the well-trained network, we generate binary label figures and extract calving fronts from them.

We conduct 12 experiments that combine three histogram modification strategies (histogram normalization, linear stretch, and no histogram modification) and four networks (ResNet-DeepLabv3+, DRN-DeepLabv3+, MobileNet-DeepLabv3+, and U-Net). To find the best combination, we measure the test error of each experiment by calculating the averaged width of the enclosed area bounded by the manually-delineated and network-delineated calving fronts.

### 3.2.2.3 Post-processing procedures

We adopt similar post-processing procedures with Chapter 2, including extracting boundaries, removing small polygons, and truncating boundaries to get the calving fronts. Besides, we develop an automated evaluation workflow based on the geometric complexity of calving fronts to discard unqualified results.

As pointed out in Chapter 2, smoothness is one of the criteria for preparing the training examples. Moreover, delineations with complex shapes are usually wrong in our results. The complexity calculation is derived from the combination of three metrics: frequency and amplitude of the vibration, and the convexity of the polygon [Brinkhoff et al., 1995]. Since the calving fronts are lines, we connect both ends of a front to form a polygon.

The frequency and amplitude of the vibration describe the local fluctuation. The global shape of a polygon also influences the rating of the complexity. Frequency is based on notches, namely the non-convex points of a polygon. The maximum number of a polygon's notches ( $N_{notch}$ ) cannot be larger than the number of vertices ( $N_{vertice}$ ) minus three. Accordingly, we normalize the number of notches ( $N_{notch}$ ) to the interval  $[0,1]$  by

$$\hat{N}_{notch} = \frac{N_{notch}}{N_{vertice} - 3} \quad (3.3)$$

In extreme cases of high frequency, every edge has a different direction from its predecessor, and  $\hat{N}_{notch}$  is 0.5. Both high and low  $\hat{N}_{notch}$  values indicate smooth boundaries. The following definition of vibration frequency ( $f$ ) fulfills these requirements:

$$f = (4 \times (\hat{N}_{notch} - 0.5^2) - 1)^2 \quad (3.4)$$

Vibration amplitude ( $A_m$ ) is defined as:

$$A_m = \frac{B_p - B_c}{B_p} \quad (3.5)$$

where  $B_p$  represents the boundary of the polygon and  $B_c$  is the boundary of its convex hull. A more complex shape always indicates a longer boundary, which has a higher amplitude value. Global convexity of a polygon ( $C_v$ ) is measured with the following equation:

$$C_v = \frac{a_c - a_p}{a_c} \quad (3.6)$$

where  $a_p$  is the area of the polygon and  $a_c$  is the area of its convex hull. Brinkhoff et al. (1995) further defined the complexity of a polygon based on experimental investigations and the consideration of combining local and global characteristics of a polygon:

$$C_p = 0.8 \times A \times f + 0.2 \times C_v \quad (3.7)$$

The complexity is in the interval [0,1] with low (high) value indicating simple (complex).

Taking Figure 3.1c as an example, the polygon formed by the front has 452 vertices and 204 notches. Therefore,  $\hat{N}_{notch}$  is equal to 0.452 and the vibration frequency is 0.98. The boundaries are 17582 meters for the polygon and 17401 meters for its convex hull, giving a vibration amplitude equal to 0.01. The areas are  $1.99 \times 10^7 \text{ m}^2$  for the polygon and  $2.02 \times 10^7 \text{ m}^2$  for its convex hull, and therefore its convexity is 0.014. Using all these parameters, the complexity of the polygon is calculated as 0.0065.

For polygons with large complexity, we will take them as unreasonable and abandon them. The complexity threshold varies for different glaciers due to their diverse terminal shapes. A large threshold could retain all good results but may miss some unqualified ones. To retain all the good results, we set the thresh-

old based on the maximum complexity of our manually-delineated calving fronts. The thresholds are 0.045 for Helheim, 0.1 for Jakobshavn Isbræ, and 0.043 for Kangerlussuaq. After removing unreasonable results based on complexity threshold, we conduct manual evaluation and discard the remaining unqualified results. With the network-delineated results, we quantify the calving front variations of each glacier. At each time step, we first calculate the enclosed area bounded by two temporally adjacent calving fronts. Then, we sum up all the enclosed areas in the current and previous time steps to obtain the total area change. The increasing area change means retreating, and decreasing means advancing.

### 3.3 Results

The key results are presented in the following order: (1) test-error-based comparison among the 12 experiments applied in multiple datasets as in Table 3.3; (2) calving front results from our best network as in Figure 3.7; and (3) calving front variation for each glacier as in Figures 3.9–3.11. Overall, all the DeepLabv3+ networks outperform U-Net regarding the test errors. For optical images, ResNet-DeepLabv3+ is superior, and linear stretching (for Landsat-8) or no histogram modification (for Sentinel-2) yields better results (Table 3.3). For most of the SAR images, the combination of histogram normalization and DRN-DeepLabv3+ is the finest. Envisat is an exception, for which linear stretching provides slightly

Table 3.3: The test errors (in meters) of different networks. Dark green indicates small test error. In the second column, “HN” means histogram normalization, “LS” means linear stretching, and “Non” means no histogram modification. The last three rows show the averages of test error weighted by each dataset’s number of images.

Dataset	Pre-Processing	DeepLabv3+			U-Net
		ResNet	DRN	MobileNet	
Landsat-8	HN	93	82	175	191
	LS	78	101	143	169
	Non	86	99	173	210
Sentinel-2	HN	73	82	187	267
	LS	80	82	121	301
	Non	63	93	119	202
Envisat	HN	111	101	184	255
	LS	168	95	179	297
	Non	194	246	158	204
TerraSAR-X	HN	54	53	113	70
	LS	97	72	126	85
	Non	90	94	141	142
Sentinel-1	HN	108	91	134	144
	LS	132	157	151	772
	Non	129	146	175	134
ALOS-2	HN	129	75	177	313
	LS	108	102	226	310
	Non	240	120	187	331
Average	HN	96	86	163	199
	LS	112	112	150	399
	Non	120	137	160	186

better results. Compared with optical imagery, SAR images are more diverse due to their different sensors, image bands, and image processing procedures. Moreover, the accuracy of DRN-DeepLabv3+ is comparable with the best network for optical images. Therefore, DRN-DeepLabv3+ has a greater ability to handle diverse datasets. For the two best networks, DRN-DeepLabv3+ and ResNet-DeepLabv3+, histogram normalization performs better in homogenizing the diversity of the dataset and further reducing test error. The combination of histogram normalization and DRN-DeepLabv3+ has the lowest test error considering

the experiments and datasets, of 86 meters (Table 3.3) or  $8.5 \times 10^5 \text{ m}^2$ .

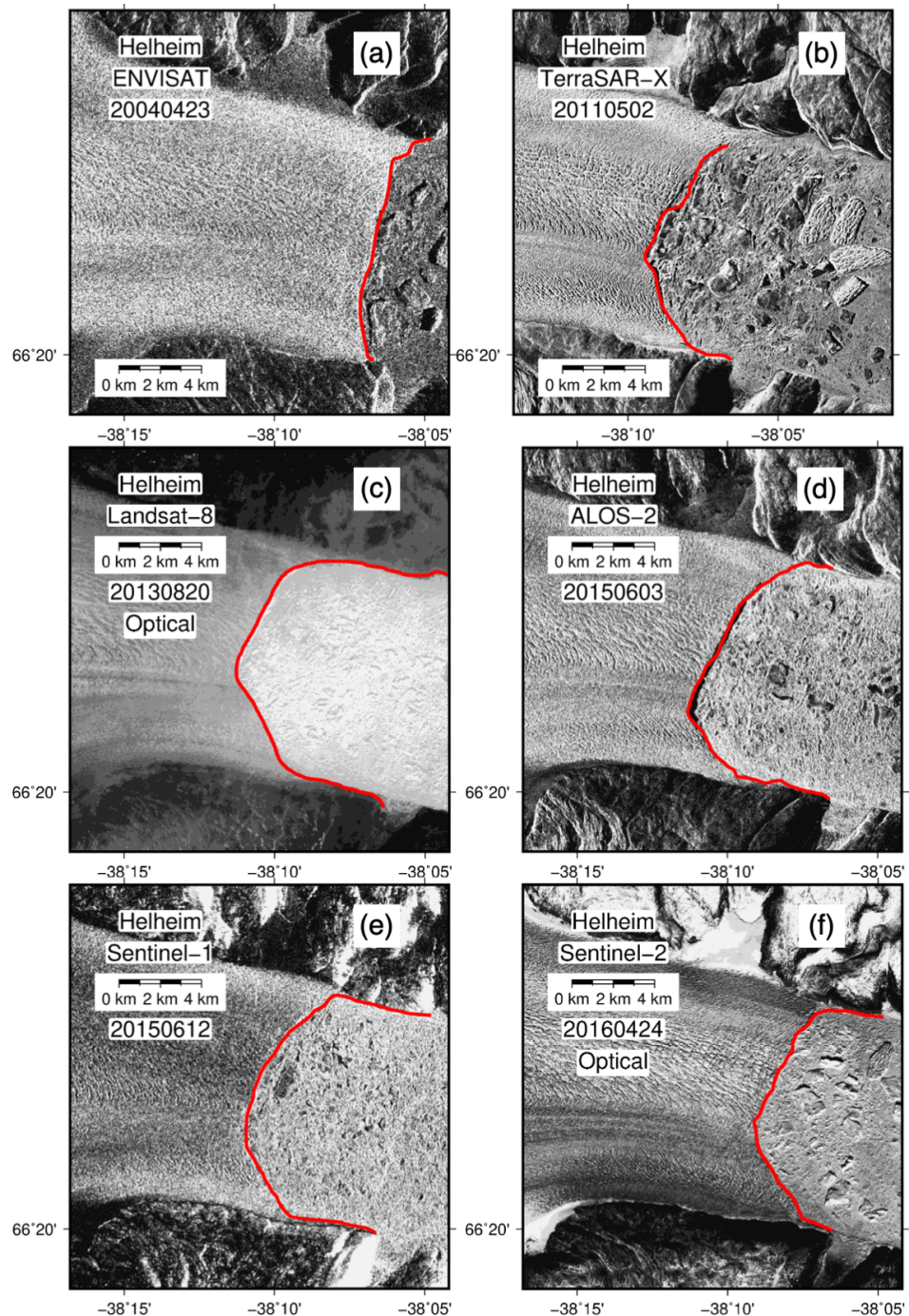


Figure 3.7: Examples of network-delineated calving fronts (red line) using all six datasets in the test sets.

Figure 3.7 shows examples of network-delineated calving fronts using all six datasets in the test set. Most of our results are promising, even for images with light cloud coverage (e.g., Figure 3.7c) and shadow (e.g., Figure 3.8). However, some images are covered by dense clouds or have blurred boundaries caused by the presence of snow cover or ice mélange bonding to the glacier. Since even experts find it difficult to manually delineate the calving fronts shown in low-quality images, we discard them in order to minimize the bias of test error.

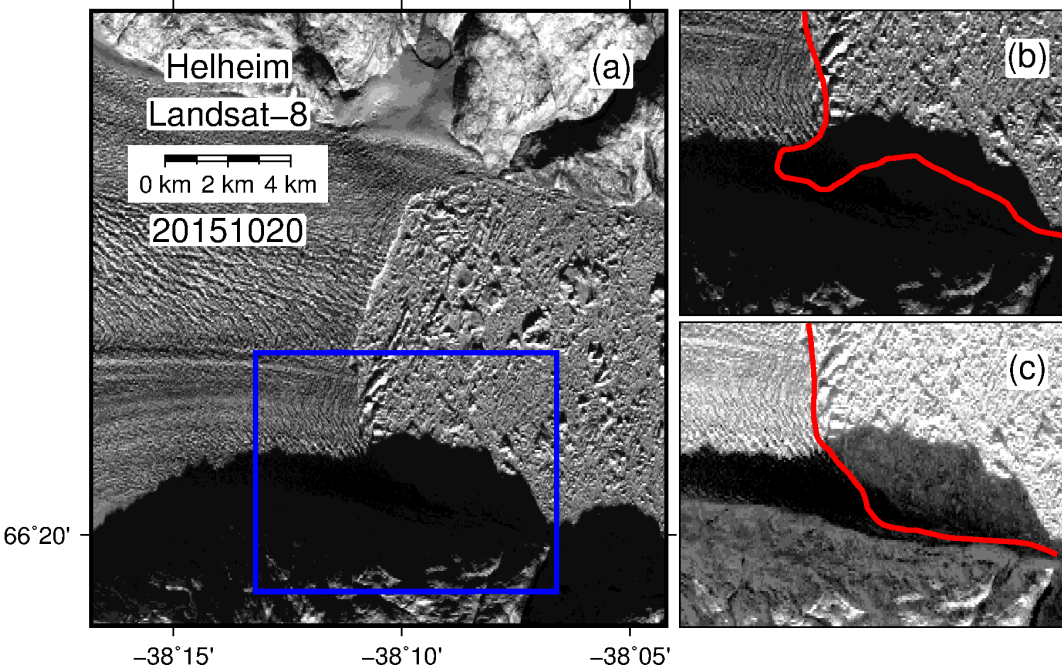


Figure 3.8: An example showing the contrast enhancement and the improvement after applying histogram normalization. (a) is the original image with severe shadow problem. (b) is the zoom-in figure of the shadowed area (blue box). (c) shows the same area as (b) but after applying histogram normalization. Red lines in (b) and (c) show the corresponding network-delineated calving fronts.

The integration of the seven datasets offers us sub-weekly calving front datasets of all three glaciers (Figures 3.9, 3.10, &3.11). In the time series of Jakobshavn Isbræ and Kangerlussuaq, ALOS-1 data are not included due to the limited samplings and data gap (e.g., no sampling from 2011 to 2013 at Kangerlussuaq). High

temporal resolution enables detailed investigations of calving front variations. For instance, we could directly obtain the number and the date of large calving events from the time series (shown as jumps in time series, e.g., Figures 3.10b, 3.11b, & 3.12). Unlike Jakobshavn Isbræ, Kangerlussuaq and Helheim have floating tongues, where large calving events occurred. Moreover, we could reliably capture the seasonal and interannual variations with high temporal resolution. In the following part, we will quantitatively analyze the interannual variations and describe the seasonality. Jakobshavn Isbræ's two branches underwent three-phase

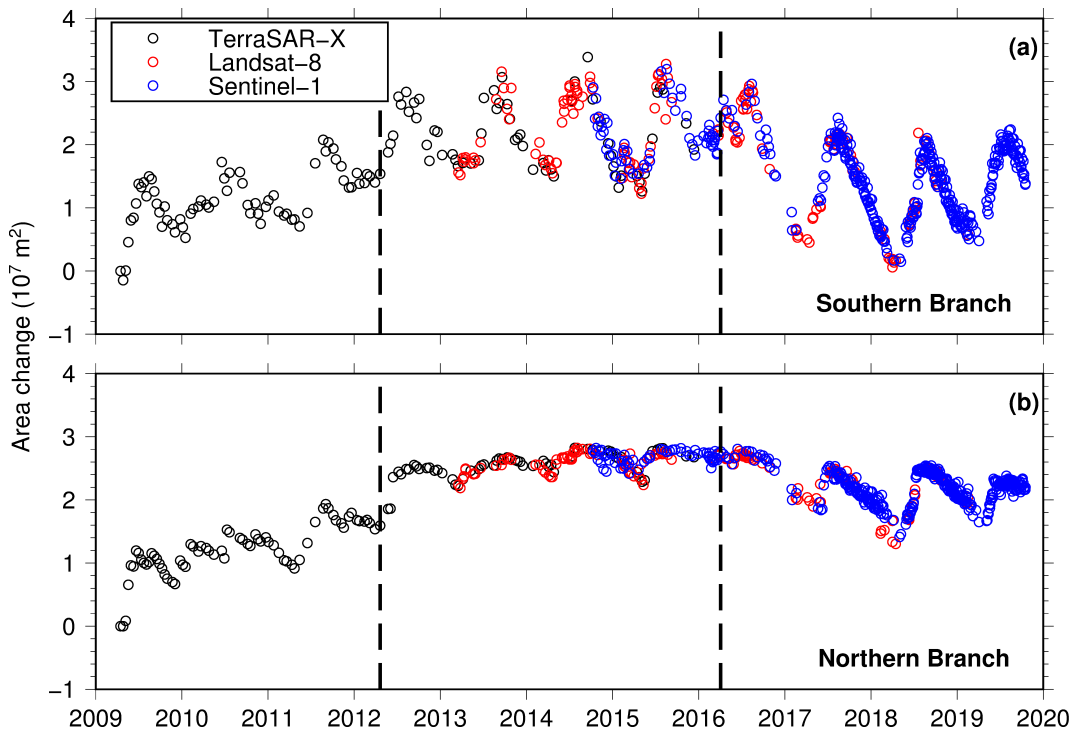


Figure 3.9: Time series of calving front variations of the two branches of Jakobshavn Isbræ. Dashed vertical lines divide the time series into three phases (see text).

interannual variations with strong seasonality. We separate the whole time series by the two beginnings of retreat seasons, namely April 2013 and April 2016. In the first phase (2009–2013), the two branches revealed linear retreat trends (–

$2.7 \times 10^6 \text{ m}^2 \text{ yr}^{-1}$  for the southern branch and  $-3.3 \times 10^6 \text{ m}^2 \text{ yr}^{-1}$  for the northern branch). In the second phase, from April 2013 to April 2016, their average changing rates remained low ( $-8.2 \times 10^4 \text{ m}^2 \text{ yr}^{-1}$  for the southern branch and  $-1.0 \times 10^6 \text{ m}^2 \text{ yr}^{-1}$  for the northern branch), and the seasonality of the northern branch almost vanished. In the third phase, both branches advanced dramatically in 2016, and on average, the rates of advance were  $2.0 \times 10^6 \text{ m}^2 \text{ yr}^{-1}$  for the southern branch and  $1.1 \times 10^6 \text{ m}^2 \text{ yr}^{-1}$  for the northern branch after April 2016. The time series

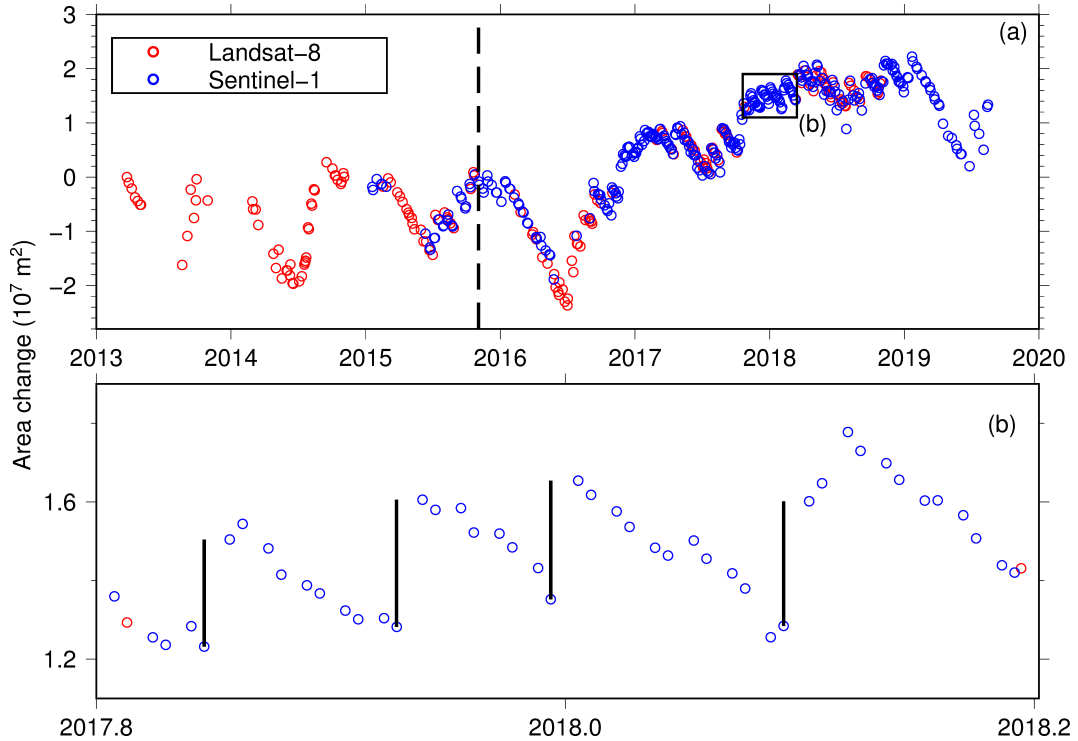


Figure 3.10: The time series of calving front variations of Kangerlussuaq. (b) is the zoomed-in figure within the black box in (a), showing the jumps (indicated by black bars) caused by large calving events. Dashed vertical lines divide the time series into two phases (see text).

of Kangerlussuaq's calving front variation shows strong interannual and seasonal variations, and its seasonality also changes interannually. We split the whole time series by November 2015, the beginning of advancing season in that year. We

choose to split the time series by the beginning of an advancing season, since Kangerlussuaq advanced at the beginning of the time series. The retreat rate was low during the first period ( $-8.4 \times 10^5 \text{ m}^2 \text{ yr}^{-1}$ ), while in the second period it was ten times larger than the previous period ( $-9.2 \times 10^6 \text{ m}^2 \text{ yr}^{-1}$ ). From 2013 to 2015, the retreating season was from July to November, while in 2016 it extended into March 2017. The seasonality remained intense from 2013 to 2016, weakened from 2017 to 2018, and recovered in 2019. We split the time series of Helheim

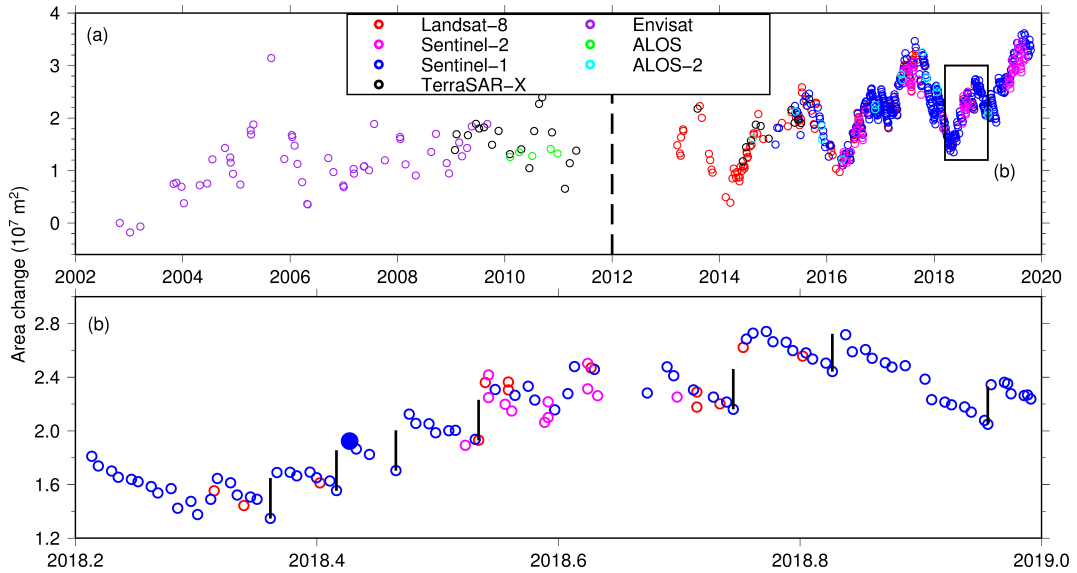


Figure 3.11: Time series of calving front variations of Helheim. (b) is the zoomed-in figure within the black box in (a), showing the jumps (indicated by black bars) caused by large calving events. The solid blue dot in (b) indicates the position after a large calving event (Figure 3.12). Dashed vertical lines divide the time series into two phases (see text).

by the data gap (from May 2011 to early 2013), and the glacier showed linear trends in both periods. The data gap was because the only operating satellite, TSX, did not cover Helheim. From 2002 to 2011, the retreat rate was  $-1.1 \times 10^6 \text{ m}^2 \text{ yr}^{-1}$ . During the second period (2013–2020) it doubled to  $-2.5 \times 10^6 \text{ m}^2 \text{ yr}^{-1}$ . The seasonality was not apparent in the first phase, which might be caused by the low sampling rate. After 2013, owing to high temporal resolution, We find

that weak and intense advances occurred alternately every two years.

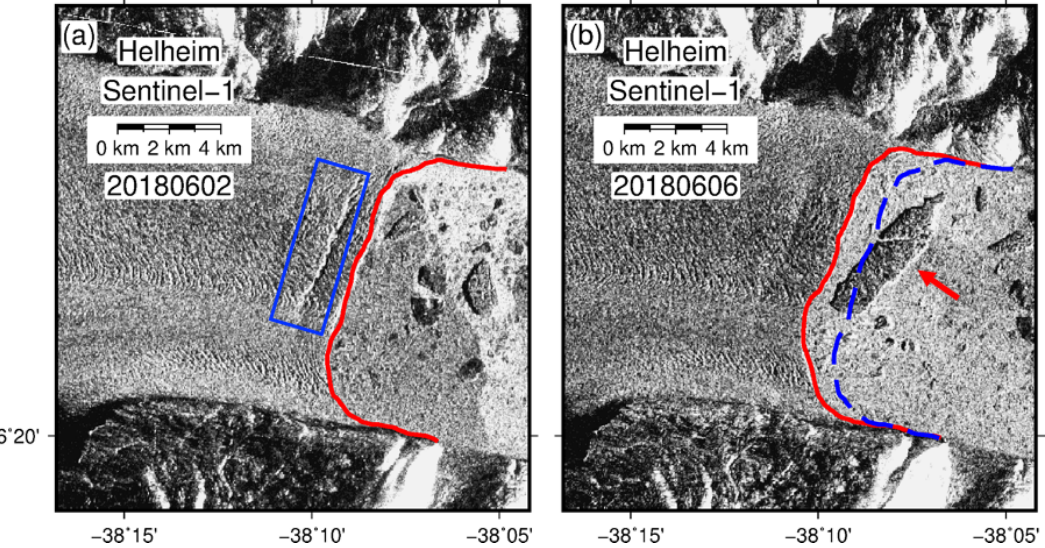


Figure 3.12: Images before (a) and after (b) a large calving event. Curves are network-delineated calving fronts. Blue dashed line in (b) is the same calving front in (a). Red arrow points at the tabular iceberg generated after the large calving event. Before the large calving event, a 4-km-long crevasse existed in the frontal area (blue box).

## 3.4 Discussion

### 3.4.1 Advantages and limitations

Compared with previous deep-learning-based studies, the major improvements we achieve in this work are 1) integrating seven datasets into a single deep learning network; and 2) applying this network to remote sensing datasets that are not included in the training. The two improvements are owing to the application of DeepLabv3+ and histogram normalization. DeepLabv3+ applies atrous convolution with different rates, which enables the network to sense multi-scale contextual information. Due to the spatial resolution differences, features with the same actual size have various pixel sizes in different images. For instance,

a 1-km-long crevasse occupies 20 pixels in Sentinel-1 images but 100 pixels in ALOS-2 images. Therefore, the ability to sense multi-scale contextual information is helpful when integrating datasets with different spatial resolutions.

A more diverse dataset requires a network with a larger learning capacity. The diversity of our dataset derives from both the different image properties and the complexity of the glacier systems. Because they were taken by various sensors, the original images are different in value range and image texture. By normalizing the histogram of images to the same Gaussian distribution with an identical value range, we can homogenize images and reduce the required learning capacity, allowing the network to tackle glaciers with more diverse glaciological settings such as fjord geometry, ice mélange strength, and floating conditions. Furthermore, after histogram normalization, the information extracted from one dataset can be applied to another, thus making it easier for the network to detect glacier fronts. Despite these advantages, our application of DeepLabv3+ is limited by the large computational power (88 Gigabytes GPU memory) and long training time (1-2 days). Another limitation of this method is that the automated evaluation workflow is insufficiently generalized. Although the workflow can release labor for evaluating the quality of results, we need to specify a threshold of complexity for each glacier. Applying the method to broader areas might require a universal criterion for evaluating the quality of the results.

### **3.4.2 Synchronous and asynchronous dynamic behaviors of glaciers**

The two branches of Jakobshavn Isbræ showed synchronous and asynchronous dynamic behavior in seasonal and interannual time scales. First, the seasonal signals of two branches match well. They both started to retreat around April and advance around September. The magnitude of the seasonal cycle of both

branches increased abruptly in 2017 and gradually diminished in 2019. Second, both branches underwent three-phase interannual variations. They both showed linear retreat trends from 2009 to 2013, remained at low changing rates from 2013 to 2016, and then started to advance. Third, despite the substantial synchronous variations in the two branches, they also behaved differently. For example, the magnitude of seasonality was larger in the southern branch than in the northern branch. Moreover, while the southern branch had a substantial seasonal variation, the northern branch's seasonality almost vanished from 2012 to 2016.

Helheim and Kangerlussuaq showed regional-coherent behaviors and local anomalies from 2013 to 2020. First, while both glaciers had substantial seasonal variations, their retreating periods were different. For Helheim, the retreating season was from March to September, while the Kangerlussuaq glacier retreated from July to November. Second, at both glaciers, the frequency of large calving events increased from 2017 to 2018 and declined in 2019. However, the number of large calving events was larger at Kangerlussuaq than at Helheim. Third, Kangerlussuaq showed distinct interannual variation, revealed by the dramatic retreat in 2016 and subsequent weak advance. Helheim's calving front varied regularly, showing a two-year cycle and linear retreat trend.

### 3.4.3 Misidentification caused by artifacts and tabular ice-bergs

Some of the SAR images have stripe artifacts (Figure 3.13). The network misidentifies some of these artifacts as glacier region due to both its glacier-like texture and the leak of training examples with artifacts. This type of artifact is due to the terrain correction of SAR images [Hau, 1999]. Terrain correction is the process for correcting geometric distortions that lead to geolocation errors, which is necessary since accurate geolocation is the prerequisite for combining multiple

datasets. In our example, the terrain correction stretches the foreshortening area and generates these stripe artifacts.

The floating ice tongue could generate quite large tabular icebergs, which have the same texture as glaciers. Therefore, when tabular icebergs had only just been detached from the glacier and were still close to the front, the network could have trouble separating them. Adding training examples with tabular icebergs close to the terminus could help solve this problem (Figure 3.14a). However, the number of training examples might not be sufficient to make the network generate promising results for all the cases (Figure 3.14b). In the current study, we discard these unreasonable results through the complexity evaluation. For instance, the example shown in Figure 3.14b with high complexity (0.21) has been discarded.

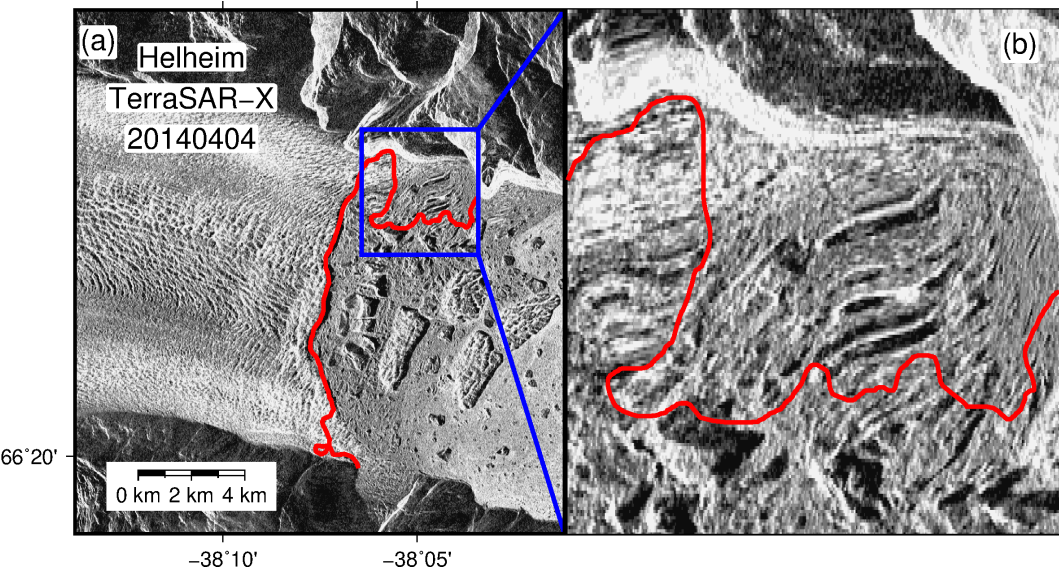


Figure 3.13: Example showing the stripe artifacts caused by terrain correction in SAR images. (b) shows the zoomed-in figure of artifacts within the blue box in (a). The red line is the calving front delineated by the network, showing the misidentifications of the artifacts as glacier ice.

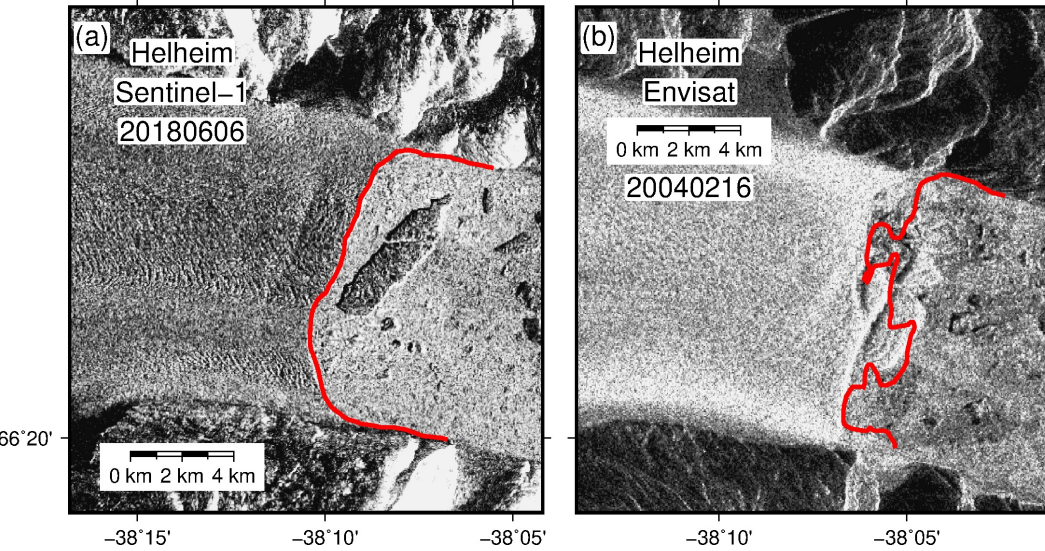


Figure 3.14: Two examples showing the results with newly generated tabular icebergs. The well-trained network could (a) generate promising results, or (b) misidentify the newly generated tabular icebergs as parts of the glacier. Red lines show the calving fronts delineated by the well-trained network.

### 3.4.4 Prospects for improvement

We could improve our method in two ways: (1) adding more training examples; and (2) modifying the current network or adopting a more advanced one. The first approach is the most direct way of improving the network’s accuracy. The second approach could improve the network’s learning capacity and accuracy and utilize training examples more efficiently.

The misidentifications for both artifacts and tabular icebergs are caused by the leak of their corresponding training examples. Moreover, when applying our method to other glaciers or datasets, different textures of a new target might also cause misidentification due to the complexity of the glacier system and the diverse datasets. Including more training examples could help to solve these misidentifications.

As with adding more training examples, data augmentation can also diversify

the training dataset and improve the generalization of the deep-learning-based method. However, the diversity enhanced by new training examples is greater than through augmented ones. Therefore, to balance the training data volume and required computational power, we could reduce the number of augmented training examples after adding new ones.

Three possible approaches could be adopted to modify our current network. First, the learning capacity of a network is restricted by the number of adjustable parameters. When the network reaches its maximum capacity, adding more training examples would not help improve the network's accuracy. In this case, we could enlarge the network's size (e.g., by adding more layers into the network). Second, our work only uses single-band images, which might not provide complete information. We could modify our current algorithm to fully utilize multi-band images or integrate other information such as elevation (e.g., DEM). Third, the design of DeepLabv3+'s decoder might not be sophisticated enough to recover object boundaries that are sharp enough to separate glacier and tabular iceberg. A more advanced decoder module might help to solve the misidentification of tabular icebergs.

Newly developed networks may also increase the accuracy of the results. For instance, [Zhang et al., 2018] have created a Context Encoding Network (EncNet) to capture global information of an image to improve segmentation accuracy. [Liu et al., 2018] have developed the Path Aggregation Network (PANet) to enhance information passing, aiming to propagate low-level features to the final output more accurately. These openly available networks provide us greater opportunities to extract glacier fronts from complex glacier systems and diverse datasets.

### 3.5 Conclusion

This study integrates seven remote sensing datasets into a single deep learning network. We automate the delineation of the calving fronts of the Jakobshavn Isbræ, Kangerlussuaq and Helheim glaciers using Envisat, TSX, Landsat-8, Sentinel-1 & -2, and ALOS-1 & -2 images. By conducting 12 experiments, we find that the combination of histogram normalization and DRN-DeepLabv3+ is most appropriate for our task. The successful application to an independent study area and datasets shows the high generalization of our method to various glacier targets and data types. The promising results for images with light cloud and shadow also demonstrate the robustness of our method. The integration of seven remote sensing datasets offers us sub-weekly calving front datasets. The high temporal resolution enables detailed investigation of seasonal and interannual calving front variations and large calving events. The increased accuracy, generalization, and robustness of the deep-learning method demonstrate that our method has the potential to be applied to many other tidewater glaciers both in Greenland and elsewhere in the world, using multi-temporal and multi-sensor remote sensing imagery.

---

□ End of chapter.

# Chapter 4

## Conclusion

### 4.1 Summary

This dissertation presents two deep-learning-based works of automated delineating glacier fronts in Greenland from remote sensing imagery. First, we apply U-Net, a deep learning architecture to TSX images at Jakobshavn Isbræ (Chapter 2). We develop an innovative deep learning-based framework that includes image pre-processing, the preparation of training examples, data augmentation, and post-processing. Demonstrating through this successful case study on Jakobshavn Isbræ, we prove the feasibility of applying deep learning to automate the glacier front delineation, establishing the foundation of this dissertation. The second work, building on the experience and results from the first one, further increases the generalization, accuracy, and robustness of the deep-learning-based method (Chapter 3). We successfully integrate seven remote sensing datasets into a single deep learning network and delineate fronts of the three largest glaciers in Greenland. The main technical improvements we made from the first to second work are in two aspects: first, we apply a more advanced deep-learning architecture, namely DeepLabv3+, for solving the diversity introduced by the

multi-sensor datasets and complex glacier system; second, we adopt histogram normalization to homogenize the diversity of multi-sensor remote sensing imagery. The conclusions of this dissertation are as follows:

1. Deep-learning-based method can be successfully applied to automate the glacier front delineation using multi-temporal and multi-sensor remote sensing imagery.
2. DeepLabv3+ outperforms U-Net regarding result' accuracy, and its accuracy is close to human-level.
3. Histogram normalization can effectively homogenize the diversity of multi-sensor remote sensing imagery and improve the accuracy.
4. The generalization of the deep-learning-based method are proved by applying to glaciers and datasets that are not included in the training, indicating its potential of being applied to many other glaciers both in Greenland and elsewhere in the world.
5. Retreating into an overdeepened basin might trigger the unstable dynamic behavior of Jakobshavn Isbræ.
6. High temporal resolution of the calving front dataset enables us to directly obtain the number and the date of large calving events from the time series.

## 4.2 Future Work

The future work will focus on two aspects: (1) applying the deep learning-based method to all the large outlet glaciers in Greenland, (2) quantifying the spatio-temporal characteristics of calving front variations, and (3) using Structural equa-

tion modeling (SEM) to investigate the local controlling factors of multi-decadal changes at selected glaciers.

### 4.2.1 A broader application to all major outlet glaciers in Greenland

A calving front dataset that is both spatially and temporally comprehensive is required to better understand glacier front changes. Through the two works of automated delineating glacier fronts, we have proved the feasibility of the deep learning-based method and further demonstrated its generalization on various glacier targets and datasets. In the future, we will apply the well-trained network to remote sensing images taken by 11 space-borne sensors (listed in Figure 1.3) across Greenland and obtain ice front at sub-monthly intervals. Such a broader application introduces more complexities, which might require more training examples or a more advanced network. Next, we will describe the strategy for the broader application. We first group images according to their location and data type, considering the similarities in glaciological settings and image properties. For a group of images, we apply them to the well-trained network and use the evaluation workflow (described in section 3.2.2.3) to estimate the quality of the results. If more than 10% of the results are unqualified, we will randomly select half of them as training examples and retrain the network. Otherwise, we will consider the current network applicable to this group of images and move on to the next. If the network fail to produce promising results for images in the training set, we will consider to modify our network or adopt a more advanced one (discussed in section 3.4.3).

#### 4.2.2 Quantifying the spatio-temporal characteristics of calving front variations

With the network-delineated glacier fronts, we will produce the time series of calving front variations at each glacier. To further quantify the spatio-temporal characteristics of calving front variations, we will calculate the annual, sub-annual, decadal, and multi-decadal retreat rates of each glacier. Since front changes differently in winter and summer [Kehrl et al., 2017; Fried et al., 2018], we will separately calculate sub-annual retreat rates during winter (November to April) and summer (May to October). We will also calculate the decadal rates during two periods: from 2000 to 2010 and 2011 to 2021, as well as multi-decadal rates from 2000 to 2022. Moreover, we will generate maps of annual rates, winter rates, and summer rates in each year, decadal rates, and multi-decadal rates. Regional-coherent position changes have been documented by previous studies [Murray et al., 2015]. Deriving from a comprehensive dataset, these maps will likely illustrate both the regional-coherent behaviors (especially at decadal and multi-decadal time scales) and local anomalies.

#### 4.2.3 Using structural equation modeling to analyze causal relationships

Controls on calving front variations are numerous and complex [Fried et al., 2018]. Correlation analysis, despite its simplicity, cannot reveal if which factors are the main drivers of frontal changes [Hill et al., 2017; Cowton et al., 2018]. Therefore, a quantitative analysis of causal relationships between front variations and various forcing is required.

We will analyze the time series of annual retreat rates using Structural equation modeling (SEM) to investigate the local controlling factors of front variations at

selected glaciers. SEM is a statistic framework for quantitatively investigating multivariate causal relationships [Grace, 2006; Bendixen et al., 2017]. The meta-model of our SEM will build on prior expected primary relationships between meltwater runoff, ocean temperature, air temperature, sea ice coverage, bed elevation at the front, and glacier front variations as well as confounding factors such as height above sea level and spatial gradient of glacier surface velocity (see Figure 4.1 for an example and note that the numerical values are all assumed for illustrative purpose).

For instance, the ocean temperature can affect the front variations directly and indirectly through sea ice coverage and submarine melting. Moreover, ocean temperature can be influenced by air temperature and have an undirected relationship with sea ice coverage and submarine melting. Both sea ice coverage and meltwater runoff can affect the front variations and be influenced by air temperature (Figure 4.1). By using SEM, we can quantitatively assess the strength of the links between each pair of related variables.

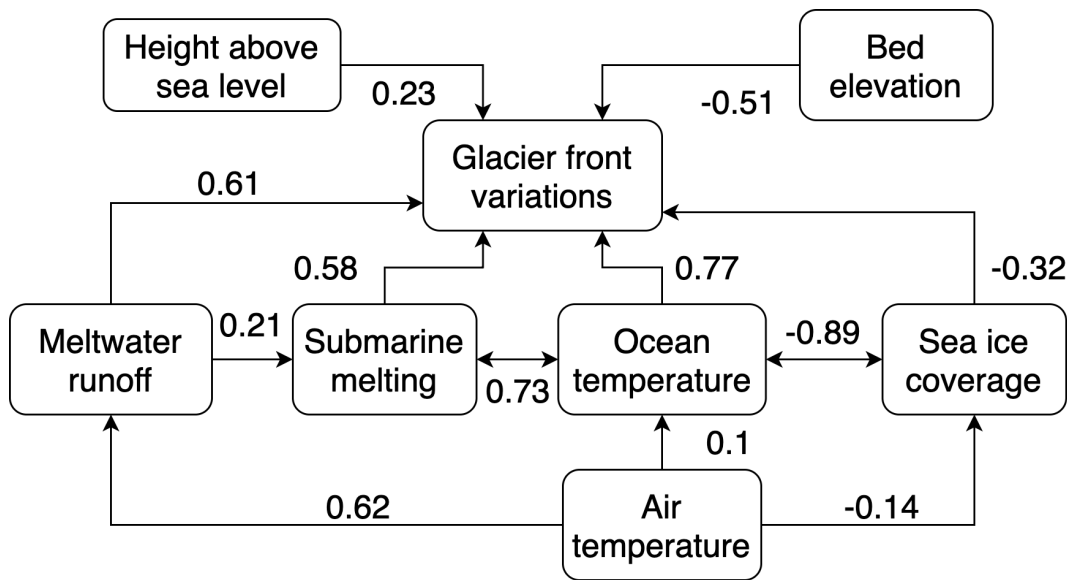


Figure 4.1: Meta-model showing hypothesized causal links from which a structural equation model was constructed. One-headed arrows indicate a directed relationship, and two-headed arrows indicate an undirected relationship. The numbers on the arrows are fictitious path coefficients. The absolute value of each number means the intensity of the corresponding causal links, and the sign means positive (+) or negative (-) relationship between two variables.

---

End of chapter.

## Appendix A

### Supplementary figures, movies and tables for Chapter 2

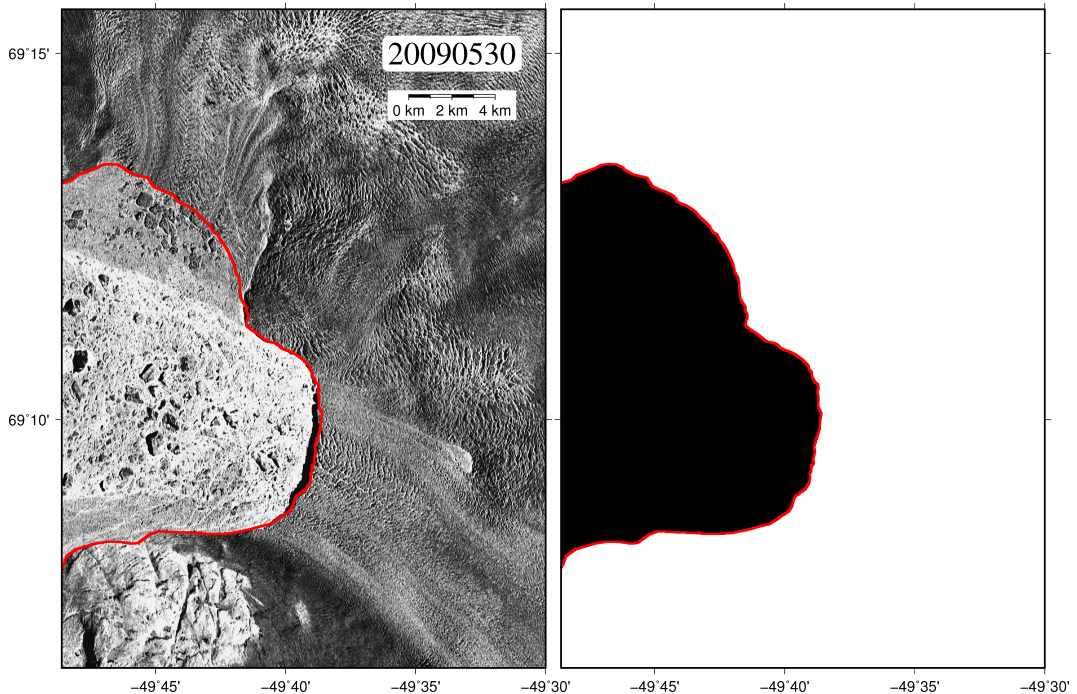


Figure A.1: An example of the training dataset. The left is a training image, and the right one is its ground truth image where the black region is ice mélange and the white region is non-ice mélange (including both glacier and bedrock). The red line is the calving front we delineate manually.

APPENDIX A. SUPPLEMENTARY FIGURES, MOVIES AND TABLES FOR CHAPTER 278

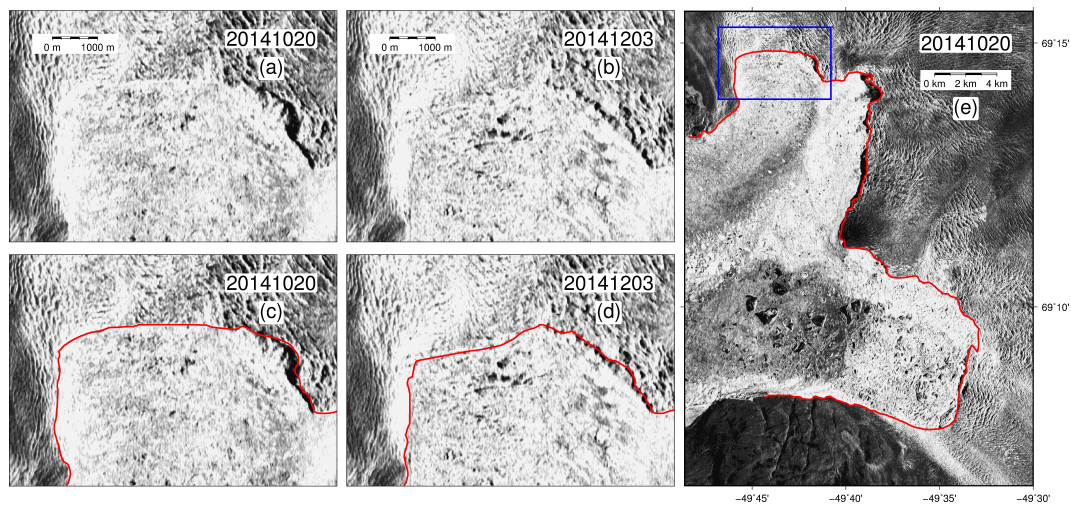


Figure A.2: An example showing how we use a reference image to delineate a smooth calving front on a winter image with obscure boundaries. (a) is the reference image and (b) is the image with obscure boundaries. (c) and (d) show the manually delineated calving fronts. The blue box in (e) shows the location of (a)-(d).

APPENDIX A. SUPPLEMENTARY FIGURES, MOVIES AND TABLES FOR CHAPTER 27

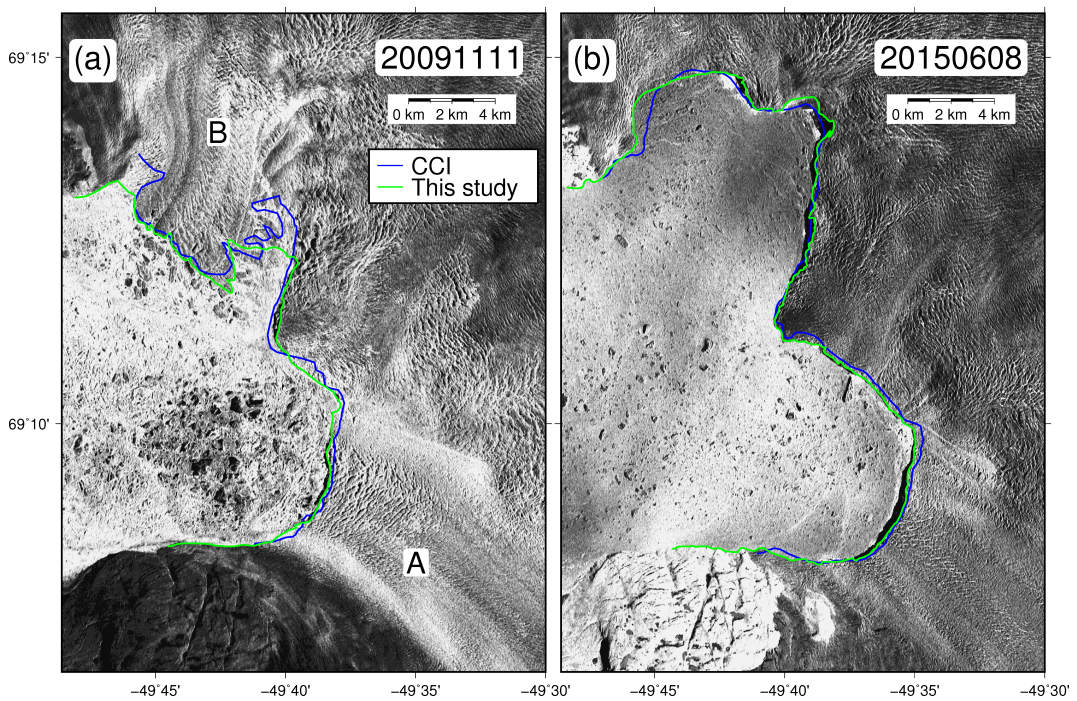


Figure A.3: Two examples showing the validation of re-georeferencing. In both (a) and (b), the two lines show the manually delineated calving fronts from ours and the CCI.

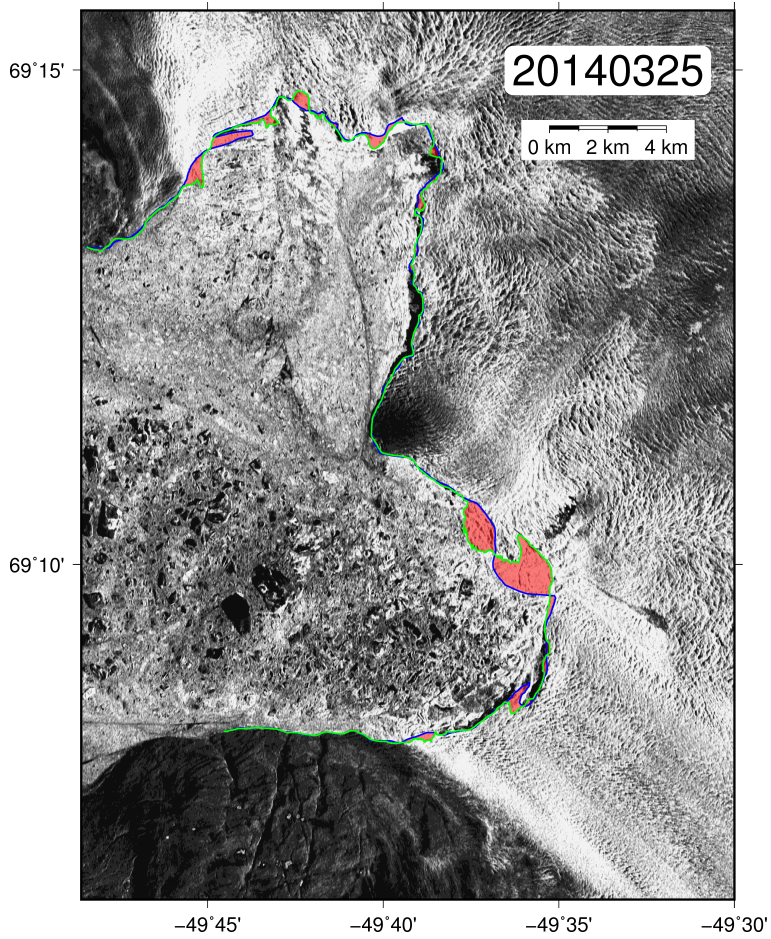


Figure A.4: An example of error estimation of the network-delineation. The green line is the calving front we manually delineate. The yellow line is the calving front delineated by the deep-learning network. The red zone indicates the error of our results, which is the area circled by the green and yellow lines.

**Movie A.1:** A movie showing the calving front positions from April 16th, 2009 to December 23rd, 2015. The red curve indicates the calving fronts delineated by our deep learning network.

DOI: <https://doi.pangaea.de/10.1594/PANGAEA.897062>.

**Movie A.2:** A movie showing the calving front variation of Branch A and the cross-section between the calving front and the profile. Two green lines indicate the bed elevation profiles. The red line shows the calving front position.

DOI: <https://doi.pangaea.de/10.1594/PANGAEA.897080>.

**Movie A.3:** Similar to Movie S2 but for Branch B.

DOI: <https://doi.pangaea.de/10.1594/PANGAEA.897063>.

Table A.1: Test error of each image and their means.

Date	Error (m)	Date	Error	Date	Error
20090702	26	20111221	48	20140427	72
20090906	20	20120225	27	20140702	38
20090928	50	20120307	23	20140714	29
20091009	66	20120614	20	20140725	14
20091020	52	20120707	20	20140918	32
20091111	34	20120820	15	20141009	27
20091203	25	20120911	24	20141203	24
20100105	38	20120921	38	20141225	31
20100207	58	20121014	52	20150105	35
20100323	65	20121115	34	20150116	31
20100425	56	20121219	63	20150207	35
20100506	57	20130120	59	20150323	42
20100630	58	20130222	57	20150425	30
20100915	12	20130306	58	20150506	48
20101018	31	20130407	37	20150608	12
20101120	42	20130418	32	20150619	22
20101223	28	20130510	23	20150711	23
20110125	21	20130624	39	20150802	20
20110216	43	20130727	55	20150813	67
20110310	22	20130828	32	20150904	45
20110423	102	20130908	24	20151018	28
20110526	61	20130920	34	20151029	48
20110617	31	20131012	30	20151120	38
20110903	19	20131125	19	20151223	32
20111005	26	20131217	51		
20111016	24	20140303	49	Total Mean	38 (6 pixels)
20111108	67	20140325	74	Summer Mean	31 (5 pixels)
20111210	35	20140405	38	Winter mean	42 (7 pixels)

## Appendix B

### Glossary of abbreviations

**AdaMax**: Adaptive moment estimation max

**ASAR**: Advanced Synthetic Aperture Radar

**ASPP**: Atrous Spatial Pyramid Pooling

**ASTER**: Advanced Spaceborne Thermal Emission and Reflection Radiometer

**BCE**: Binary cross-entropy

**CCI**: The Greenland Ice Sheet Climate Change Initiative

**CNN**: Convolutional neural network

**DCNN**: Deep convolution neural network

**DLR**: Deutsches Zentrum für Luft- und Raumfahrt

**EEC**: Enhanced ellipsoid corrected

**EW**: Extra Wide Swath

**GAN**: Generative Adversarial Network

**GDAL**: Geospatial Data Abstraction Library

**GIMP**: The Greenland Ice Mapping Project

**GPU**: Graphics processing unit

**GRD**: Ground Range Detected

**InSAR**: Interferometric SAR

**IOU**: Intersection over union

**IW:** Interferometric Wide Swath

**LeakyReLU:** Leaky rectified linear unit

**MSI:** Multi-spectral instruments

**PALSAR:** Phased Array type L-band Synthetic Aperture Radar

**PROMICE:** Programme for Monitoring of the Greenland Ice Sheet

**SAR:** Synthetic Aperture Radar

**SEM:** Structural equation modeling

**SLC:** Scan Line Corrector

**SM:** Strip Map

**SMB:** Surface mass balance

**SWIR:** Short wave infrared spectral range

**TSX:** TerraSAR-X

**VNIR:** Visible/near infrared

**WV:** Wave

# List of publications and outputs

## *Publications*

**Zhang, E.**, Liu, L., Huang, L. and Ng, K. S. Automatically delineating calving fronts of Greenland glaciers from multi-sensor remote sensing imagery: a general method based on deep learning. *Manuscript under review*.

**Zhang, E.**, Liu, L., and Huang, L. (2019). Automatically delineating the calving front of Jakobshavn Isbræ from multitemporal TerraSAR-X images: a deep learning approach. *The Cryosphere*, 13(6), 1729-1741.

Zhang, B., L. Liu, S. A. Khan, T. van Dam, A. A. Bjørk, Y. Peings, **Zhang, E.**, M. Bevis, Y. Yao, and B. Noël (2019), Geodetic and model data reveal different spatio-temporal patterns of transient mass changes over Greenland from 2007 to 2017, *Earth and Planetary Science Letters*, 515, 154–163, doi:10.1016/j.epsl.2019.03.028.

Zhang, B., **Zhang, E.**, L. Liu, S. A. Khan, T. van Dam, Y. Yao, M. Bevis, V. Helm (2018), Geodetic measurements reveal short-term changes of glacial mass near Jakobshavn Isbræ (Greenland) from 2007 to 2017, *Earth and Planetary Science Letters*, 503, 216–226, doi:10.1016/j.epsl.2018.09.029.

Zhang, B., Liu, L., Khan, S. A., Dam, T., **Zhang, E.**, Yao, Y. (2017). Transient variations in glacial mass near Upernivik Isstrøm (west Greenland) detected by the combined use of GPS and GRACE data *Journal of Geophysical Research: Solid Earth*, 122(12).

***Conference******AGU Fall Meeting, 2019, Oral Presentation***

Automatically delineating calving fronts of Greenland glaciers from multi-sensor remote sensing imagery: a general method based on deep learning

***AGU Fall Meeting, 2018, Poster Presentation***

Automatically delineating terminus of Jakobshavn Isbræ from multi-sensor remote sensing imagery based on deep learning

***Workshop on Glacial Isostatic Adjustment and Elastic Deformation, 2017, Poster Presentation***

Transient variations in ice mass near Jakobshavn Isbræ (west Greenland) detected by the combined use of GPS and GRACE data

***Data***

**Zhang, Enze** (2019): The calving fronts delineated by the network in Jakobshavn Isbræ. PANGAEA, <https://doi.org/10.1594/PANGAEA.897064>.

***Code***

**Zhang, Enze** (2020), [https://github.com/enzezhang/Front\\_DL3](https://github.com/enzezhang/Front_DL3).

# Bibliography

- Amundson, J. M., Fahnestock, M., Truffer, M., Brown, J., Lüthi, M. P., and Motyka, R. J. (2010). Ice mélange dynamics and implications for terminus stability, Jakobshavn Isbræ, Greenland. *Journal of Geophysical Research: Earth Surface*, 115(F01005):F01005.
- Anantrasirichai, N., Biggs, J., Albino, F., Hill, P., and Bull, D. (2018). Application of Machine Learning to Classification of Volcanic Deformation in Routinely Generated InSAR Data. *Journal of Geophysical Research: Solid Earth*, 123(8):6592–6606.
- Andersen, J. K., Fausto, R. S., Hansen, K., Box, J. E., Andersen, S. B., Ahlstrøm, A. P., van As, D., Citterio, M., Colgan, W., Karlsson, N. B., et al. (2019). Update of annual calving front lines for 47 marine terminating outlet glaciers in greenland (1999–2018). *Geological Survey of Denmark and Greenland Bulletin*.
- Bamber, J. L., Westaway, R. M., Marzeion, B., and Wouters, B. (2018). The land ice contribution to sea level during the satellite era. *Environmental Research Letters*, 13(6):063008.
- Bartholomaus, T. C., Larsen, C. F., and O’Neil, S. (2013). Does calving matter? Evidence for significant submarine melt. *Earth and Planetary Science Letters*, 380:21 – 30.

- Batista, G. E. A. P. A., Prati, R. C., and Monard, M. C. (2005). Balancing strategies and class overlapping. In Famili, A. F., Kok, J. N., Peña, J. M., Siebes, A., and Feelders, A., editors, *Advances in Intelligent Data Analysis VI*, pages 24–35, Berlin, Heidelberg. Springer Berlin Heidelberg.
- Baumhoer, C. A., Dietz, A. J., Kneisel, C., and Kuenzer, C. (2019). Automated Extraction of Antarctic Glacier and Ice Shelf Fronts from Sentinel-1 Imagery Using Deep Learning. *Remote Sensing*, 11(21).
- Bendixen, M., Iversen, L. L., Bjørk, A. A., Elberling, B., Westergaard-Nielsen, A., Overeem, I., Barnhart, K. R., Khan, S. A., Box, J. E., Abermann, J., et al. (2017). Delta progradation in Greenland driven by increasing glacial mass loss. *Nature*, 550(7674):101.
- Benn, D. I., Cowton, T., Todd, J., and Luckman, A. (2017). Glacier calving in Greenland. *Current Climate Change Reports*, 3(4):282–290.
- Bentes, C., Frost, A., Velotto, D., and Tings, B. (2016). In *Proceedings of EUSAR 2016: 11th European Conference on Synthetic Aperture Radar, title=Ship-Iceberg Discrimination with Convolutional Neural Networks in High Resolution SAR Images*, pages 1–4.
- Bjørk, A. A., Kjær, K. H., Korsgaard, N. J., Khan, S. A., Kjeldsen, K. K., Andresen, C. S., Box, J. E., Larsen, N. K., and Funder, S. (2012). An aerial view of 80 years of climate-related glacier fluctuations in southeast Greenland. *Nature Geoscience*, 5(6):427–432.
- Bondzio, J. H. (2017). *Analysis of Recent Dynamic Changes of Jakobshavn Isbrae, West Greenland, Using a Thermomechanical Model*. PhD thesis.
- Brinkhoff, T., Kriegel, H.-P., Schneider, R., and Braun, A. (1995). Measuring the complexity of polygonal objects. In *ACM-GIS*, page 109. Citeseer.

- Bunce, C., Carr, J. R., Nienow, P. W., Ross, N., and Killick, R. (2018). Ice front change of marine-terminating outlet glaciers in northwest and southeast Greenland during the 21st century. *Journal of Glaciology*, 64(246):523–535.
- Carr, J. R., Stokes, C. R., and Vieli, A. (2017). Threefold increase in marine-terminating outlet glacier retreat rates across the atlantic arctic: 1992–2010. *Annals of Glaciology*, 58(74):72–91.
- Carroll, D., Sutherland, D. A., Shroyer, E. L., Nash, J. D., Catania, G. A., and Stearns, L. A. (2015). Modeling turbulent subglacial meltwater plumes: Implications for Fjord-scale buoyancy-driven circulation. *Journal of Physical Oceanography*, 45(8):2169–2185.
- Cassotto, R., Fahnestock, M., Amundson, J. M., Truffer, M., and Joughin, I. (2015). Seasonal and interannual variations in ice mélange and its impact on terminus stability, Jakobshavn Isbræ, Greenland. *Journal of Glaciology*, 61(225):76–88.
- Catania, G. A., Stearns, L. A., Sutherland, D. A., Fried, M. J., Bartholomaus, T. C., Morlighem, M., Shroyer, E., and Nash, J. (2018). Geometric controls on tidewater glacier retreat in central western Greenland. *Journal of Geophysical Research: Earth Surface*, 123(8):2024–2038.
- Chen, L.-C., Zhu, Y., Papandreou, G., Schroff, F., and Adam, H. (2018). Encoder-Decoder with Atrous Separable Convolution for Semantic Image Segmentation. *Lecture Notes in Computer Science*, page 833–851.
- Cooke, C. L. V. and Scott, K. A. (2019). Estimating Sea Ice Concentration From SAR: Training Convolutional Neural Networks With Passive Microwave Data. *IEEE Transactions on Geoscience and Remote Sensing*, 57(7):4735–4747.

- Cowton, T. R., Sole, A. J., Nienow, P. W., Slater, D. A., and Christofersen, P. (2018). Linear response of east Greenland's tidewater glaciers to ocean/atmosphere warming. *Proceedings of the National Academy of Sciences*, 115(31):7907–7912.
- Fahnstock, M., Bindschadler, R., Kwok, R., and Jezek, K. (1993). Greenland Ice Sheet Surface Properties and Ice Dynamics from ERS-1 SAR Imagery. 262(5139):1530–1534.
- Fried, M. J., Catania, G. A., Bartholomaus, T. C., Duncan, D., Davis, M., Stearns, L. A., Nash, J., Shroyer, E., and Sutherland, D. (2015). Distributed subglacial discharge drives significant submarine melt at a greenland tidewater glacier. *Geophysical Research Letters*, 42(21):9328–9336.
- Fried, M. J., Catania, G. A., Stearns, L. A., Sutherland, D. A., Bartholomaus, T. C., Shroyer, E., and Nash, J. (2018). Reconciling Drivers of Seasonal Terminus Advance and Retreat at 13 Central West Greenland Tidewater Glaciers. *Journal of Geophysical Research: Earth Surface*, 123(7):1590–1607.
- Gao, L., Tian, T., Sun, X., and Li, H. (2018). Fusion of shallow and deep features for classification of high-resolution remote sensing images. In *MIPPR 2017: Multispectral Image Acquisition, Processing, and Analysis*, volume 10607.
- Geng, J., Fan, J., Wang, H., Ma, X., Li, B., and Chen, F. (2015). High-Resolution SAR Image Classification via Deep Convolutional Autoencoders. *IEEE Geoscience and Remote Sensing Letters*, 12(11):2351–2355.
- Goodfellow, I., Bengio, Y., and Courville, A. (2016). *Deep Learning*. MIT Press.
- Gorelick, N., Hancher, M., Dixon, M., Ilyushchenko, S., Thau, D., and Moore, R. (2017). Google earth engine: Planetary-scale geospatial analysis for everyone. *Remote Sensing of Environment*, 202:18 – 27.

- Grace, J. B. (2006). *Structural equation modeling and natural systems*. Cambridge University Press.
- Hau, C. C. (1999). *Information processing for remote sensing*. World Scientific.
- He, K., Zhang, X., Ren, S., and Sun, J. (2016). Deep residual learning for image recognition. *2016 IEEE Conference on Computer Vision and Pattern Recognition (CVPR)*, pages 770–778.
- Hill, E. A., Carr, J. R., and Stokes, C. R. (2017). A review of recent changes in major marine-terminating outlet glaciers in Northern Greenland. *Frontiers in Earth Science*, 4:111.
- Holland, D. M., Thomas, R. H., De Young, B., Ribergaard, M. H., and Lyberth, B. (2008). Acceleration of Jakobshavn Isbræ triggered by warm subsurface ocean waters. *Nature geoscience*, 1(10):659–664.
- Howard, A. G., Zhu, M., Chen, B., Kalenichenko, D., Wang, W., Weyand, T., Andreetto, M., and Adam, H. (2017). Mobilenets: Efficient convolutional neural networks for mobile vision applications. *arXiv preprint arXiv:1704.04861*.
- Howat, I. M., Ahn, Y., Joughin, I., van den Broeke, M. R., Lenaerts, J. T. M., and Smith, B. (2011). Mass balance of Greenland’s three largest outlet glaciers, 2000–2010. *Geophysical Research Letters*, 38(12):L12501.
- Howat, I. M., Box, J. E., Ahn, Y., Herrington, A., and McFadden, E. M. (2010). Seasonal variability in the dynamics of marine-terminating outlet glaciers in greenland. *Journal of Glaciology*, 56(198):601–613.
- Howat, I. M. and Eddy, A. (2011). Multi-decadal retreat of Greenland’s marine-terminating glaciers. *Journal of Glaciology*, 57(203):389–396.

- Howat, I. M., Joughin, I., Fahnestock, M., Smith, B. E., and Scambos, T. A. (2008). Synchronous retreat and acceleration of southeast Greenland outlet glaciers 2000–06: ice dynamics and coupling to climate. *Journal of Glaciology*, 54(187):646–660.
- Howat, I. M., Joughin, I., and Scambos, T. A. (2007). Rapid Changes in Ice Discharge from Greenland Outlet Glaciers. *Science*, 315(5818):1559–1561.
- Howat, I. M., Joughin, I., Tulaczyk, S., and Gogineni, S. (2005). Rapid retreat and acceleration of Helheim Glacier, east Greenland. *Geophysical Research Letters*, 32(22):L22502.
- Huang, L., Luo, J., Lin, Z., Niu, F., and Liu, L. (2020). Using deep learning to map retrogressive thaw slumps in the Beiluhe region (Tibetan Plateau) from CubeSat images. *Remote Sensing of Environment*, 237:111534.
- Huang, Z., Pan, Z., and Lei, B. (2017). Transfer Learning with Deep Convolutional Neural Network for SAR Target Classification with Limited Labeled Data. *Remote Sensing*, 9(9):907.
- James, T. D., Murray, T., Selmes, N., Scharrer, K., and O’Leary, M. (2014). Buoyant flexure and basal crevassing in dynamic mass loss at Helheim Glacier. *Nature Geoscience*, 7(8):593–596.
- Jenkins, A. (2011). Convection-Driven Melting near the Grounding Lines of Ice Shelves and Tidewater Glaciers. *Journal of Physical Oceanography*, 41(12):2279–2294.
- Joughin, I., Abdalati, W., and Fahnestock, M. (2004). Large fluctuations in speed on Greenland’s Jakobshavn Isbrae glacier. *Nature*, 432(7017):608.

- Joughin, I., Das, S. B., King, M. A., Smith, B. E., Howat, I. M., and Moon, T. (2008a). Seasonal Speedup Along the Western Flank of the Greenland Ice Sheet. *Science*, 320(5877):781–783.
- Joughin, I., Howat, I., Alley, R. B., Ekstrom, G., Fahnestock, M., Moon, T., Nettles, M., Truffer, M., and Tsai, V. C. (2008b). Ice-front variation and tide-water behavior on Helheim and Kangerdlugssuaq Glaciers, Greenland. *Journal of Geophysical Research: Earth Surface*, 113(F1):F01004.
- Joughin, I., Howat, I. M., Fahnestock, M., Smith, B., Krabill, W., Alley, R. B., Stern, H., and Truffer, M. (2008c). Continued evolution of Jakobshavn Isbrae following its rapid speedup. *Journal of Geophysical Research: Earth Surface*, 113(F4):F04006.
- Joughin, I., Smith, B. E., Howat, I. M., Floricioiu, D., Alley, R. B., Truffer, M., and Fahnestock, M. (2012). Seasonal to decadal scale variations in the surface velocity of Jakobshavn Isbrae, Greenland: Observation and model-based analysis. *Journal of Geophysical Research: Earth Surface*, 117(F2):F02030.
- Joughin, I., Smith, B. E., Shean, D. E., and Floricioiu, D. (2014). Brief Communication: Further summer speedup of Jakobshavn Isbrae. *The Cryosphere*, 8(1):209–214.
- Kehrl, L. M., Joughin, I., Shean, D. E., Floricioiu, D., and Krieger, L. (2017). Seasonal and interannual variabilities in terminus position, glacier velocity, and surface elevation at Helheim and Kangerlussuaq Glaciers from 2008 to 2016. *Journal of Geophysical Research: Earth Surface*, 122(9):1635–1652.
- Khan, S. A., Aschwanden, A., Bjørk, A. A., Wahr, J., Kjeldsen, K. K., and Kjær, K. H. (2015). Greenland ice sheet mass balance: a review. *Reports on Progress in Physics*, 78(4):046801.

- Khazendar, A., Fenty, I. G., Carroll, D., Gardner, A., Lee, C. M., Fukumori, I., Wang, O., Zhang, H., Seroussi, H., Moller, D., Noël, B. P. Y., van den Broeke, M. R., Dinardo, S., and Willis, J. (2019). Interruption of two decades of Jakobshavn Isbrae acceleration and thinning as regional ocean cools. *Nature Geoscience*, 12(4):277.
- King, M. D., Howat, I. M., Jeong, S., Noh, M. J., Wouters, B., Noël, B., and van den Broeke, M. R. (2018). Seasonal to decadal variability in ice discharge from the Greenland Ice Sheet. *The Cryosphere*, 12(12):3813–3825.
- Kingma, D. P. and Ba, J. (2014). Adam: A method for stochastic optimization. *arXiv preprint arXiv:1412.6980*.
- Krieger, L. and Floricioiu, D. (2017). Automatic glacier calving front delineation on Terrasar-x and Sentinel-1 sar imagery. In *2017 IEEE International Geoscience and Remote Sensing Symposium (IGARSS)*, pages 2817–2820.
- Kussul, N., Lavreniuk, M., Skakun, S., and Shelestov, A. (2017). Deep Learning classification of land cover and crop types using remote sensing data. *IEEE Geoscience and Remote Sensing Letters*, 14(5):778–782.
- Lea, J. M., Mair, D. W. F., Nick, F. M., Rea, B. R., van As, D., Morlighem, M., Nienow, P. W., and Weidick, A. (2014). Fluctuations of a greenlandic tidewater glacier driven by changes in atmospheric forcing: observations and modelling of kangiata nunaata sermia, 1859–present. *The Cryosphere*, 8(6):2031–2045.
- LeCun, Y., Bengio, Y., and Hinton, G. (2015). Deep learning. *Nature*, 521:436.
- Leong, W. J. and Horgan, H. J. (2020). DeepBedMap: Using a deep neural network to better resolve the bed topography of Antarctica. *The Cryosphere Discussions*, 2020:1–27.

- Liu, H. and Jezek, K. C. (2004). A complete high-resolution coastline of Antarctica extracted from orthorectified Radarsat SAR imagery. *Photogrammetric Engineering & Remote Sensing*, 70(5):605–616.
- Liu, S., Qi, L., Qin, H., Shi, J., and Jia, J. (2018). Path Aggregation Network for instance segmentation. *2018 IEEE/CVF Conference on Computer Vision and Pattern Recognition*.
- Luckman, A., Benn, D. I., Cottier, F., Bevan, S., Nilsen, F., and Inall, M. (2015). Calving rates at tidewater glaciers vary strongly with ocean temperature. *Nature communications*, 6(1):1–7.
- Luckman, A. and Murray, T. (2005). Seasonal variation in velocity before retreat of Jakobshavn Isbræ, Greenland. *Geophysical Research Letters*, 32(8):L08501.
- Luckman, A., Murray, T., de Lange, R., and Hanna, E. (2006). Rapid and synchronous ice-dynamic changes in East Greenland. *Geophysical Research Letters*, 33(3):L03503.
- Maas, A. L., Hannun, A. Y., and Ng, A. Y. (2013). Rectifier nonlinearities improve neural network acoustic models. In *Proc. icml*, volume 30, page 3.
- McFadden, E. M., Howat, I. M., Joughin, I., Smith, B. E., and Ahn, Y. (2011). Changes in the dynamics of marine terminating outlet glaciers in west Greenland (2000–2009). *Journal of Geophysical Research: Earth Surface*, 116(F2):F02022.
- Meier, M. F. and Post, A. (1987). Fast tidewater glaciers. *Journal of Geophysical Research: Solid Earth*, 92(B9):9051–9058.
- Mohajerani, Y., Wood, M., Velicogna, I., and Rignot, E. (2019). Detection of

- glacier calving margins with convolutional neural networks: A case study. *Remote Sensing*, 11.
- Moon, T. and Joughin, I. (2008). Changes in ice front position on Greenland's outlet glaciers from 1992 to 2007. *Journal of Geophysical Research: Earth Surface*, 113(F2):F02022.
- Moon, T., Joughin, I., and Smith, B. (2015). Seasonal to multiyear variability of glacier surface velocity, terminus position, and sea ice/ice mélange in northwest Greenland. *Journal of Geophysical Research: Earth Surface*, 120(5):818–833.
- Moon, T., Joughin, I., Smith, B., van den Broeke, M. R., van de Berg, W. J., Noël, B., and Usher, M. (2014). Distinct patterns of seasonal Greenland glacier velocity. *Geophysical Research Letters*, 41(20):7209–7216.
- Morlighem, M., Williams, C. N., Rignot, E., An, L., Arndt, J. E., Bamber, J. L., Catania, G., Chauché, N., Dowdeswell, J. A., Dorschel, B., Fenty, I., Hogan, K., Howat, I., Hubbard, A., Jakobsson, M., Jordan, T. M., Kjeldsen, K. K., Millan, R., Mayer, L., Mouginot, J., Noël, B. P. Y., O'Cofaigh, C., Palmer, S., Rysgaard, S., Seroussi, H., Siegert, M. J., Slabon, P., Straneo, F., van den Broeke, M. R., Weinrebe, W., Wood, M., and Zinglersen, K. B. (2017). BedMachine v3: Complete bed topography and ocean bathymetry mapping of Greenland from multibeam echo sounding combined with mass conservation. *Geophysical Research Letters*, 44(21):11,051–11,061.
- Motyka, R. J., Truffer, M., Fahnestock, M., Mortensen, J., Rysgaard, S., and Howat, I. (2011). Submarine melting of the 1985 Jakobshavn Isbræ floating tongue and the triggering of the current retreat. *Journal of Geophysical Research: Earth Surface*, 116:F01007.

- Murray, T., Scharrer, K., Selmes, N., Booth, A. D., James, T. D., Bevan, S. L., Bradley, J., Cook, S., Llana, L. C., Drocourt, Y., Dyke, L., Goldsack, A., Hughes, A. L., Luckman, A. J., and McGovern, J. (2015). Extensive retreat of Greenland tidewater glaciers, 2000 – 2010. *Arctic, Antarctic, and Alpine Research*, 47(3):427–447.
- Nick, F. M., Vieli, A., Andersen, M. L., Joughin, I., Payne, A., Edwards, T. L., Pattyn, F., and van de Wal, R. S. (2013). Future sea-level rise from Greenland’s main outlet glaciers in a warming climate. *Nature*, 497(7448):235–238.
- Nick, F. M., Vieli, A., Howat, I. M., and Joughin, I. (2009). Large-scale changes in Greenland outlet glacier dynamics triggered at the terminus. *Nature Geoscience*, 2(2):110.
- Nogueira, K., Penatti, O. A., and dos Santos, J. A. (2017). Towards better exploiting convolutional neural networks for remote sensing scene classification. *Pattern Recognition*, 61:539–556.
- Rignot, E., Braaten, D., Gogineni, S. P., Krabill, W. B., and McConnell, J. R. (2004). Rapid ice discharge from southeast Greenland glaciers. *Geophysical Research Letters*, 31(10):L10401.
- Ronneberger, O., Fischer, P., and Brox, T. (2015). U-Net: Convolutional networks for biomedical image segmentation. In Navab, N., Hornegger, J., Wells, W. M., and Frangi, A. F., editors, *Medical Image Computing and Computer-Assisted Intervention – MICCAI 2015*, pages 234–241.
- Rosenau, R., Schwalbe, E., Maas, H.-G., Baessler, M., and Dietrich, R. (2013). Grounding line migration and high-resolution calving dynamics of Jakobshavn Isbræ, West Greenland. *Journal of Geophysical Research: Earth Surface*, 118(2):382–395.

- Roth, A., Huber, M., and Kosmann, D. (2004). Geocoding of TerraSAR-X data. *Proc. Int. 20th ISPRS Congr*, pages 840–844.
- Schild, K. M. and Hamilton, G. S. (2013). Seasonal variations of outlet glacier terminus position in Greenland. *Journal of Glaciology*, 59(216):759–770.
- Seale, A., Christoffersen, P., Mugford, R. I., and O’Leary, M. (2011). Ocean forcing of the Greenland Ice Sheet: Calving fronts and patterns of retreat identified by automatic satellite monitoring of eastern outlet glaciers. *Journal of Geophysical Research: Earth Surface*, 116(F3):F03013.
- Sohn, H.-G. and Jezek, K. C. (1996). Ice sheet margin detection using ERS-1 synthetic aperture radar. In *IGARSS ’96. 1996 International Geoscience and Remote Sensing Symposium*, volume 1, pages 148–150.
- Sohn, H.-G., Jezek, K. C., and van der Veen, C. J. (1998). Jakobshavn Glacier, west Greenland: 30 years of spaceborne observations. *Geophysical Research Letters*, 25(14).
- Stearns, L. A. and Hamilton, G. S. (2007). Rapid volume loss from two East Greenland outlet glaciers quantified using repeat stereo satellite imagery, journal = Geophysical Research Letters. 34(5):L05503.
- Straneo, F., Heimbach, P., Sergienko, O., Hamilton, G., Catania, G., Griffies, S., Hallberg, R., Jenkins, A., Joughin, I., Motyka, R., Pfeffer, W. T., Price, S. F., Rignot, E., Scambos, T., Truffer, M., and Vieli, A. (2013). Challenges to Understanding the Dynamic Response of Greenland’s Marine Terminating Glaciers to Oceanic and Atmospheric Forcing. *Bulletin of the American Meteorological Society*, 94(8):1131–1144.
- Sun, Y., Wang, X., and Tang, X. (2014). Deep learning face representation from

- predicting 10,000 classes. In *Proceedings of the IEEE conference on computer vision and pattern recognition*, pages 1891–1898.
- Thomas, R. H. (2004). Force-perturbation analysis of recent thinning and acceleration of Jakobshavn Isbræ, Greenland. *Journal of Glaciology*, 50(168):57–66.
- van den Broeke, M., Bamber, J., Ettema, J., Rignot, E., Schrama, E., van de Berg, W. J., van Meijgaard, E., Velicogna, I., and Wouters, B. (2009). Partitioning recent Greenland mass loss. *Science*, 326(5955):984–986.
- van den Broeke, M., Box, J., Fettweis, X., Hanna, E., Noël, B., Tedesco, M., van As, D., van de Berg, W. J., and van Kampenhout, L. (2017). Greenland Ice Sheet Surface Mass Loss: Recent Developments in Observation and Modeling. *Current Climate Change Reports*, 3(4):345–356.
- Van Der Veen, C. (1996). Tidewater calving. *Journal of Glaciology*, 42(141):375–385.
- Vieli, A. and Nick, F. M. (2011). Understanding and modelling rapid dynamic changes of tidewater outlet glaciers: issues and implications. *Surveys in Geophysics*, 32(4-5):437–458.
- Wagner, T. J. W., James, T. D., Murray, T., and Vella, D. (2016). On the role of buoyant flexure in glacier calving. *Geophysical Research Letters*, 43(1):232–240A.
- Walsh, K. M., Howat, I. M., Ahn, Y., and Enderlin, E. M. (2012). Changes in the marine-terminating glaciers of central east Greenland, 2000–2010. *The Cryosphere*, 6(1):211–220.

- Wang, L., Scott, K. A., Xu, L., and Clausi, D. A. (2016). Sea Ice Concentration Estimation During Melt From Dual-Pol SAR Scenes Using Deep Convolutional Neural Networks: A Case Study. *IEEE Transactions on Geoscience and Remote Sensing*, 54(8):4524–4533.
- Warren, C. R. (1991). Terminal environment, topographic control and fluctuations of West Greenland glaciers. *Boreas*, 20(1):1–15.
- Xie, S., Dixon, T. H., Voytenko, D., Holland, D. M., Holland, D., and Zheng, T. (2016). Precursor motion to iceberg calving at Jakobshavn Isbræ, Greenland, observed with terrestrial radar interferometry. *Journal of Glaciology*, 62(236):1134–1142.
- Yu, F., Koltun, V., and Funkhouser, T. (2017). Dilated residual networks. In *Proceedings of the IEEE conference on computer vision and pattern recognition*, pages 472–480.
- Zhang, E., Liu, L., and Huang, L. (2019). Automatically delineating the calving front of Jakobshavn Isbræ from multitemporal TerraSAR-X images: a deep learning approach. *The Cryosphere*, 13(6):1729–1741.
- Zhang, F., Du, B., and Zhang, L. (2015). Saliency-Guided unsupervised feature learning for scene classification. *IEEE Transactions on Geoscience and Remote Sensing*, 53(4):2175–2184.
- Zhang, H., Dana, K., Shi, J., Zhang, Z., Wang, X., Tyagi, A., and Agrawal, A. (2018). Context encoding for semantic segmentation. *2018 IEEE/CVF Conference on Computer Vision and Pattern Recognition*.
- Zhu, X. X., Tuia, D., Mou, L., Xia, G., Zhang, L., Xu, F., and Fraundorfer, F. (2017). Deep Learning in Remote Sensing: A comprehensive review and list of resources. *IEEE Geoscience and Remote Sensing Magazine*, 5(4):8–36.